Nano Research Energy

ISSN 2791-0091 (print); 2790-8119 (online)
https://doi.org/10.26599/NRE.2025.9120207

Review Article

Ion storage mechanisms in TiO_2

Zhiyu Zou[1,2,§], Yongbiao Mu[1,2,§], Meisheng Han[1,2] (✉), Hengyuan Hu[1,2], Kunxiong Zheng[1,2], Quanyan Man[1,2], Zijian Qiu[1,2], Wenjia Li[1,2], Lei Wei[1,2], Lin Zeng[1,2] (✉), and Tianshou Zhao[1,2] (✉)

[1] *Shenzhen Key Laboratory of Advanced Energy Storage, Department of Mechanical and Energy Engineering, Southern University of Science and Technology, Shenzhen 518055, China*
[2] *SUSTech Energy Institute for Carbon Neutrality, Southern University of Science and Technology, Shenzhen 518055, China*
[§] *Zhiyu Zou and Yongbiao Mu contributed equally to this work.*

Received: 2 September 2025 / **Revised:** 21 October 2025 / **Accepted:** 27 October 2025 / **Published date:** 2 April 2026

ABSTRACT

Titanium dioxide (TiO_2) is a non-toxic, stable, naturally abundant, and easily synthesized material that has been extensively investigated in various energy fields, including rechargeable ion batteries, solar cells and photocatalysis. Recently, TiO_2 has garnered significant attention as a promising negative electrode material for sodium-ion batteries. However, the ion storage mechanism of TiO_2 remains poorly understood, with existing studies often presenting inconsistent or contradictory results. This review critically summarizes recent researches on advances in understanding the ion storage mechanisms of TiO_2 electrode materials in both lithium-ion and sodium-ion batteries, with a particular focus on the latest findings related to *in-situ* electrochemically induced crystalline-to-amorphous-to-rock-salt phase transformations. This emerging concept challenges the traditional perspective that irreversible phase evolution is inherently detrimental. Instead, the *in-situ* formation of new rock-salt phases with enhanced electrochemical storage capabilities for Li^+ or Na^+ offers a promising alternative strategy for the design of next-generation TiO_2–based negative electrodes. Furthermore, we highlight a rich yet underexplored research area with significant potential to deepen the understanding of electrochemical phase transitions in TiO_2 and other metal oxide electrodes within energy storage systems.

KEYWORDS

ion storage mechanisms, phase transition, rock-salt phase, negative electrode, TiO_2

1 Introduction

In recent years, the global energy landscape has been rapidly shifting from the dominance of fossil energy to a new direction of low-carbon and multi-energy synergistic paradigm. Energy storage has emerged as a critical enabler for the widespread deployment of intermittent power generation technologies and has consequently received significant attention [1, 2]. Although lithium-ion batteries (LIBs) have dominated the market for portable electronic devices since their commercialization in 1991 [3], their limited global lithium reserves and associated safety concerns have hindered their ability to meet the growing demands of energy storage market. Fortunately, sodium-ion batteries (SIBs), owing to the low cost and natural abundance of sodium, as well as their physicochemical similarities to lithium, have been extensively investigated and are regarded as one of the most promising alternatives to commercial LIBs, especially for large-scale energy storage applications [4–6]. However, the higher standard reduction potential of sodium ($E^0_{(Na^+/Na)}$ = −2.71 V vs. $E^0_{(Li^+/Li)}$ = −3.01 V), its larger ionic radius (1.02 Å for Na^+ vs. 0.76 Å for Li^+), and the thermodynamic instability of Na-intercalated graphite compounds, making conventional graphite anodes (negative electrode) used in LIBs unsuitable for SIBs, pose substantial challenges, leading to poor electrochemical activity [7]. Although hard carbon has attracted considerable attention as a negative electrode material for SIBs, it still faces significant challenges related to safety, poor rate capability, and limited cycling stability [8]. Despite the identification of numerous positive electrode materials for SIBs [9–15], the development of suitable negative electrode materials remains limited. Therefore, the exploration and design of high-performance negative electrode materials are imperative for advancing SIB technology.

Since its discovery in 1821, titanium dioxide (TiO_2) has been extensively studied across a wide range of fields, including photocatalysis [16–18], rechargeable ion batteries [19–23], solar cells [24–26], sensors [27, 28], medicines, food packing and cosmetic industry [29–31], due to its non-toxicity, stability, natural abundance, and ease of synthesis. The unique properties of TiO_2 have driven nearly a century of continuous research and exploration. Early studies primarily focused on elucidating its

Address correspondence to Meisheng Han, hanms@sustech.edu.cn; Lin Zeng, zengl3@sustech.edu.cn; Tianshou Zhao, zhaots@sustech.edu.cn

crystallographic structure. For example, in 1916, Vegard first investigated the anatase and rutile phases of TiO_2 using Bragg's ionization method [32], and these structures were later refined by Greenwood [33]. Although foundational, these early investigations lacked the precision required for detailed structural characterization. In 1955, Cromer et al. precisely determined the crystallographic parameters of anatase and rutile using X-ray diffraction (XRD), laying the groundwork for subsequent research on TiO_2-based electrodes [34]. Since then, numerous studies have been dedicated to the classification and structural refinement of TiO_2. With advancements in experimental techniques, the known structural forms of TiO_2 have been revisited and characterized with significantly higher accuracy, leading to the identification of multiple polymorphs, including naturally occurring, metastable, and high-pressure phases. Their corresponding crystal structures are presented in Fig. 1 and include anatase TiO_2(A) (crystal system: tetragonal, space group:$I4_1/amd$), rutile TiO_2(R) (tetragonal, $P4_2/mnm$), brookite TiO_2(Br) (orthorhombic, $Pbca$), and several metastable phases such as bronze-like TiO_2(B) (monoclinic, $C2/m$), hollandite-like TiO_2(H) (tetragonal, $I4/m$), ramsdellite-like TiO_2(Ra) (orthorhombic, $Pbnm$), columbite-like TiO_2(Co) (orthorhombic, $Pbcn$), fluorite-like cubic TiO_2(C) (cubic, $Fm\bar{3}m$), and baddeleyite-like TiO_2(Ba) (monoclinic, $P2_1/c$) [35–40]. Additionally, several amorphous forms of TiO_2 have also been reported [41, 42]. The main physicochemical characteristics of these TiO_2 polymorphs are summarized in Table 1.

Among the various TiO_2 polymorphs, TiO_2(A), TiO_2(R) and TiO_2(B) are the most commonly studied in batteries, offering chemically identical yet structurally distinct host lattices. Consequently, these polymorphs exhibit different lattice configurations, ion diffusion pathways, and surface energies, which significantly influence their ion storage behaviors. Among them, TiO_2(A) and TiO_2(R) occur naturally, whereas TiO_2(B) is a metastable polymorph synthesized under specific conditions. TiO_2(R) is the thermodynamically most stable phase under ambient conditions and is the most abundant in nature. However, its highly anisotropic ion diffusion results in kinetically constrained three-dimensional transport within micrometer-sized particles, limiting its performance as a negative electrode [45]. In contrast, TiO_2(A) demonstrates high surface activity, rapid charge storage through surface adsorption, and excellent structural stability, making it suitable for high-rate energy storage applications [22]. Meanwhile, TiO_2(B) features a unique open crystal framework with low-energy ion pathways extending from the surface to subsurface regions, which is believed to contribute to its pseudocapacitive charging behavior [46, 47].

For a long time, TiO_2 has been considered limited as an electrode material because its relatively dense crystalline structure and few open diffusion channels hinder ion transport. As a result, ion insertion is often confined to surface regions—especially in large crystals—leading to low ion diffusion coefficients. Nevertheless, TiO_2 remains one of the few transition metal oxides capable of insertion ions at a relatively low voltage (~1.5 V vs. Li^+/Li, ~0.8 V vs. Na^+/Na), while offering a theoretical specific capacity of 335 $mAh{\cdot}g^{-1}$ as a negative electrode material comparable to that of graphite/hard carbon negative electrodes. In practice, however, most reported Li^+/Na^+ insertion occurs near the surface to form Li/Na_xTiO_2 ($x < 0.5$) rather than through bulk insertion, resulting in measured capacities typically below ~168 $mAh{\cdot}g^{-1}$, depending on the crystal size. Although this value is lower than that of conversion- and alloying-type electrodes [48–50], TiO_2 provides superior cycling stability and a higher operating voltage [51]. This is particularly advantageous, as the sodiation voltage of hard carbon is close to the sodium plating potential, raising significant safety concerns [52]. Therefore, the relatively high operating voltage of TiO_2 improves safety,

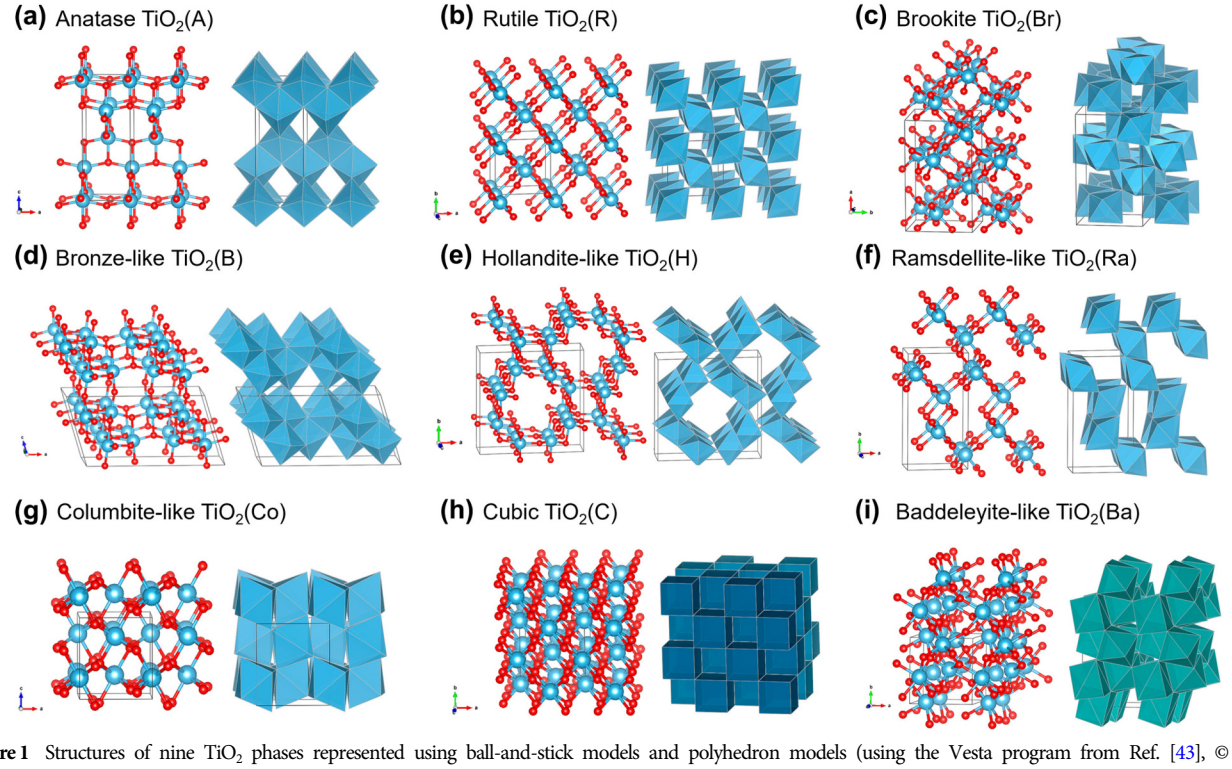

Figure 1 Structures of nine TiO_2 phases represented using ball-and-stick models and polyhedron models (using the Vesta program from Ref. [43], © 2011 International Union of Crystallography Printed in Singapore): (a) anatase TiO_2(A), (b) rutile TiO_2(R), (c) brookite TiO_2(Br), (d) bronze-like TiO_2(B), (e) hollandite-like TiO_2(H), (f) ramsdellite-like TiO_2(Ra), (g) columbite-like TiO_2(Co), (h) cubic TiO_2(C), (i) baddeleyite-like TiO_2(Ba). Red balls: O atoms; blue balls: Ti atoms. Unit cells are outlined using thin lines. Reproduced with permission from Ref. [44], © 2014 American Chemical Society.

positioning it as a promising candidate for both lithium- and sodium-ion storage applications.

Owing to its unique characteristics, TiO_2 has long been regarded as a highly promising material for ion storage, attracting substantial research attention and becoming a widely used electrode material in energy storage devices. Researches into the sodium-ion storage mechanisms of TiO_2 began later than in LIBs, emerging in the 21st century and accelerating significantly after 2014 (Fig. 2(a)). Building upon pioneering studies in LIBs, many researchers initially explained ion storage in TiO_2 based on the well-established insertion/extraction mechanism [41, 53–55]. However, certain experimental observations and characterization results have challenged this assumption, leading to notable discrepancies in the reported ion storage mechanisms. For example, several studies reported that both *ex situ* and *in situ* XRD patterns exhibited unchanged or reversible diffraction peaks of crystalline TiO_2 during ion insertion and extraction, suggesting a largely reversible structural response [54, 56–58]. In contrast, other

Table 1 Structural characteristics of 9 TiO_2 crystalline phases

Category	Naturally occurring phases			Metastable phases			High-pressure phases		
Phase	Anatase	Rutile	Brookite	TiO_2(B)	TiO_2(H)	TiO_2(Ra)	TiO_2(Co)	TiO_2(C)	TiO_2(Ba)
Crystal system	tetragonal	tetragonal	orthorhombic	monoclinic	tetragonal	orthorhombic	orthorhombic	cubic	monoclinic
Space group	$I4_1/amd$	$P4_2/mnm$	$Pbca$	$C2/m$	$I4/m$	$Pbnm$	$Pbcn$	$Fm\bar{3}m$	$P2_1/c$
Group #	141	136	61	12	87	62	60	225	14
a(Å)	3.7842	4.5941	9.184	12.1787	10.161	4.9022	4.515	4.516	4.589
b(Å)	3.7842	4.5941	5.447	3.7412	10.161	9.459	5.497	4.516	4.849
c(Å)	9.5146	2.9589	5.145	6.5249	2.97	2.9585	4.939	4.516	4.736
α(°)	90	90	90	90	90	90	90	90	90
β(°)	90	90	90	107.054	90	90	90	90	98.6
γ(°)	90	90	90	90	90	90	90	90	90
Density[a]($g \cdot cm^{-3}$)	3.895	4.248	4.123	3.734	3.461	3.868	4.329	5.761	5.092
Edge sharing[b]	4	2	3	—	—	—	—	—	—
Lattice energy[c] ($kJ \cdot mol^{-1}$)	24.75	0	18.53	49.16	73.05	68.49	8.86	147.78	155.55
CN(Ti)	6	6	6	6	6	6	6	8	7

[a] Calculated; [b] Per polyhedron; [c] Relative to that of rutile [44]; calculated at 0 K and 0 GPa.

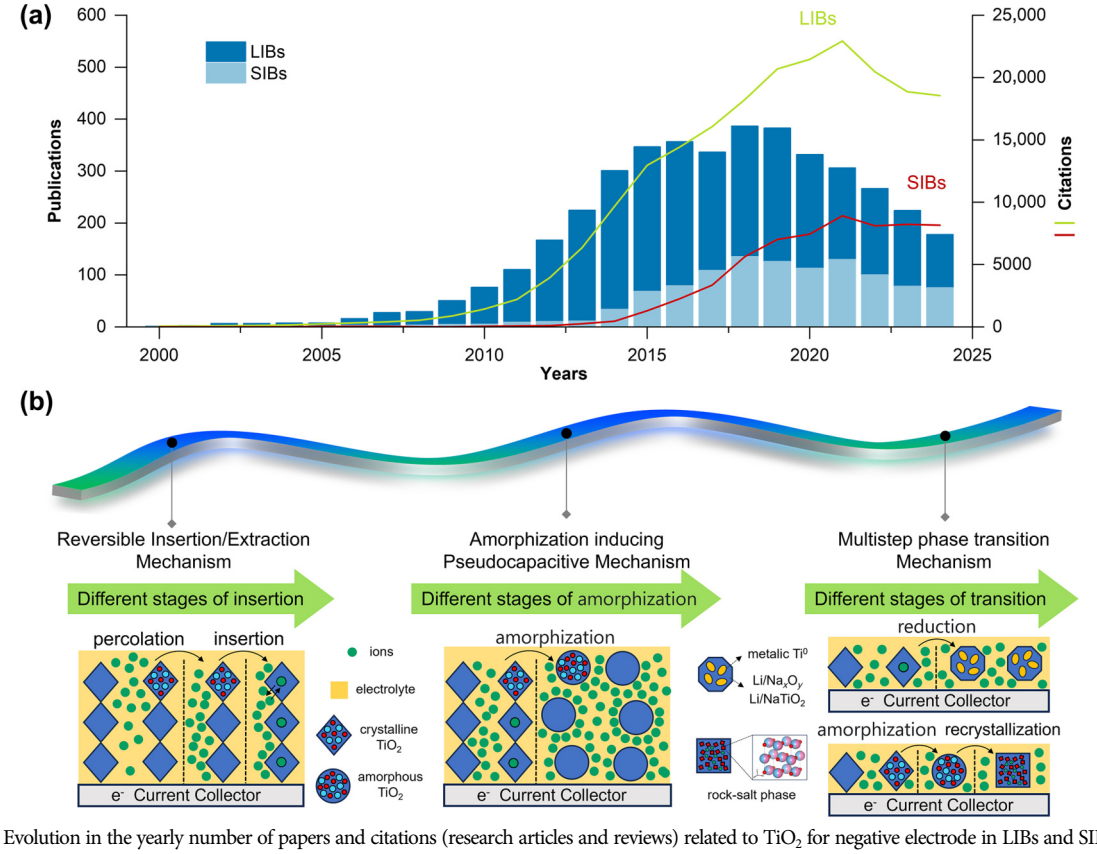

Figure 2 (a) Evolution in the yearly number of papers and citations (research articles and reviews) related to TiO_2 for negative electrode in LIBs and SIBs (Date from Web of Science). (b) Illustration of the three types of ion storage mechanisms in TiO_2: insertion, amorphization, and phase transition, which may occur independently or concurrently depending on particle size, cycling depth, and electrochemical conditions.

investigations, particularly those focusing on nanosized TiO_2, have revealed a complete loss of crystallinity following initial sodiation to 0.01 V (vs. Na^+/Na), with the material remaining amorphous during subsequent cycles [22, 36, 59, 60].

These conflicting findings have led to two competing interpretations: one supporting a reversible insertion/extraction mechanism without major structural phase transitions, and the other proposing an irreversible transformation from a crystalline to an amorphous state upon initial ion insertion. Interestingly, recent studies have further refined the latter interpretation by revealing that TiO_2 underwent a multistep electrochemically induced phase transformation—from a crystalline to an amorphous structure—followed by partial atomic rearrangement that leads to the *in situ* formation of rock-salt phase $Li/NaTiO_2$ nanograins during cycling [61–63].

Although these interpretations are supported by evidence from a range of advanced characterization techniques, a unified consensus on the reaction mechanism has not yet been reached. Therefore, a comprehensive review of the ion storage mechanisms in TiO_2 is essential, as it provides a fundamental basis for optimizing its electrochemical performance as a negative electrode in both LIBs and SIBs. Through systematic analysis, we have identified and summarized the predominant mechanisms reported to date, as illustrated in Fig. 2(b):

(a) Reversible ion insertion/extraction with minimal lattice distortion, typically observed in bulk TiO_2 particles; (b) Amorphization-induced pseudocapacitive behavior, prevalent in nanosized TiO_2, where structural disorder facilitates surface-controlled charge storage; (c) Multistep phase transformation mechanisms, which include two main scenarios: (i) formation and decomposition of Li_2O (or Na_2O) associated with the reduction and oxidation activity of metallic titanium; and (ii) an initial crystalline-to-amorphous transformation followed by partial structural rearrangement and *in-situ* generation of rock-salt-type $Li/NaTiO_2$ nanograins during subsequent cycling.

Although several mechanisms—such as reversible (de)intercalation and amorphization—have been proposed based on distinct experimental observations, they are not necessarily mutually exclusive. On the contrary, these processes may occur concurrently or sequentially within the same system at different stages of cycling. The extent to which partial recrystallization or rock-salt phase formation occurs is largely determined by the crystallite size of TiO_2. When the crystallite size is sufficiently small, complete amorphization followed by recrystallization can take place throughout the entire particle, leading to the disappearance of all XRD diffraction peaks. In contrast, larger particles typically experience only surface-limited amorphization and phase transition, while the bulk crystalline framework remains intact; hence, XRD reflections remain observable. This size-dependent structural evolution often accounts for the inconsistencies among reported results and contributes to the divergent interpretations of ion storage mechanisms in TiO_2-based electrodes.

2 Development of ion storage mechanisms in TiO_2

2.1 Chronological development in LIBs

Given that the majority of TiO_2 applications in batteries have historically focused on lithium-ion systems—and considering the chemical similarities between lithium and sodium, as well as the early reliance of SIB research on mechanisms derived from lithium-based systems. Therefore, before discussing the sodium-ion storage mechanisms, it is necessary to first review the lithium-ion storage behavior in TiO_2, which was also initially subject to controversy.

In this section, we briefly summarize the development of ion storage mechanisms in TiO_2 for LIBs from a chronological perspective. Since the 1970s, TiO_2 electrodes began to be investigated for use in LIBs, and the reaction mechanisms between lithium and TiO_2 were gradually elucidated through a series of studies. For example, in 1979, Ohzuku et al. [64] proposed a reaction mechanism based on XRD analysis, suggesting that the crystal structure of TiO_2(A) undergoes a transformation during discharge, resulting in the formation of $LiTiO_2$. They proposed the following reaction pathway: $TiO_2 \rightarrow Ti(Li^+)O_2 \xrightarrow{rearrangement} LiTiO_2$ where lithium ions diffuse into the TiO_2 lattice to form an intermediate $Ti(Li^+)O_2$, which subsequently rearranges into a cubic-phase $LiTiO_2$ (Fig. 3(a)). In 1981, Bonino et al. [65] studied TiO_2(A) with an average particle size of 0.25 μm and observed a flat discharge profile at a current density of 0.5 $mA{\cdot}cm^{-2}$ with a cut-off voltage of 1 V, consistent with a single-electron transfer process. However, their XRD analysis did not detect the characteristic peaks of $LiTiO_2$ (Fig. 3(b)), contradicting the hypothesis proposed by Ohzuku et al. [64]. However, Bonino et al.'s findings indicated the formation of another new phase, suggesting that the discharge process led to the generation of a novel stoichiometric compound rather than simple lithium-ion insertion into the TiO_2 lattice.

In 1988, Atlung et al. [66] further investigated the lithium storage behavior of three titanium dioxide polymorphs: TiO_2(A), TiO_2(R), and TiO_2(B). They observed a distinct two-phase equilibrium during lithium insertion into TiO_2(A), evidenced by a constant voltage plateau at 1.815 V (vs. Li^+/Li^0) in the electrochemical curves at 25 °C. When the temperature was raised to 120 °C, thereby enhancing ion diffusion, a second plateau emerged at 1.560 V (vs. Li^+/Li^0), and the lithium insertion ratio (x = Li/TiO_2, molar ratio) exceeded 0.5 (Fig. 3(c)). In contrast, lithium insertion into TiO_2(B) resulted in a sloped electrochemical profile without a distinct two-phase equilibrium. For TiO_2(R), no detectable lithium insertion was observed at 25 °C.

Furthermore, after lithium insertion, the electronic conductivity of both TiO_2(A) and TiO_2(B) increased significantly (measured on pressed powder pellets under 70 MPa), indicating a transition from insulating to conducting states. These findings suggest that Li–Li interactions during insertion are strongest in TiO_2(A), thereby promoting phase separation, whereas in TiO_2(B), the weaker attractive forces between inserted lithium atoms are insufficient to induce a two-phase transition.

In 2005, building on their previous promising work on transition metal oxides [67], Jean-Marie Tarascon's group further investigated the influence of crystal size reduction in TiO_2(A), with particle sizes ranging from 76.1 to 6.3 nm [68]. They discovered that nanostructuring extends the solid-solution domain at the onset of the electrochemical reaction during the first cycle (Fig. 3(d)). To distinguish between purely capacitive and insertion-based ion storage, atomic absorption spectrometry was employed to quantify the number of participating ions. The results revealed that decreasing crystal size significantly enhanced the pseudocapacitive behavior, a phenomenon that will be discussed in more detail in subsequent sections.

A year later, in 2006, Yong-Sheng Hu et al. [69] reported the electrochemical performance of nanosized TiO_2(R), which showed

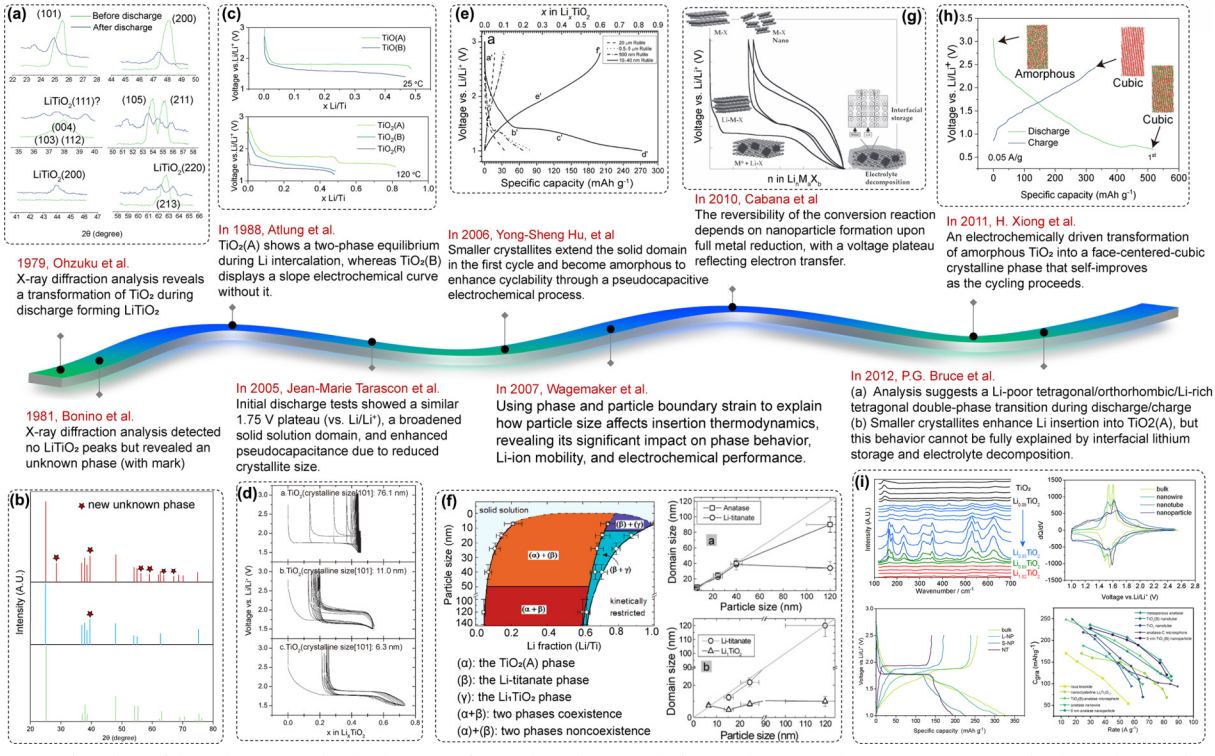

Figure 3 Brief timeline of the milestones in the development of TiO_2 electrode materials for LIBs battery applications. (a) In 1979, Ohzuku et al. Reproduced with permission from Ref. [64], © 1979 Published by Elsevier Ltd. (b) In 1981, Bonino et al. Reproduced with permission from Ref. [65], © 1981 Published by Elsevier B.V. (c) In 1988, Atlung et al. Reproduced with permission from Ref. [66], © 1988 Published by Elsevier B.V.(d) In 2005, Jean-Marie Tarascon et al. Reproduced with permission from Ref. [68], © The Royal Society of Chemistry 2005. (e) In 2006, Yong-Sheng Hu et al. Reproduced with permission from Ref. [69], © 2006 WILEY-VCH Verlag GmbH & Co. KGaA, Weinheim. (f) In 2007, Wagemaker et al. Reproduced with permission from Ref. [74], © 2007 American Chemical Society. (g) In 2010, Cabana et al. Reproduced with permission from Ref. [76] © 2010 WILEY-VCH Verlag GmbH & Co. KGaA, Weinheim. (h) In 2011, Hui Xiong et al. Reproduced with permission from Ref. [77] © 2012 American Chemical Society. (i) In 2012, Peter G. Bruce et al. Reproduced with permission from Ref. [78] © 2012 WILEY-VCH Verlag GmbH & Co. KGaA, Weinheim and from Ref. [79], © 2012 American Chemical Society.

unexpected advantages compared with its micrometer-sized counterpart (Fig. 3(e)). Although previous studies had generally reported negligible lithium insertion into TiO_2(R) [64, 65, 70], XRD, high resolution transmission electron microscope (HRTEM) and selected area electron diffraction (SAED) results indicated that irreversible structural changes at deeper lithium insertion levels (below 1.4 V during the first cycle). The formation of smaller crystalline grains and amorphous regions was identified as the cause of the sloped voltage profile observed during the second discharge process [71]. Notably, once this special nanocrystalline structure was formed, it remained stable and reversible during subsequent discharge/charge cycles, enabling excellent capacity retention. This improvement was attributed to surface-based lithium storage on nanosized particles rather than bulk insertion, a behavior particularly favorable for high-rate performance. It is important to acknowledge that this insightful concept, namely, the electrochemical transformation to an amorphous structure [72, 73], has significantly inspired further mechanistic studies on TiO_2 and will be elaborated upon in later sections.

In 2007, Wagemaker et al. [74, 75] employed neutron diffraction to investigate the structural evolution of TiO_2(A) (α-phase, the Li-poor phase) during lithiation across different particle sizes, aiming to elucidate the impact of particle size on lithium storage mechanisms. They introduced the concept of phase and particle boundary strain as a fundamental framework to explain the particle-size-dependent insertion thermodynamics. Their findings revealed that particle size played a critical role in governing phase behavior, lithium-ion mobility, and overall electrochemical performance (Fig. 3(f)). For instance, 7 nm TiO_2(A) particles could accommodate up to Li/Ti≈0.21, whereas larger particles (e.g., 120 nm) achieved only Li/Ti≈0.03. As particle size decreased, the Li-titanate phase (β-phase) became capable of incorporating more lithium, and particles around 7 nm in size could be fully transformed into Li_1TiO_2 (γ-phase, the Li-rich phase), thereby achieving the theoretical maximum capacity (Li/Ti = 1).

However, the Li_1TiO_2 phase exhibits poor ionic conductivity due to the full occupation of octahedral voids, which hinders lithium-ion diffusion. This kinetic limitation prevents the formation of the γ-phase in larger particles, as indicated by the "kinetically restricted" region in the phase diagram. In contrast, the reduced diffusion path in nanosized particles alleviates this limitation, allowing complete transformation into Li_1TiO_2 and enabling solid-solution reactions to occur even at room temperature. These results explain why smaller particles can undergo full conversion to the Li-rich phase, while bulkier particles are constrained by sluggish ion diffusion during bulk insertion. Nonetheless, the study appears to have overlooked the surface adsorption–dominated mechanism proposed earlier by Y. S. Hu and Maier et al. [69], which also contributes significantly to lithium storage in nanosized TiO_2.

In 2010, Cabana et al. [76] systematically summarized the aforementioned mechanisms and highlighted the behavior of transition metal oxides (including TiO_2) that underwent conversion reactions in LIBs when used as electrode materials (Fig. 3(g)). Many transition metal compounds lack vacant sites in their crystal structures, making conventional insertion reactions

thermodynamically or kinetically unfavorable. As a result, such materials were initially disregarded as potential electrodes. To explain the observed large irreversible capacity losses and amorphous structural transformations commonly associated with metal oxide negative electrodes, alloying and conversion reaction mechanisms were subsequently proposed.

The conversion mechanism, in particular, involves the complete reduction of the transition metal and the simultaneous formation of a lithium-containing binary compound matrix (e.g., Li_2O). The reversibility of this process appears to depend on the repeated formation and decomposition of this matrix during cycling. Notably, this mechanism differs fundamentally from the well-established insertion/deinsertion and alloying processes, offering a distinct route to energy storage in TiO_2 and other metal oxide electrodes. In 2011, H. Xiong et al. [77] synthesized amorphous TiO_2 nanotubes (TiO_2NTs) via electrochemical anodization of titanium foil for use as electrodes in lithium half-cells. Using a combination of synchrotron XRD, X-ray absorption spectroscopy (XAS), HRTEM, and computational methods, they were the first to report an electrochemically driven transformation of amorphous TiO_2NTs into a cubic crystalline phase. This newly formed cubic phase, with a stoichiometry approaching $Li_1Ti_1O_2$, exhibited excellent long-term cycling stability and enhanced capacity and power performance. Their XRD analysis showed no significant structural changes during cycling above 1.1 V. However, cycling at potentials below 1.1 V induced a distinct voltage plateau, indicative of an irreversible phase transition and the formation of a new crystalline phase (Fig. 3(h)). This phase exhibited a highly symmetric rock-salt structure, in which Ti and Li atoms were randomly distributed among all octahedral sites within an almost ideal cubic close-packed oxygen lattice. Further calculations revealed that lithium-ion diffusion in the cubic $LiTiO_2$ structure had a remarkably low activation energy barrier of 0.257 eV, substantially lower than that in TiO_2(A) (~0.5 eV). Moreover, molecular dynamics simulations indicated that Li^+ diffusion in the fully lithiated cubic $LiTiO_2$ phase was faster than in fully lithiated amorphous TiO_2NT, explaining its superior power capability.

These findings suggest that the insertion/extraction of Li^+ ions in TiO_2NTs triggers a structural evolution into a new crystalline phase that is better suited for high-performance energy storage. This electrochemically induced phase transformation presents a modular and tunable approach for designing novel battery materials with tailored physical and chemical properties—a concept that will be explored further in subsequent sections.

In 2012, the group led by Peter G. Bruce [78, 79] further analyzed the lithium storage mechanisms of TiO_2(A) and TiO_2(B). Thery found that TiO_2(A) underwent a multi-phase transition sequence, comprising a Li-poor tetragonal phase (Li_xTiO_2, x<0.08), an orthorhombic phase (Li_xTiO_2, x=0.5) and a Li-rich tetragonal phase (Li_xTiO_2, x=1), analogous to the mechanism previously reported by Wagemaker et al. (Fig. 3(l)). The discharge curves revealed three distinct voltage regions: Region A (slope area from 2 to 1.75 V), Region B (plateau area of 1.75 V)), and Region C (from 1.75 to1.0 V, a pseudo-plateau followed by a sloping tail).

In region A, most studies attributed the behavior to lithium insertion into the Li-poor tetragonal anatase lattice via a solid-solution mechanism [46, 68, 74, 76, 80]. Other studies, however, suggested that lithium storage in this region was also involved surface adsorption [69, 81–83]. Both mechanisms proceed without phase nucleation and are strongly influenced by reduced particle and crystal size. Region B is characterized by a typic two-phase coexistence between the orthorhombic $Li_{0.5}TiO_2$ phase and the Li-poor tetragonal Li_xTiO_2 phase. The length of plateau increased with particle size, as the two-phase transformation is thermodynamically sluggish, particularly in bulk materials [84]. In Region C, the low-voltage sloping tail is more pronounced in samples with smaller crystal sizes, allowing further lithium insertion into TiO_2. Some studies attributed this to the formation of a Li-rich tetragonal phase ($Li_{0.5+x}TiO_2$), where x is size-dependent. Others proposed that interfacial lithium storage [81–83] or electrolyte decomposition and solid electrolyte interphase (SEI) formation [47, 85]. To clarify the origin of this region, researchers compared different TiO_2(A) samples with different surface areas, including nanotubes (NT, 220 $m^2 \cdot g^{-1}$), mesoporous nanoparticles (M-NP, 205 $m^2 \cdot g^{-1}$) [86], and small nanoparticles (S-NP, 286 $m^2 \cdot g^{-1}$). Unexpectedly, NT (218 $mAh \cdot g^{-1}$) and M-NP (202 $mAh \cdot g^{-1}$), which had smaller surface areas, delivered higher capacities in Region C than S-NP (175 $mAh \cdot g^{-1}$). These results suggest that interfacial lithium storage and electrolyte decomposition may not fully account for the capacity in Region C, as such mechanisms would typically scale with surface area.

In the same year, Belak and van der Ven et al. [87] conducted a comprehensive first-principles statistical mechanical study to investigate the thermodynamic and kinetic properties of the lithiation process in TiO_2(A). Their results shed light on the fundamental limitations of this material in LIBs. Although the tetragonal unit cell of TiO_2(A) can theoretically host one lithium per titanium atom, bulk TiO_2(A) typically only achieved $Li_{0.5}TiO_2$, undergoing a tetragonal-to-orthorhombic phase transition commonly reported as the upper limit of lithium insertion [88, 89]. However, in $Li_{0.5}TiO_2$, lithium diffusion is restricted to one dimension along strain-invariant interfaces, hindering ion transport across phase boundaries and limiting capacity [90]. Only nanostructured TiO_2(A) can support full lithiation to $LiTiO_2$. Furthermore, first-principles calculations revealed that lithium diffusion in the fully lithiated Li_1TiO_2 phase was significantly lower than in TiO_2 or $Li_{0.5}TiO_2$, due to the absence of distorted Ti–O octahedra, which otherwise facilitated ion mobility. This transition and reduction ion diffusion are analogous to those observed in previous studies.

In brief, substantial progress has been made in elucidating the electrochemical behavior of TiO_2 in LIBs, with the insertion/extraction mechanism remaining the most widely accepted framework. However, two critical factors warrant further attention: (a) Crystal size plays a pivotal role in ion storage behavior and should be considered a key parameter in material design; (b) First-cycle capacity loss cannot be fully explained by interfacial lithium storage or electrolyte decomposition alone. It is therefore essential to investigate whether lithium insertion induces structural or textural modifications, potentially leading to phase transitions.

We strongly recommend that researchers focus on the first cycle, as irreversible capacity loss at deeper lithiation levels (below 1 V) suggests underlying structural changes. In particular, the irreversible formation of nanoscale crystalline grains and amorphous regions reported by Jean-Marie Tarascon and Yong-Sheng Hu et al. [67, 69], as well as the electrochemically induced transformation of amorphousTiO_2 into a cubic crystalline phase observed by Xiong et al. [77], merit continued investigation.

Based on a chronological analysis of the literature and experimental evidence, we identify three prevailing ion storage mechanisms as follows: (a) a reversible ion insertion/extraction mechanism, (b) an amorphization-induced pseudocapacitive

mechanism, and (c) a multistep phase transition mechanism. Although these mechanisms originate from distinct experimental observations, they are not necessarily mutually exclusive. On the contrary, they may operate concurrently or sequentially within the same system, depending on the material structure, cycling conditions, and state of charge, as will be discussed later.

2.2 Reversible insertion/extraction mechanism

Building on the success of TiO_2 as a negative electrode for LIBs, its potential application in SIBs has garnered growing interest. However, sodium exhibits distinct physical and chemical properties, such as a larger ionic radius and different thermodynamic behavior, which may result in fundamentally different storage mechanism in TiO_2. For instance, while lithium can intercalate into graphite, Na-intercalated graphite compounds are thermodynamically unstable [91]. Consequently, the larger Na^+ radius and sluggish diffusion kinetics induce greater lattice strain and localized disorder in TiO_2, thereby enhancing ion insertion–induced lattice distortion. This process ultimately causes the surface crystalline layer of TiO_2 to undergo amorphization, which serves as the crucial precursor for nucleation and the subsequent formation of cubic rock-salt $Li/NaTiO_2$ nanograins. However, in contrast to the relatively well-understood lithium-ion storage in TiO_2, sodium-ion storage remains more elusive, with conflicting reports in the literature posing a major challenge to the development of high-performance TiO_2-based negative electrodes. Therefore, the following section focuses on the sodium storage mechanism of TiO_2, critically examining the historical development and ongoing debate surrounding its storage mechanism.

The first study employing TiO_2 as a negative electrode in SIBs was also conducted by H. Xiong et al. , who directly grew amorphous TiO_2NTs on titanium foil via same electrochemical anodization (Fig. 4(a)). The sodium storage performance of TiO_2NTs was evaluated using 1 M $NaClO_4$ in propylene carbonate (PC) as the electrolyte and sodium metal as the counter electrode. The results showed that only large-diameter amorphous TiO_2NTs (inner diameter>80 nm) exhibited a gradually increasing capacity of up to 120 mAh·g^{-1} at 50 mA·g^{-1} (Fig. 4(b) and inset), whereas narrower nanotubes (<45 nm inner diameter, 10 nm wall thickness) and crystalline phases such as anatase and rutile did not exhibit significant Na^+ insertion. From these findings, the authors inferred that the significant size mismatch between Ti and Na ions, along with the higher Na^+ diffusion barrier compared to Li^+, requires a higher sodium concentration to establish a sufficient electric field for effective insertion.

Furthermore, XAS revealed a reduction in the Ti oxidation state upon Na^+ insertion, confirming successful Na^+ insertion into

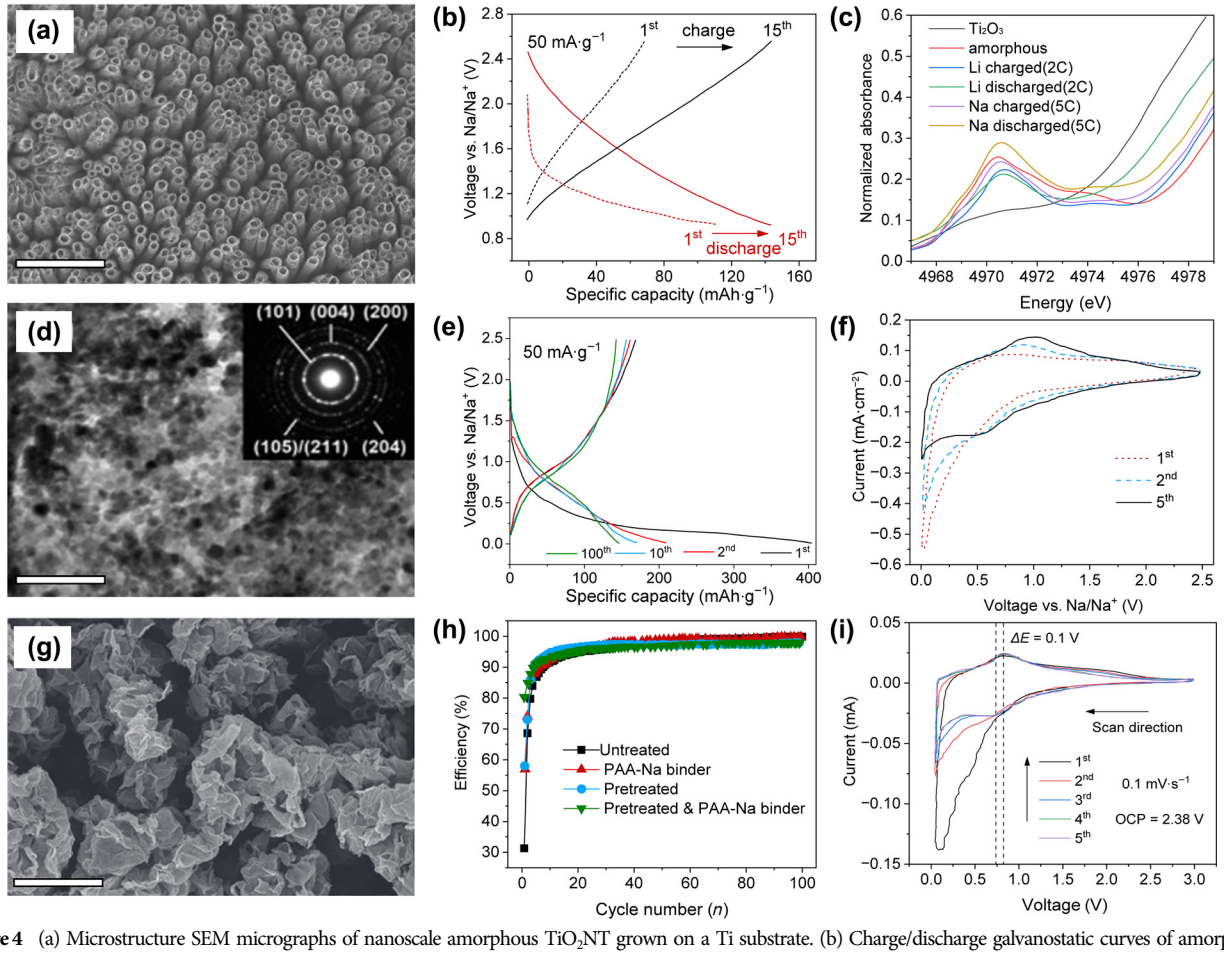

Figure 4 (a) Microstructure SEM micrographs of nanoscale amorphous TiO_2NT grown on a Ti substrate. (b) Charge/discharge galvanostatic curves of amorphous 80 nm I.D. TiO_2NT in Na half cell (red for discharge and black for charge) cycled between 2.5 and 0.9 V versus Na/Na$^+$ at 50 mA·g^{-1}. (c) Ti K-edge XANES spectra of TiO_2NT electrodes in Pre-edge region. (a-c) Reproduced with permission from Ref. [41], © 2011 American Chemical Society. (d) TiO_2(A) nanocrystals (ANC), TEM with indexed SAED and lattice fringe inserts. (e) Charge/discharge galvanostatic curves of ANC, tested at a rate of 50 mA·g^{-1}. (f) CV curves of ANC, tested at a rate of 1 mV·s^{-1}. (d-f) Reproduced with permission from Ref. [93], © 2013 The Royal Society of Chemistry. (g) High-magnification SEM image for G-TiO_2. (h) Efficiencies of the four G-TiO_2 electrodes with different treatments. (i) CV curves of G-TiO_2 (scan rate: 0.1 mV·s^{-1}). (g–i) Reproduced with permission from Ref. [94], © 2015 Macmillan Publishers Limited.

amorphous TiO_2NTs. However, X-ray absorption near-edge structure (XANES) spectra indicated increased crystallinity in TiO_2NTs after Na^+ insertion (Fig. 4(c)). This structural evolution suggests that Na^+ insertion promotes the development of medium-range order in amorphous TiO_2NTs upon cycling, as evidenced by the emergence of main-edge peaks resulting from higher-order multiple scattering [92].

Although ion storage initially follows a surface-controlled capacitive mechanism due to the rapid diffusion in the amorphous TiO_2NTs structure, prolonged cycling induces a gradual transition to a mixed mechanism, incorporating both diffusion-controlled and capacitive processes. This evolution coincides with the enhanced crystallinity in TiO_2NTs. This phenomenon may indicate the *in-situ* formation of new phases, which will be further discussed in the phase transition section.

Two years later, Xu and Mitlin et al. [93] further reported that crystalline TiO_2(A) nanomaterials (ANC, Fig. 4(d)) for SIBs also operate based on a reversible Na-ion insertion–extraction behavior. They claimed that the current observed at 0.8–0.0 V during the first cathodic scan in cyclic voltammetry (CV) is attributed to the irreversible formation of the SEI with a relatively low initial Coulombic efficiency (ICE) of 41.9%. However, similar to LIBs, electrolyte decomposition alone may not fully account for the observed first-cycle capacity loss. Given that metal oxides typically exhibit fewer interfacial side reactions and higher Na^+ diffusion energy barriers, the first-cycle irreversibility is more likely associated with sodium insertion-induced structural or textural changes. These modifications may trigger an amorphization process and result in the irreversible trapping of sodium within the TiO_2 lattice during the initial cycle, a phenomenon that will be discussed in further detail in subsequent sections.

In 2015, Chen et al. [94] demonstrated that the Na^+ insertion in TiO_2/graphene nanocomposites (G-TiO_2, Fig. 4(g)) enabled high-rate capability and long cycle life in SIBs, primarily through a pseudocapacitance storage mechanism rather than a conventional insertion or alloying reaction. This hybrid G-TiO_2 electrode delivered a specific capacity of exceeding 90 mAh·g^{-1} at an ultrahigh current density of 12,000 mA·g^{-1} (36C), with an average voltage plateau around 0.8 V. The voltage is notably lower than those typically observed in LIBs, such as 1.4 V for TiO_2(R), 1.5 V for TiO_2(B) and 1.75 V for TiO_2(A) [46, 68, 69]. The lower plateau suggests that sodium insertion into TiO_2 requires a higher electrochemical driving force, likely due to the greater ionic radius of Na^+ and its associated higher diffusion barrier compared to Li^+.

Furthermore, a significant irreversible capacity loss was observed during the initial cycles, with an ICE of only 31.4%. The irreversible behavior observed in CV curves during early cycles further supports the occurrence of a structural phase transition into an amorphous state. This amorphization process is believed to be responsible for the emergence of pseudocapacitive behavior in the G-TiO_2 electrode, an effect that will be discussed in more detail in later sections.

Among the proposed sodium storage mechanisms, the insertion/deinsertion mechanism remains the most widely accepted. To investigate this predominantly reversible insertion process, numerous studies have employed *ex-situ* and *in-situ* characterization techniques, which often reveal unchanged diffraction peaks of crystalline TiO_2 in both sodiated and desodiated states, supporting a reversible insertion mechanism without significant structural changes [54, 56, 57, 95]. For example, in 2014, Khalil Amine et al. [54] synthesized pitch carbon-coated TiO_2(A) nanorods via a hydrothermal method. These nanorods exhibited a large initial discharge capacity exceeding 700 mAh·g^{-1} but a charge capacity of only 193 mAh·g^{-1}, resulting in an ICE of less than 30% (Fig. 5(a)). Remarkably, even when the discharge cutoff voltage was raised to 0.8 V, the irreversible capacity loss still exceeded 300 mAh·g^{-1} (with ICE < 2%). Since such high voltages are unlikely to trigger significant side reactions with the electrolyte [96, 97], this observation highlights the importance of understanding the irreversible processes linked to the phase transition process.

Ex-situ XANES analysis indicated significant spectral shifts between point 3 and 4 (curve *x* in Fig. 5(b) and inset corresponding to point *x* in Fig. 5(c)). These included a shift to lower energies and a slight enhancement of the edge-front peaks (see inset of Fig. 5(b)), which were attributed to ligand-field changes associated with amorphization. Although partial recovery of the spectrum was observed upon charging, the pre-edge features did not fully return to those of the pristine TiO_2(A) electrode, indicating an irreversible alteration in the local structure or ligand environment. If the conversion reaction were dominant, the TiO_2(A) structure would be expected to irreversibly transform into metallic Ti at full discharge.

However, based on *ex-situ* XRD, high-resolution TEM, and SAED pattern analyses (Figs. 5(c) and 5(d)), the authors reported that the TiO_2(A) framework did not convert into Ti metal or a fully amorphous phase, even after deep discharge to 0.01 V. Instead, it retained structural integrity and exhibited a reversible $Ti^{4+/3+}$ redox process, even after prolonged cycling. A year later, Yang-Kook Sun et al. [56] further emphasized that the sodium-ion storage mechanism in TiO_2(A) was predominantly governed by the reversible insertion/extraction of Na^+ into/out of the anatase phase, based on $Ti^{4+/3+}$ redox couple. This conclusion was supported by the fact the observed capacity does not exceed the theoretical limit, and no additional peaks are detected in the XRD patterns (Fig. 5(e)).

However, the absence of the (101) main peak, coupled with the rapid oxidation of discharged (sodiated) electrodes upon exposure to air may compromise the reliability of the *ex-situ* XRD data. Moreover, the blurred SAED pattern after discharge (Fig. 5(d), inset 4) suggests a loss of long-range crystallinity, an indication of partial amorphization. Interestingly, after 100 cycles, the reappearance of distinct diffraction spots in the SAED pattern indicates partial recrystallization during cycling, a phenomenon that was overlooked in their discussion and will be further examined in the section on multistep phase transitions, as it may involve the formation of a new rock-salt phase.

Similar reversible insertion/extraction mechanism has been reported in recent studies. For example, Li et al. [98] used *in-situ* XRD to show that the primary diffraction peaks of TiO_2(A) did not shift during cycling, and no new peaks emerged (Fig. 5(f)). *In-situ* Raman spectroscopy further revealed that the 152 cm^{-1} peak, attributed to the Ti–O stretching vibration on the (101) plane, exhibited a reversible behavior similar to the *in-situ* XRD results (Fig. 5(h)), indicating nearly reversible Na^+ insertion/extraction.

However, closer inspection of the XRD region between 23.5° and 26.5° (Fig. 5(f), inset color mapping) showed a gradual decline in peak intensity during initial sodiation. This behavior was attributed to an amorphous process, in which TiO_2(A) irreversibly transforms into a sodiated amorphous phase during the first cycle. This interpretation was supported by XPS fitting of electrodes discharged to various states of charge (SOC) (Fig. 5(g)). At a discharge cutoff of 0.01 V (State 4), approximately 0.70 Na^+ was inserted per TiO_2 unit ($Na_{0.7}TiO_2$), while at the end of charging

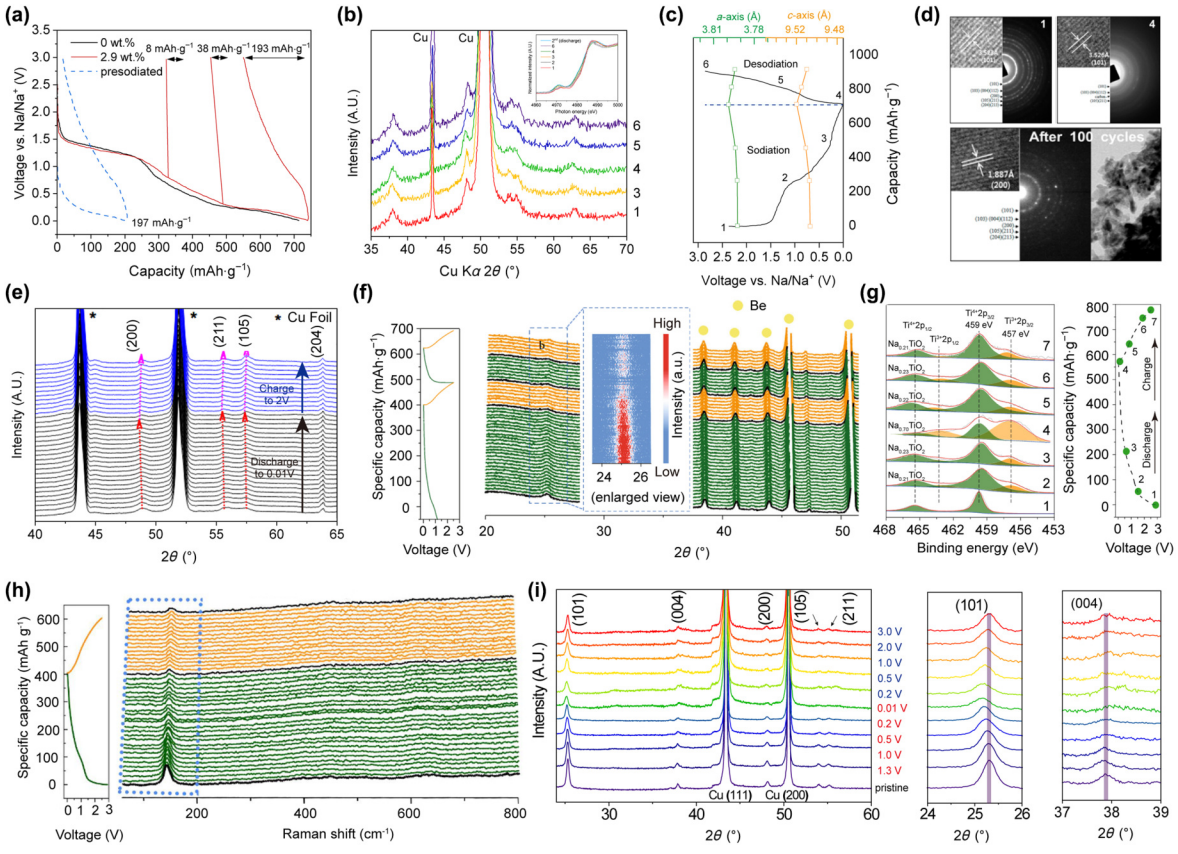

Figure 5 Schematic illustration of the reversible insertion/extraction behavior of TiO_2. (a) First discharge curve of different carbon-coated nanorod TiO_2(A). (b) *Ex-situ* XRD patterns and (inset) XANES K-edge spectra of 2.9 wt.% carbon-coated TiO_2(A) nanorods at various states of charge (SOC) with each spectrum corresponding to a different SOC point as shown in (c) corresponding charge–discharge curve. (d) HR-TEM images and SAED pattern of the pristine sample (points 1 and 4), and SAED pattern with TEM image of extensively cycled electrode. (a-d) Reproduced with permission from Ref. [54], © 2014 American Chemical Society. (e) *ex-situ* XRD patterns of TiO_2(A). Reproduced with permission from Ref. [56], © 2015 Elsevier Ltd. (f) *In-situ* XRD patterns of TiO_2(A) in the 20.0°–55.0° diffraction range and the surface color mapping between 23.5° and 26.5° (inset). (g) Ti 2p XPS spectra of TiO_2(A) collected at different SOC. (h) *in-situ* Raman spectra of TiO_2(A) in the 50.0–800.0 cm^{-1}. (f-h) Reproduced with permission from Ref. [98], © 2022 Li, F. J. et al. (i) *ex-situ* XRD patterns of TiO_2(A) during 1st cycle with enlarged (101) and (004) crystal face inset. Reproduced with permission from Ref. [58], © 2024 Wiley-VCH GmbH.

(State 7), approximately 0.2 Na^+ remained irreversibly trapped, further supporting the irreversible nature of the first-cycle amorphous process. However, a detailed mechanistic explanation of this transformation remains lacking.

Nevertheless, a significant irreversible capacity loss is typically observed during the first cycle, followed by a gradual decrease in the intensities of XRD diffraction peaks during subsequent cycles, an evolution that remains poorly understood. To explain these phenomena, one could consider the conversion reaction mechanism proposed by Jean-Marie Tarascon and Wu et al. [49, 67], in which TiO_2 was reduced to metallic Ti during deep sodiation. If this mechanism were dominant, XRD patterns should exhibit a characteristic diffraction peak of metallic Ti at 40.2° (Cu Kα, λ=1.5406 Å), along with features indicative the formation of amorphous binary compound matrix (e.g., Na_2O). Interestingly, in a separate study, a gradual reduction in the intensities of all diffraction peaks was clearly observed during the discharge (Fig. 5(i)) [58], strongly suggesting that TiO_2 transitions into an amorphous state after the first cycle. However, their SAED patterns obtained after 10,000 cycles revealed the emergence of crystalline diffraction rings, implying that a crystalline structure is reformed during long-term cycling. This structural reorganization, potentially representing a reversible amorphous-to-crystalline transition, will be discussed in detail in the following multistep phase transformation section.

2.3 Amorphization inducing pseudocapacitive mechanism

While early studies described ion storage in TiO_2 as a purely insertion-driven process, discrepancies in experimental observations suggest that the underlying storage mechanisms are more complex and require further investigation. For example, multiple reports have shown that upon discharging to low potentials, the main diffraction peaks of TiO_2 gradually disappeared or exhibit significant broadening, indicative of an amorphization process. Even after recharging to 3.0 V, the original crystalline structure was not recovered, suggesting an irreversible amorphous transformation during the initial sodium insertion [22, 36, 59]. Other studies focusing on nanosized TiO_2 particles (crystal size < 10 nm) have reported complete loss of crystallinity after the first discharge to 0.01 V, with the amorphous state remaining stable throughout subsequent electrochemical cycles [77, 99].

For instance, Cha et al. [60] synthesized TiO_2(A) nanoparticles (5–8 nm) via a hydrothermal method and observed, through *ex-situ* XRD and TEM analyses (Fig. 6(a)), a clear loss of crystallinity upon sodiation, suggesting a structural phase transformation. Additionally, the originally white TiO_2(A) electrode turned black after discharge, implying the formation of a new phase. Interestingly, after washing the discharged electrode with

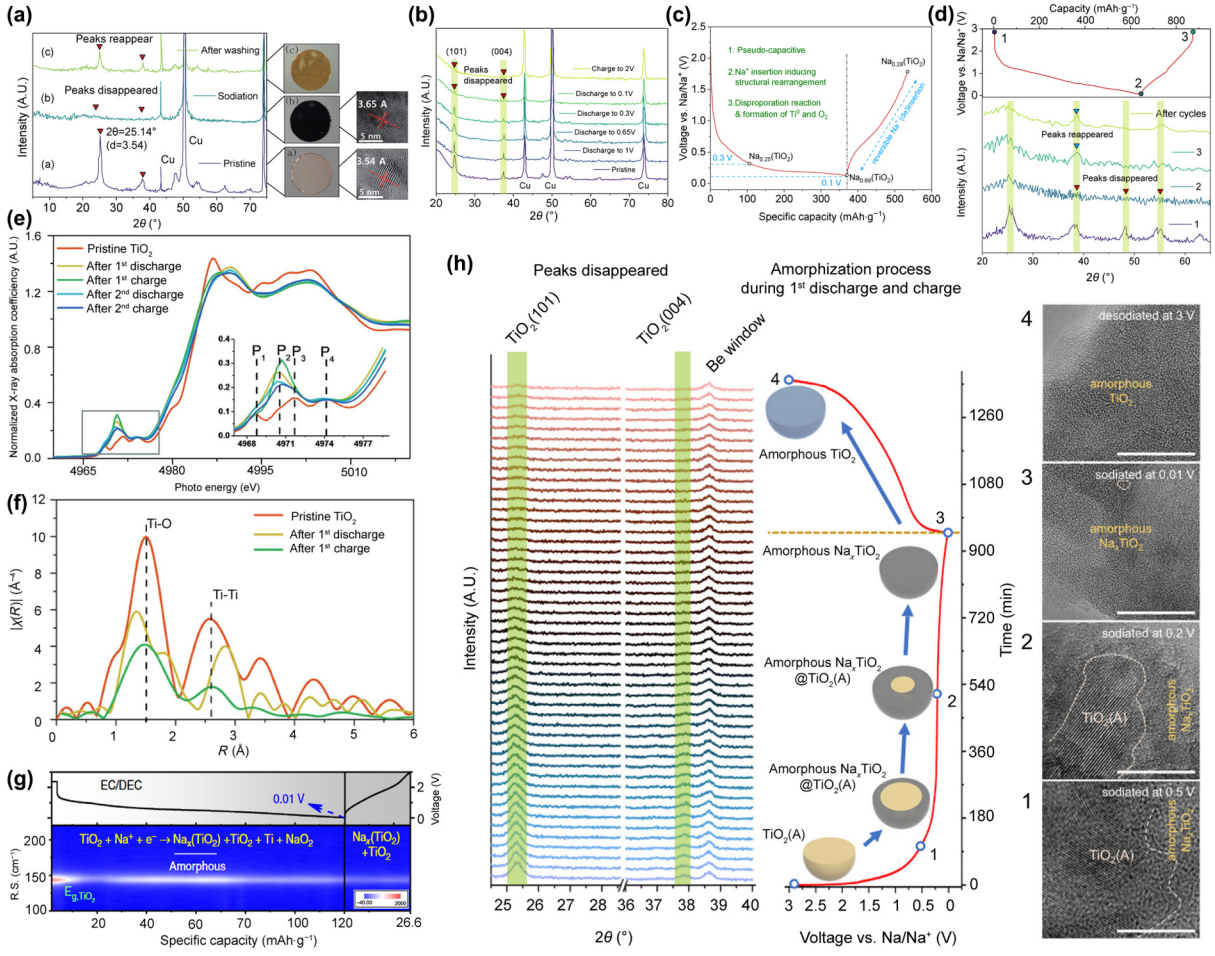

Figure 6 Schematic illustration of the amorphous phase transition behavior of TiO_2. (a) XRD patterns of TiO_2 electrodes in three different states. a. pristine (black line; white-colored electrode). b. After sodiation (red line; black-colored electrode). c. After washing with deionized water (blue line; yellow-colored electrode). Reproduced with permission from Ref. [60], © 2014 The Royal Society of Chemistry. (b) XRD patterns of pristine and cycled electrodes at different SOC reveal that nearly all anatase-related reflections disappear completely after discharging. (c) Schematic illustration of the conversion reaction mechanism, involving the formation of metallic titanium, sodium superoxide, and an amorphous sodium titanate phase. (b, c) Reproduced with permission from Ref. [49], © 2014 WILEY-VCH Verlag GmbH & Co. KGaA, Weinheim. (d) XRD patterns of TiO_2 at different electrochemical states: (1) pristine, (2) after the first discharge to 0.01 V, (3) after the first charge to 3 V, and (after cycles) at 3 V after five cycles at 1 C. Reproduced with permission from Ref. [51], © 2017 American Chemical Society. (e) Ti-K edge XANES spectra of TiO_2 during the first two cycles. (f) Corresponding FT magnitude of k^3-weighted EXAFS spectra. (e, f) Reproduced with permission from Ref. [36], © 2018 WILEY-VCH Verlag GmbH & Co. KGaA, Weinheim. (g) *In-situ* Raman spectroscopy of TiO_2(A) during the first cycle using an EC/DEC-based electrolyte (R.S.: Raman shifts). Reproduced with permission from Ref. [59], © 2019 Li, K. K. et al. (h) *In-situ* XRD patterns and corresponding *ex-situ* HR-TEM images at different SOC indicate a continuous crystalline-to-amorphous transition initiating at the particle surface and gradually progressing inward. Scale bar: 10 nm. Reproduced with permission from Ref. [22], © 2023 Wei, Q. L. et al.

deionized water, the TiO_2(A) diffraction peaks reappeared, indicating partial reversibility. Similarly, Passerini et al. [49] observed a gradual decline and eventual disappearance of TiO_2(A) XRD reflections upon sodiation in nanoparticulate samples (<30 nm). As shown in Fig. 6(b), anatase-related peaks vanished almost entirely at the end of discharge (0.1 V) and did not recover upon charging to 2 V. This significant irreversible capacity led the authors to suggest that a conversion-like mechanism may be involved (Fig. 6(c)). In this mechanism, TiO_2(A) initially forms an intermediate sodium titanate phase, which then disproportionates into a secondary sodium titanate phase and is partially reduced to metallic titanium, a hypothesis that will be discussed in phase transition section later.

Le et al. [51] synthesized nanosized TiO_2(A) (average grain size ~8.1 nm, calculated via the Scherrer equation) using a microwave-assisted solvothermal method. *Ex-situ* XRD analysis revealed that nearly all diffraction peaks of the fresh electrode (Fig. 6(d), position 1) disappeared after discharge to 0.01 V (position 2), indicating a complete transition to an amorphous structure upon sodium insertion. Upon recharging to 3 V (position 3), crystallinity was partially recovered, though with notable shifts in peak positions and intensities, which was consistent with the findings reported by Han et al. [58] This partially reversible amorphous phase was maintained after five galvanostatic cycles at 1 C, suggesting structural reversibility following the first cycle.

The amorphization process was further confirmed by XAS analysis [36]. The results demonstrated that the local bonding environment of the electrode material evolved during the discharge/charge process, indicating that the TiO_2(A) electrode undergoes amorphization during the first sodiation, and that the resulting amorphous phase exhibits pseudocapacitive sodium storage behavior in subsequent cycles. Specifically, after the first sodiation, a new peak (P2) at 4970.7 eV emerged, which is recognized as a characteristic feature of amorphous sodium titanate within the pre-edge region (4968–4977 eV) of the XANES spectra. Even after desodiation, the electrode displayed a broad

peak near P2, resembling the spectral features of amorphous TiO_2(A) reported in the literature, though its precise interpretation remains inconclusive. Moreover, the absence of the characteristic TiO_2(A) fingerprint after the first charge supports the irreversible amorphization of the TiO_2(A) electrode upon sodiation (Fig. 6(e)).

In contrast, Bella et al. [100] proposed a contradictory conclusion that challenges the amorphization conversion mechanism. They compared the electrochemical behaviors of amorphous nanotubular TiO_2 (80 nm diameter), prepared by anodic oxidation on Ti foil, and crystalline TiO_2(A), obtained via thermal annealing at 450 °C in air. The amorphous sample exhibited continuous capacity fading, while the crystalline sample showed an abrupt capacity enhancement after several cycles. According to the previous discussion, Na^+ insertion into TiO_2(A) is expected to induce structural changes or generate new crystalline phases. However, their *ex-situ* XRD analysis showed that the crystallinity of both samples remained unaffected by sodiation and desodiation, with no evidence of sodium titanate or metallic Ti phases observed in their XRD. It is important to note that the nanotubular TiO_2 produced via anodic oxidation is typically too thick to enable effective Na^+ diffusion, which may suppress amorphization and hinder the detection of phase transitions. This kinetic limitation may partially explain the inconsistencies reported across different studies regarding the amorphization storage mechanism of TiO_2.

More importantly, Tong-Yi Zhang et al. [59] found that electrolyte also played a vital role in the amorphization process of TiO_2. They synthesized TiO_2(A) nanocrystals (~16 nm) using a solvothermal method and compared the electrochemical behavior in two different electrolytes: diglyme-based and EC/DEC-based systems. A clear difference in ICE was observed between the two electrolytes. *In-situ* Raman spectroscopy further revealed distinct structural evolutions depending on the electrolyte used (Fig. 6(f)). In the EC/DEC-based electrolyte, full amorphization of TiO_2 was achieved only after approximately four cycles, indicating lower accessible capacity. In contrast, in the diglyme-based electrolyte, amorphization occurred entirely during the first discharge, enabling higher Na^+ storage. Moreover, CV dynamic analysis showed significantly lower polarization in the diglyme-based system, suggesting more favorable sodiation kinetics for the TiO_2 electrode. This difference in kinetics may also help explain the conflicting reports regarding the extent of amorphization in earlier studies.

Inspired by these findings, Xu and Wei et al. [22, 36] also employed a diglyme-based electrolyte and, through a combination of *in-situ* and *ex-situ* techniques, confirmedthat TiO_2(A) electrode underwent amorphization during the first sodiation process. The resulting amorphous phase exhibited pseudocapacitive sodium storage behavior during subsequent cycles.

In-situ XRD revealed that as the electrode was discharged from 3 to 0.5 V, the intensity and shape of the primary (101) diffraction peak remained unchanged, indicating the preservation of the pristine anatase structure. However, further discharge to 0.01 V resulted in peak broadening and eventual disappearance (Fig. 6(g)), confirming the amorphization of the TiO_2 structure. During the following desodiation process, the amorphous phase was retained. *Ex-situ* HRTEM images of TiO_2 at different sodiation states showed a progressive shrinkage of crystalline domains from the particle shell toward the core, illustrating a gradual crystalline-to-amorphous transition. It is important to note that in many previous studies, the amorphous layer has often been conflated with the SEI, leading to significant confusion in interpreting the underlying structural changes.

To clarify these discrepancies, we summarize the most influential factors contributing to the variation in reported amorphization behavior in Table 2. Among them, crystal size is a particularly critical factor, as smaller particle sizes favor amorphization and pseudocapacitive behavior. Additionally, electrolyte composition and cut-off voltage are shown to play crucial roles in determining whether amorphization occurs. Specifically, when a diglyme-based electrolyte and a low cut-off voltage are used, amorphization is consistently observed. Moreover, the addition of fluoroethylene carbonate (FEC) often results in an abnormally high initial discharge capacity, which may further complicate the interpretation of amorphization behavior and must be considered carefully in future mechanistic studies.

It is worth noting that TiO_2-based negative electrodes typically exhibit low ICE during the first cycle, as reported in numerous studies [22, 36, 51, 59]. This behavior cannot be fully attributed to the formation of SEI alone. Since such high voltages are insufficient to cause significant electrolyte decomposition. Given the intrinsically poor electronic and ionic conductivities of TiO_2,

Table 2 Factors influencing the amorphization process

Year	Phase	IDC[a] (mAh·g^{-1})	ICE[b] (%)	Particle size (nm)	Crystal size (nm)	Electrolyte[c]	Amorphization	Ref.
2014	TiO_2(A)	740(0–3 V)	26	—	~ 10	1 M $NaClO_4$ in PC:FEC (98:2 *v*/*v*)	No	[54]
2014	TiO_2(A)	531(0.01–3 V)	—	—	< 8	1 M $NaClO_4$ in EC/DEC (1:1 *v*/*v*)	Yes	[60]
2015	TiO_2(A)	357(0.1–2 V)	44	30	—	1 M $NaClO_4$ in EC:PC[d] (1:1 *v*/*v*)	Yes	[49]
2015	TiO_2(A)	693(0.1–2 V)	36	< 10	—	0.5 M $NaPF_6$In PC:FEC (98:2 *v*/*v*)	No	[56]
2017	TiO_2(A)	129(0.1–2.5 V)	37	80	—	1 M $NaClO_4$ in PC	No	[100]
2017	TiO_2(A)	700(0.01–3 V)	31	100-350	8.1	1 M $NaClO_4$ in EC:PC (1:1 *v*/*v*)with 5 vol.% FEC	Yes	[51]
2018	TiO_2(A)	470(0.01–3 V)	56	—	< 25	1M $NaPF_6$ in Diglyme[e]	Yes	[36]
2019	TiO_2(A)	326(0.005–2.5 V) 423(0.005–2.5 V)	69 33	16	< 16	1 M $NaCF_3SO_3$ in Diglyme 1 M $NaCF_3SO_3$ in EC/DEC (1:1 *v*/*v*)	Yes Not clear	[59]
2022	TiO_2(A)	573(0.01–2.5 V)	44	—	10	1 M $NaClO_4$ in EC:DMC (1:1 *v*/*v*)with 5 vol.% FEC	Yes	[98]
2023	TiO_2(A)	294(0.01–3 V)	79	—	10	1 M $NaPF_6$ in Diglyme	Yes	[22]
2024	TiO_2(A)	650(0.01–3 V)	57	—	12	1 M $NaPF_6$in EC:DECwith 5 vol.% FEC	No	[58]

[a] Initial discharge capacity, [b] Initial coulombic efficiency, [c] PC: propylene carbonate, [d] EC: ethylene carbonate, DEC: diethyl carbonate, DMC: dimethyl carbonate, FEC: fluoroethylene carbonate, [e] Diglyme (DEGDME): diethylene glycol dimethyl ether.

ion insertion into the lattice is energetically demanding and requires a higher electrochemical driving force. As a result, significant lattice distortion may occur, and a portion of the inserted ions may become irreversibly trapped within the structure, even after subsequent charging (extraction). Interestingly, several studies have reported that cycled TiO_2 with an amorphous structure exhibits enhanced capacitive behavior. The amorphous matrix accommodates ion insertion with minimal volume expansion, consistent with a pseudocapacitive storage mechanism, thereby contributing to excellent rate capability and high specific capacity. Moreover, the typically high specific surface area, abundant surface defects, and porous architecture of the amorphous phase offer numerous active sites for ion adsorption and retention. Additionally, its inherently low electronic conductivity may help suppress charge leakage, thus enhancing both double-layer capacitance and surface pseudocapacitive.

Based on these observations, the amorphization in TiO_2 electrodes can be tentatively described as follows: during discharge, ion insertion induces progressive lattice distortion, ultimately leading to the collapse of the crystalline framework and the formation of an amorphous phase (e.g., sodium titanate). This amorphous structure subsequently enables ion storage through interfacial or pseudocapacitive mechanisms, which are particularly dominant in nanostructured TiO_2 materials [101].

Notably, pseudocapacitive contributions arising from faradaic processes, such as surface redox reactions and ion insertion at undercoordinated atomic sites, are significantly enhanced in amorphous structures, leading to simultaneous improvements in both electrochemical double-layer capacitance and pseudo-capacitance [102]. Based on these insights, it can be concluded that surface disorder is beneficial for promoting faradaic charge storage processes, thereby enhancing overall pseudocapacitive performance. This enhancement can be attributed to several characteristics intrinsic to the amorphous structures, which facilitates sodium ion adsorption and transport . Similar trends have been observed in LIBs, where surface-amorphized structures show stronger capacitive behavior [99, 103–105].

Since as early as 2000, nanostructured materials have attracted growing attention in electrochemical energy storage [67, 106], owing to their ability to enhance ion transport and pseudocapacitive behavior through crystal size reduction. As the crystal size approaches the Debye length, the interfacial region becomes dominant in charge storage, and the mechanism transitions from bulk diffusion-limited to surface-controlled behavior. In such regimes, the distinction between purely capacitive and battery-type mechanisms becomes increasingly ambiguous [83]. In electric double-layer capacitors (EDLCs), charge storage is based on the reversible physical adsorption of electrolyte ions onto the electrochemically stable surface of the electrode, without involving chemical changes in the electrode material (Fig. 7(a)) [107]. This mechanism allows for ultrafast charge/discharge but typically results in low energy density. Representative CV and GCD profiles of EDLCs are show in Figs. 7(b) and 7(c). In contrast, battery-like faradaic reactions involve ion insertion or extraction into/from the bulk electrode lattice (Fig. 7(d)), which enables high energy density but is limited by ion diffusion, resulting in slower kinetics and typically characterized by pronounced redox peaks and extended voltage plateaus (Figs. 7(e) and 7(f)) [73, 82].

Pseudocapacitive behavior bridges these two mechanisms by combining the high energy density of faradaic reactions with the fast kinetics of capacitive storage [108]. It involves rapid and reversible surface or near-surface redox reactions, with charge storage occurring primarily within the outermost regions of the electrode (Fig. 7(g)). As illustrated in Fig. 7(h), broad CV peaks in pseudocapacitive materials arise from the superposition of successive redox processes. Materials such as V-, Mn-, Nb-, and Ru-based compounds typically exhibit stepwise electron transfer over a wide potential window, resulting in continuous and broad redox activity. Additionally, the coexistence of surface adsorption and insertion-based pseudocapacitance leads to mixed behavior in GCD curves (Fig. 7(i)). The electronic structure and energy level distribution, particularly in nanomaterials, play a critical role in enabling successive electron transitions, which manifest as broadened or multi-peaked CV and sloped GCD curves [73, 83, 107, 109].

In summary, the inherently poor electronic and ionic conductivities of TiO_2 make ion insertion energetically demanding, requiring a higher electrochemical driving force to facilitate ion insertion into the TiO_2 lattice [62, 63, 99, 110]. This often leads to substantial lattice distortion and eventual amorphization of the structure. Interestingly, amorphous TiO_2 has emerged as a promising material for electrochemical energy storage material due to its rapid electrochemical response, excellent cycling stability, and high specific surface area. These advantages arise from the fact that ion transport is no longer limited by bulk-phase diffusion, thereby enabling superior rate capability [105, 109, 111–113]. A relevant precedent is the work by Dunn et al. [108], who demonstrated the pseudocapacitive lithium-ion insertion behavior of orthorhombic Nb_2O_5 electrodes in LIBs, particularly in mesoporous and nanocrystalline forms. However, this study overlooked the *in-situ* electrochemically induced phase transformation in Nb_2O_5 later reported by H. Xiong et al. [61], which provided key insights into the structural dynamics during cycling. Ion insertion into disordered oxide frameworks such as amorphous TiO_2 is inherently complex due to the lack of long-range order and may involve local structural rearrangements or reorganization during insertion. Furthermore, the differences in ion storage mechanisms between amorphous and crystalline TiO_2 warrant careful reconsideration. A fundamental trade-off exists between ion and electron transport in these two structural regimes, a topic that will be discussed in detail.

2.4 Multistep phase transition mechanism

Historically, transition metal oxides were not considered viable electrode materials for rechargeable ion batteries, primarily because their crystalline structures typically lack vacant sites for insertion and deinsertion. However, in the early 21st century, J.-M. Tarascon's group reported a novel lithium uptake/removal mechanism based on vanadates (MVO_4, M = In, Cr, Fe, Al, Y) and various transition-metal oxides (M_xO_y, M = Fe, Co, Ni, Cu, etc.) [114–116]. This mechanism, known as the conversion reaction, differs fundamentally from the conventional insertion/deinsertion and alloying processes and sparked considerable interest in the field of electrochemical energy storage. This conversion reaction involves drastic, ion-driven structural and textural transformations during the first cycle, leading to a second charge–discharge profile that deviates significantly from the first [67, 117]. Notably, these transformations are often accompanied by the development of pseudo-amorphous characteristics that, once formed during the first discharge, tend to be retained during the subsequent charging process [114–116].

Similar phase transition phenomena have also been observed in other transition metal oxide systems, such as vanadium and

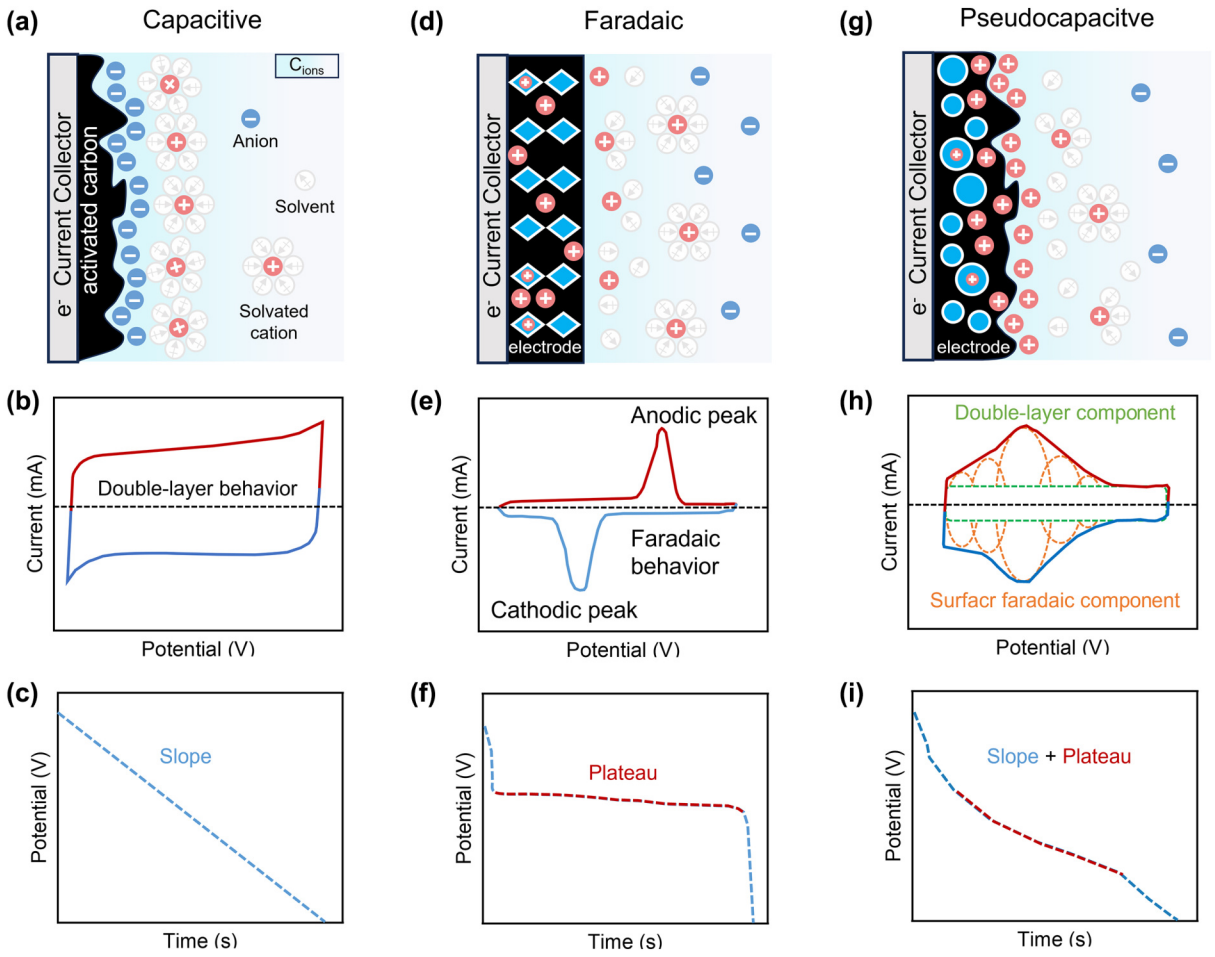

Figure 7 Schematic illustration of different types of charge storage mechanisms. (a) A typical capacitive behavior in EDLCs, where charge storage relies on the reversible adsorption of electrolyte ions onto active materials. (b) CV curve of EDLCs exhibiting a nearly rectangular shape. (c) GCD curve of EDLCs showing a linear slope. (d) Battery-type mechanisms involve faradaic redox reactions, where ions are inserted into or extracted from the electrode lattice. (e) A typical battery CV curve showing distinct redox peaks associated with charge-transfer reactions. Reproduced with permission from Ref. [111], © 2014 American Association for the Advancement of Science. (f) A typical battery GCD curve displaying voltage plateaus corresponding to two-phase coexistence. (g) Pseudocapacitive mechanisms involve fast surface or near-surface redox reactions and ion adsorption. (h) A typical pseudocapacitive CV curve showing multiple successive surface redox reactions (dashed line), contributing to pseudocapacitive charge storage. (i) A typical GCD curve of pseudocapacitive materials combining features of both slope and plateau, associated with surface adsorption and two-phase coexistence, respectively.

manganese oxides. For instance, in the manganese oxide system, a tunnel-structured todorokite, typically found in nature but difficult to synthesize under ambient laboratory conditions, can be electrochemically generated from a layered MnO_2 precursor via repeated cycling [118]. Likewise, disordered rock-salt (DRX) $Li_{3+x}V_2O_5$ has been obtained by electrochemically lithiating V_2O_5 to 1.5 V [119]. These findings collectively point to a rich yet underexplored research domain, with significant potential to advance the understanding of electrochemically induced phase transitions in TiO_2 and other metal oxide electrode materials.

2.4.1 *Conversion reduction mechanism*

In 1997, considerable research efforts were directed toward exploring new metal oxide-based negative electrode systems for LIBs. Among the most influential was the work by Idota et al. [72], who reported an amorphous tin-based composite oxide containing Sn(II)–O as the active center for lithium insertion, along with other glass-forming elements that constituted the oxide network. They also filed approximately 200 patent applications related to the so-called "Fuji cell", which detailed the synthesis and electrochemical behavior of hundreds of tin-based and other group IV element oxide composite glasses [120]. In these systems, the negative electrode comprised a tin-based composite oxide (TCO), rather than conventional carbon. The authors claimed that lithium storage occurred via a reversible insertion mechanism, wherein lithium maintained its ionic character throughout the charge–discharge process and did not result in the formation of metallic tin (Sn^0).

However, the reported lithium-to-tin ratio, approximately 4 to 7 Li atoms per Sn atom, was significantly higher than typical insertion systems. This discrepancy prompted further investigation by J.R. Dahn and L.F. Nazar's group [121, 122], who focused on understanding the fundamental storage mechanisms in these materials, particularly in parent compounds such as SnO and SnO_2 and the glassy $SnSiO_3$. Their findings revealed that the irreversible capacity was roughly proportional to the oxygen content (as Sn-O bonds) in the starting material, highlighting the crucial role of oxygen participation in the electrochemical reactions. In contrast, lithium alloying with pure metallic tin (i.e., without Sn–O bonds) was found to be highly irreversible. This difference is attributed to a conversion reduction in which the reduction of tin oxides results in the formation of an amorphous Li_2O matrix that serves to maintain mechanical cohesion between electrode particles. Consequently, tin oxides and their composites

generally exhibit more stable cycling performance compared to metallic tin.

A similar phenomenon has also been observed in other group IV post-transition metal oxides, such as PbO_2, which follows a comparable alloying reaction mechanism involving the reduction of the metal oxide and the reversible formation/decomposition of lithium-metal alloys [123]. These findings have led to the proposal of a more universal reaction scheme. During the first discharge, lithium preferentially bonds with oxygen (originally bonded to the metal), breaking up the oxide matrix and generating dispersed metallic domains embedded within an amorphous Li_2O framework. Upon further lithiation, these metallic regions alloy with lithium up to the theoretical limit of $Li_{4.4}M$. The reverse (delithiation) process occurs during charging, though only a small fraction of lithium can be reversibly extracted from the Li_2O matrix. This generalized reaction pathway is illustrated in Fig. 8.

However, for 3d transition metals, alloying reactions with lithium are not thermodynamically feasible. As a result, the alloying mechanism has historically been confined to certain post-transition metal elements, such as Al、Ga、In、Sn、Pb、Bi、Ge. This limitation remained until the early 2000s, when J.-M. Tarascon's group reported that vanadate-based systems (MVO_4, M = In, Cr, Fe, Al, Y) and other 3d transition metal oxides (M_xO_y, M = Fe, Co, Ni, Cu, etc.) [67, 114–116] also exhibited large irreversible capacity losses during the first discharge. These losses were attributed to the complete reduction of the metal oxides and the concurrent formation of a Li_2O matrix, followed by the amorphization of the resulting metal particles, a process now widely recognized as the conversion mechanism.

This mechanism differs fundamentally from traditional insertion/deinsertion or alloying processes. Rather than relying on interstitial ion diffusion or alloy formation, the conversion reaction involves ion-driven structural and textural transformations of transition metal oxides. These transformations result in the full reduction of the oxide and the formation of highly dispersed, nanosized metallic particles embedded in a Li_2O matrix. These metallic nanoparticles then participate in the reversible formation and decomposition of Li_2O, enabling repeated electrochemical cycling.

The conversion reaction can be generalized as a displacive redox process, exemplified by the following reaction scheme:

$$M_aX_b + (b \cdot n)Li \leftrightarrow aM + bLi_nX \quad (1)$$

where M = metal, X = anion, and n = formal oxidation state of X. The key to reversibility in this mechanism lies in the formation and subsequent redispersion of metal nanoparticles; the extent of nanoparticle aggregation significantly impacts long-term cycling performance. Moreover, the conversion process is typically accompanied by the formation of a SEI layer, similar to that formed on carbonaceous negative electrodes. The generated metallic particles often display pseudo-amorphous characteristics due to their nanostructured and disordered nature [124, 125]. However, it is important to note that direct structural evidence for the formation of metallic particles during conversion reactions remains limited.

Although only a few studies have suggested that TiO_2 may undergo a conversion-like mechanism involving the formation of metallic Ti^0 [19, 49, 126, 127], such a pathway cannot be ruled out. For example, Passerini et al. [49], reported a gradual decrease and eventual disappearance of XRD reflections corresponding to TiO_2(A) during sodiation, which did not reappear upon subsequent desodiation. Coupled with the significant irreversible capacity loss observed during the first cycle, these findings led the authors to propose that the reaction may proceed via a conversion-like mechanism. Specifically, they hypothesized that TiO_2(A) first transforms into an intermediate sodium titanate phase, which then undergoes disproportionation into another sodium titanate species and is partially reduced to metallic titanium (Ti^0), sodium superoxide (NaO_2), and molecular oxygen (O_2), following the reaction pathway:

$$TiO_2 + Na^+ \rightarrow Ti + Na_xTiO_2 + NaO_2 + O_2 \quad (2)$$

Although the formation of metallic titanium and NaO_2 is irreversible, the newly generated amorphous sodium titanate phase can reversibly intercalate and deintercalate approximately 0.41 Na^+ per TiO_2 unit, thereby enabling stable cycling following the initial conversion reaction. However, several critical considerations must be addressed:

(a) While some studies report that TiO_2 is reduced to metallic Ti^0 upon deep discharge to 0.01 V, the primary evidence originates from *ex-situ* XPS analysis, which shows characteristic peaks assigned to metallic Ti^0 (Ti $2p_{3/2}$ at 453.7 eV and Ti $2p_{1/2}$ at 459.8 eV) [49, 126]. However, other investigations have reported only a reduction of Ti^{4+} to Ti^{3+} at low potentials (down to 0.01 V). Upon recharging to 3 V, peaks observed at binding energies of 456.4 and 462.5 eV were attributed to metallic Ti^0 [19]. However, these binding energies deviate from those typically associated with metallic titanium, casting doubt on the actual presence of metallic Ti^0.

From a thermodynamic perspective, the complete reduction of

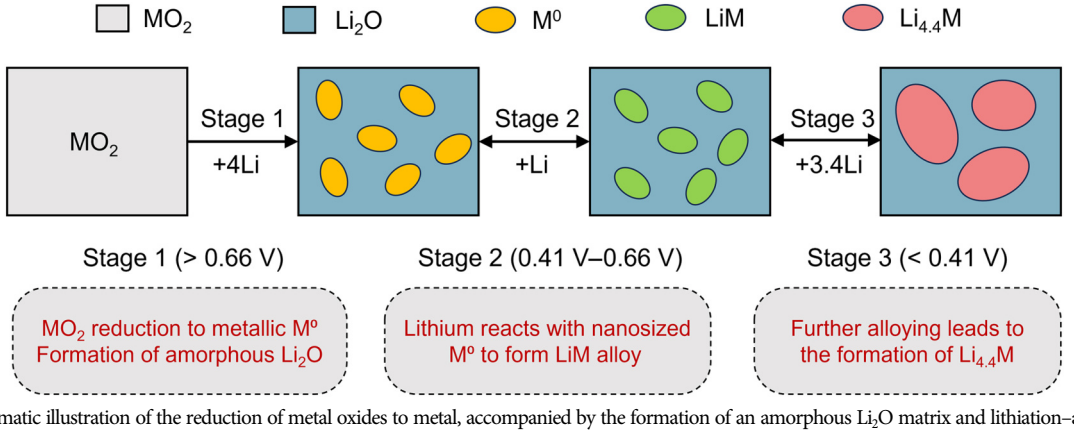

Figure 8 Schematic illustration of the reduction of metal oxides to metal, accompanied by the formation of an amorphous Li_2O matrix and lithiation–alloying charge storage mechanisms.

Ti^{4+} to Ti^0 under typical sodiation conditions is improbable. Furthermore, *in-situ* XRD studies, recognized for their sensitivity to metallic phase formation during electrochemical reduction, fail to detect metallic diffraction peaks. Although the absence of such peaks has been attributed to the possible formation of Ti nanoparticles smaller than the X-ray coherence length [67], further investigation is warranted to clarify these discrepancies.

(b) Some reports propose that nanosized metal particles may catalyze the decomposition of Li_2O, as nanoscaling significantly alters the chemical and physical properties of the electrode material [67, 128]. However, from a thermodynamic standpoint, both Li_2O ($\Delta G°$ = +562.0 kJ·mol^{-1}) and Na_2O ($\Delta G°$ = +375.4 kJ·mol^{-1}) are highly stable compounds. The large positive Gibbs free energy changes associated with their decomposition reflect the strength of the Li–O and Na–O bonds, suggesting that decomposition is unlikely under standard battery operating conditions (e.g., discharging to 0.01 V or charging to 3 V). Although some researchers also argue that Li_2O may exist as nano crystallites smaller than the coherence length of X-rays, thus eluding detection via XRD studies, claims of metallic Ti^0 formation in systems involving Li_2O or Na_2O are more likely the result of misinterpreted spectroscopic signals [67, 121, 129].

While alloying and conversion reactions have been well-documented for certain post-transition metals [72, 121–123, 129–132], and even for some 3d transition metals [67, 114, 115, 133], the reaction mechanism governing TiO_2 cannot be fully explained by a single reversible insertion/extraction process, classical alloying behavior, or conventional conversion reactions. Recent studies suggest that the formation of a newly emerged rock-salt phase may better accounts for the observed electrochemical behavior via a structural reorganization process. Therefore, we advocate for a reevaluation of the TiO_2 reaction mechanism and propose that electrochemically driven phase transition pathways be explored more thoroughly. As many transition metal oxides exhibit similar behaviors, a deeper investigation into such mechanisms may offer valuable insights into the charge storage processes in other metal oxide-based electrodes. Therefore, the following sections will elaborate on the electrochemically driven phase transition storage mechanisms.

2.4.2 *Electrochemically driven phase transition mechanism*

Despite extensive investigations into the ion storage mechanisms of TiO_2, the reported results remain inconsistent. To address these discrepancies, a recently proposed multistep phase transition mechanism, comprising a crystalline-to-amorphous-to-rock-salt transformation, has emerged and warrants systematic discussion. Notably, a similar transformation has been reported in Nb_2O_5, a transition metal oxide that, like TiO_2, exhibits multiple polymorphs, sluggish Li^+ diffusion, and poor electronic conductivity. H. Xiong et al. [61] observed a crystalline-to-amorphous transformation in Nb_2O_5 during electrochemical cycling, followed by recrystallization into a nanostructured rock-salt Nb_2O_5 framework upon repeated lithiation.

The first evidence of an amorphous-to-crystalline transition in TiO_2 was also reported by H. Xiong et al. [77], and subsequent studies have supported a mechanism whereby intercalated ions induce a near-surface transformation of crystalline TiO_2 into an amorphous phase [134]. Upon extended cycling, this amorphous TiO_2 underwent an irreversible and spontaneous reorganization into a cubic rock-salt structure through electrochemically driven self-organization. This transformation is believed to generate ion-trapping sites during the initial cycle, contributing to the typically low ICE [22, 62, 63]. Moreover, it is widely recognized as a key factor in the emergence of pseudocapacitive behavior [58, 135, 136].

Very recently, an electrochemically induced multistep phase transition mechanism was proposed to reconcile inconsistencies in previous reports [62, 63]. By closely analyzing the evolution of the CV curves (Fig. 9(a)), a strongly irreversible cathodic peak during the first discharge (sodiation), accompanied by the gradual disappearance of diffraction peaks, was observed, both of which indicate a crystalline-to-amorphous transition. X-ray absorption spectroscopy (XAS) and *ex-situ* synchrotron-radiation pair distribution function analyses further confirmed this transformation, revealing an expansion of the Ti-O bond length from 1.54 to 1.59 Å, and the Ti-Ti bond from 2.51 to 2.76 Å after the first cycle. These changes reflect electrochemically induced distortion and expansion of the TiO_6 octahedral framework to accommodate Na^+ insertion.

Upon further cycling, the cathodic peak gradually shifts to higher voltages (as evident by comparing the 2nd and 10th cycles in Fig. 9(a), while broad redox peaks centered around 0.75 V become increasingly pronounced from the third cycle onward. Simultaneously, new XRD diffraction peaks at 36.8°, 43.3°, and 62.5° gradually emerge, indicating the formation of a rock-salt (RS-$NaTiO_2$) phase. Kinetic analysis comparing RS-$NaTiO_2$ (Fig. 9(b)) with the cycled amorphous TiO_2 electrode (Fig. 9(c)) reveals that differences in their electrochemical responses are primarily governed by the relative proportions of rock-salt nanograins and residual amorphous regions (see insets). While both phases can accommodate Na^+ ions, they exhibit distinct electrochemical profiles: the amorphous phase shows a "box-like" CV response, whereas RS-$NaTiO_2$ displays a "mirror-like" profile. This distinction is attributed to structural differences, specifically, the *in-situ* transformation from a crystalline TiO_2 lattice with well-ordered Ti-O octahedra generates more RS-$NaTiO_2$ nanograins than direct cycling of chemically synthesized amorphous TiO_2.

The crystalline-to-rock-salt phase transition was further validated by *ex-situ* HR-TEM and STEM. After a single cycle, the initially crystalline TiO_2(A) (Figs. 9(d) and 9(e)) becomes amorphous (Figs. 9(f) and 9(g)), consistent with most previously reported results [22, 36, 59]. Remarkably, after approximately 20 cycles, partial recrystallization occurs, resulting in the formation of ordered RS-$NaTiO_2$ nanograins (Figs. 9(h)–9(i)). These findings collectively support a multistep transformation pathway: initial Na^+ insertion disrupts the long-range order of crystalline TiO_2, forming an amorphous phase, which subsequently reorganizes into the RS-$NaTiO_2$ structure through continuous cycling. This transformation likely involves the gradual rearrangement of distorted TiO_6 octahedra and the progressive occupation of octahedral sites by Na^+ ions, forming [NaO_6] octahedra that define the rock-salt lattice. Notably, such behavior closely parallels that observed in Nb_2O_5, further supporting the universality of this mechanism among transition metal oxides [61].

In summary, during the discharging process, the crystalline regions of TiO_2 gradually undergoes amorphization from the particle shell toward the core, indicating that ion insertion distorts the lattice and partially induces a crystalline-to-amorphous transition. This transformation typically occurs during the initial discharge and is associated with pronounced irreversibility and voltage hysteresis. These effects may arise from irreversible ion trapping, lattice mechanical stress, thermodynamic and entropic factors, activation polarization, or nucleation barriers [61, 137]. Specifically, from a thermodynamic perspective, electrode

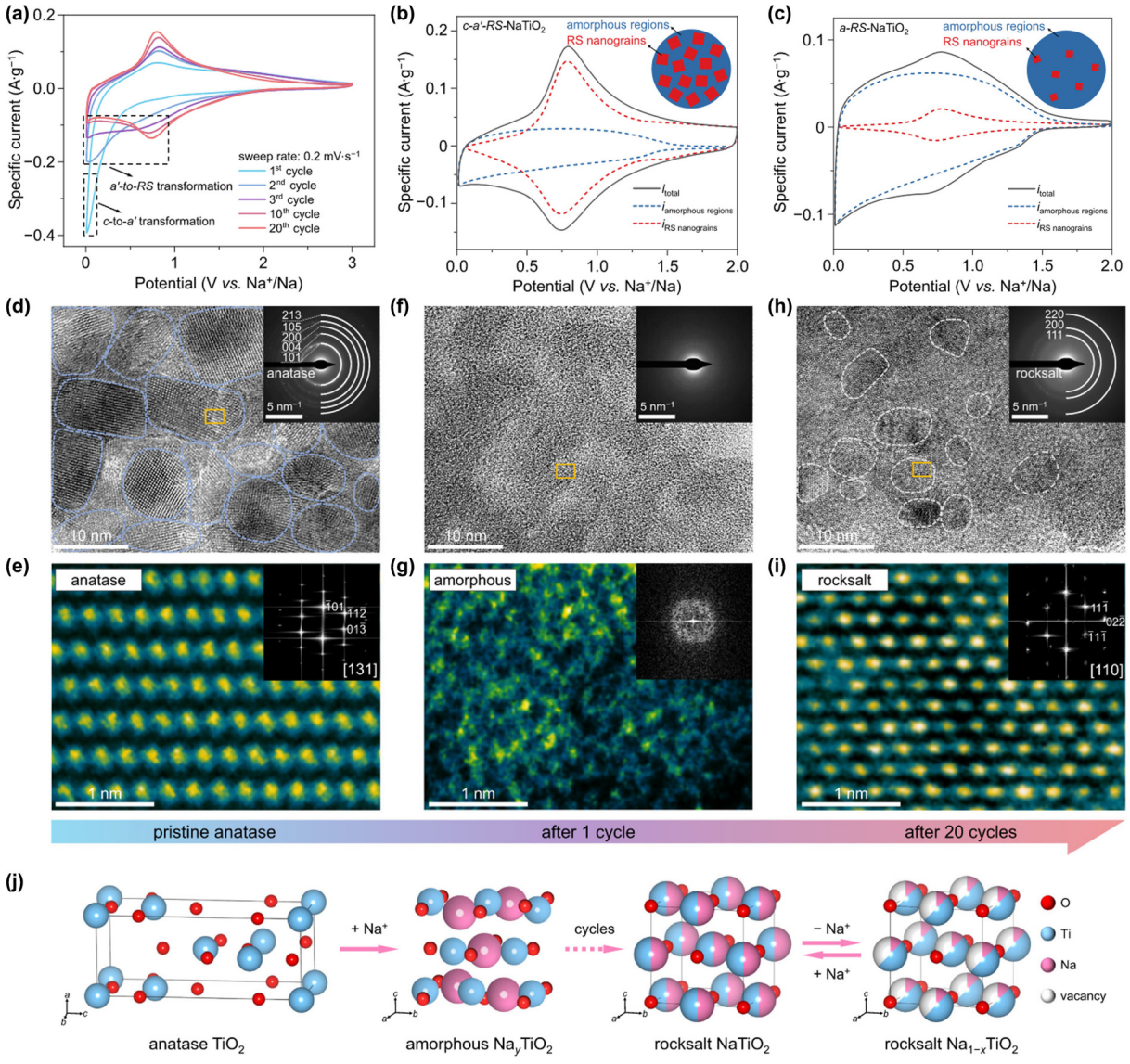

Figure 9 Electrochemically driven crystalline-to-amorphous-to-rock-salt phase transformation. (a) CV curves of the TiO_2(A) electrode for initial 20 cycles (scan rate: 0.2 mV·s^{-1}). (b) Deconvolution of the CV curves for the cycled TiO_2 with more RS-$NaTiO_2$ nanodomains and (c) with less RS-$NaTiO_2$ nanodomains at 0.2 mV·s^{-1}. The total response current (i_{total}) consists of contributions from both the RS phase nanograins (i_{RS}) and the residual amorphous regions (i_{amor}). (d)-(i) HRTEM and atomic-resolution HAADF-STEM images of (d, e) pristine a-TiO_2, (f, g) after 1 cycle, and (h, i) after 20 cycles, respectively. The insets are the corresponding SAED patterns and the FFT patterns images. (j) Schematic illustration of the multistep phase transition mechanism, highlighting the electrochemically driven crystalline-to-amorphous-to-rock-salt phase transformation, followed by a solid-solution reaction of the *in-situ* formed RS-$NaTiO_2$ nanograins during Na^+ cycling. Reproduced with permission from Ref. [63], © 2025 Tang, D. F. et al.

materials inherently tend to evolve from metastable or non-equilibrium phases toward more stable configurations as structural and compositional changes accumulate during cycling. From a kinetic standpoint, the onset and progression of phase transitions are governed by factors such as charge transfer resistance, ion diffusion limitations, crystal structure and defects. In some studies, the absence of bulk structural transformation has been attributed to kinetic constraints or electrochemical conditions that suppress the amorphization process, particularly when the crystallite size is too large to undergo complete transformation. Moreover, extended cycling may induce partial nucleation within amorphous regions, leading to the formation of rock-salt Li/$NaTiO_2$ nanograins. These nanograins subsequently contribute additional ion storage through interfacial or insertion pseudocapacitive mechanisms. Previous studies have shown that when the ion concentration exceeds a critical threshold, atomic rearrangement is thermodynamically favored to minimize the system's free energy, thus triggering a phase transition into the more stable rock-salt structure [61, 63]. Importantly, RS-Li/$NaTiO_2$ has been shown to be both thermally and air-stable, making it a thermodynamically preferred phase into which the amorphous TiO_2 structure tends to spontaneously evolve during prolonged electrochemical cycling [61–63]. Furthermore, the stabilization of Li/$NaTiO_2$ nanoscale grains plays a crucial role in mitigating mechanical degradation by relieving electrochemical stress, maintaining structural coherence, and facilitating reversible phase transitions, all of which collectively contribute to superior long-term cycling stability in TiO_2-based electrodes.

Interestingly, electrochemically induced phase transitions have also been widely reported in other transition other metal oxides [49, 67, 106]. For instance, in Fe_2O_3 and Fe_3O_4, a transition from a hexagonal close-packed to a cubic close-packed oxygen sublattice

has been observed [101, 138]. In the spinel Fe_3O_4 structure, Li^+ insertion involves cooperative Fe-ion migration from tetrahedral to octahedral sites, ultimately leading to the formation of a rock-salt-type phase, a process that is also strongly influenced by crystal size. Similarly, MoO_3 undergoes an irreversible structural phase transition upon lithium insertion [139]. Moreover, disordered rock-salt structures have also been structure reported in other transition metal oxides, including niobium oxide electrodes [61], vanadium oxides [119], manganese oxides [118], and DRX-type layered positive electrode materials [140–142].

These observations challenge the conventional perception that irreversible phase evolution is inherently detrimental to battery performance. On the contrary, the *in-situ* formation of new disordered phases, often with superior Li^+ or Na^+ storage capability, offers a novel design strategy for transition metal oxide-based negative electrodes. However, the investigation of such dynamic structural transformations remains challenging due to the limited spatial and temporal resolution of conventional characterization techniques. Therefore, the application of advanced *in-situ* or operando analytical methods is essential to fully unravel the underlying mechanisms governing these complex phase transition processes in TiO_2 and other nanostructured transition metal oxides.

3 Effects on ion storage mechanisms in TiO_2

As previously discussed, TiO_2 electrode materials inherently undergo crystalline-to-amorphous transitions, followed by possible recrystallization. Their structure and electrochemical properties are influenced by a range of factors, including crystal size [143], defect density [144–150], and morphology [151, 152]. In addition, electrochemical parameters and environmental conditions, such as temperature, also play a significant role in shaping the electrochemical behavior of TiO_2 [35, 59, 63]. Despite the importance of these factors, a comprehensive understanding of how they affect ion transport and storage mechanism in TiO_2, particularly with respect to structural evolution, phase transitions, and ionic/electronic conductivities, remains incomplete. Therefore, in the following section, we focus on the influence of extrinsic physicochemical factors on the electrochemical performance of TiO_2, based on the most recent advances in understanding its ion storage mechanisms.

3.1 Crystal size

Due to the inherently poor electronic and ionic conductivities of TiO_2, nanostructuring has emerged as an effective strategy to enhance electrochemical kinetics by shortening ion diffusion pathways. Notably, our review reveals that many of the inconsistencies reported in the literature regarding the ion storage mechanism of TiO_2 are closely related to variations in crystal size. This issue remains a subject of active debate, particularly for TiO_2 nanocrystals just a few nanometres in size, where crystal size exerts a pronounced influence on ion storage behavior.

In general, numerous studies have demonstrated that nanostructuring can effectively address the limitations of poor ionic conductivity by reducing ion diffusion lengths, thereby improving electrochemical performance [67, 68, 153–156]. This enhancement is primarily attributed to size-dependent effects on both kinetics and thermodynamic properties, as materials exhibit significant changes in behavior at the nanoscale due to so-called 'nano effects'. For instance, when the size of gold particles drops below 10 nm, the melting point can dramatically drop, from the bulk value of 1064.18 °C to as low as 326.85 °C when particle size is reduced below 2 nm [128]. This phenomenon results from a higher surface-to-volume ratio (i.e., a greater fraction of atoms residing on the surface), elevated surface energy (due to reduced atomic coordination and unsatisfied surface bonds), and the Gibbs–Thomson effect, which describes the increased chemical potential of atoms in smaller particles compared to their bulk counterparts. However, reducing dimensionality to the nanoscale also introduces several challenges for electrode materials. In particular, the reduction of crystal size to the nanometre regime can create substantial interparticle voids, resulting in a low tap density of the electrode. Besides, nanostructured TiO_2 particles have a poor tap density to produce a low electrode compact density, resulting in thicker electrodes at the same areal capacity. Furthermore, their poor packing ability makes the electrode higher porosity and more interfaces. These can increase the ion transport distance and electron transfer path, and result in high contact resistance between active materials and conductive additives, thus decreasing the rate capability to some extent. Although the high surface area of nanomaterials can enhance electrochemical activity, it also increases the tendency for particle aggregation and accelerates surface-related side reactions or oxidation, ultimately contributing to the degradation of the active material. The enlarged surface area of nanostructured TiO_2 also increases the electrolyte decomposition rate during initial cycles, exacerbating irreversible capacity loss and further reducing the ICE.

Taken together, these considerations underscore the complex balance between the advantages and limitations of nanoscale engineering. Therefore, we summarize the intrinsic thermodynamic and kinetic properties, associated drawbacks, and how nanosizing TiO_2 has enabled the discovery of new phase transition mechanisms in Fig. 10. In summary, while nanostructuring TiO_2 significantly improves rate performance and ion transport, its inherently low ICE and tap density remain a practical bottleneck for high-energy applications. Through electrolyte optimization, surface modification, hierarchical particle design, conductive matrix integration, and electrode-level optimization [51, 58, 157–159], it is possible to balance high electrochemical reactivity with desirable volumetric energy density and ICE—making nanostructured TiO_2 more viable for large-scale sodium- and lithium-ion batteries.

Since the early 2000s, numerous studies have demonstrated that the electrochemical performance of M_xO_y-based electrodes (where M= Co, Ni, Cu, Fe, Nb or Ti) is strongly influenced by crystal size [67, 74, 75, 117, 160, 161]. More recent investigations of DRX electrodes [119, 162, 163], further support the notion that the thermodynamic stability of nanocrystalline materials is inherently size-dependent [164]. Similarly, downsizing TiO_2 from the microscale to the nanoscale not only enhances reaction kinetics but also induces thermodynamic shifts. As the particle size of decreases, a greater proportion of atoms are located at or near the surface, thereby increasing surface-related electrochemical reactivity [22]. This enhanced surface reactivity plays an increasingly important role in driving phase transitions toward more thermodynamically favourable structures, particularly when ion concentration reaches a critical threshold and triggers atomic rearrangement to minimize the system's free energy.

In 2005, J.-M. Tarascon et al. [68] were the first to report that reducing the crystal size of TiO_2(A) to ~10 nm significantly enhanced its electrochemical performance. As shown in Fig. 11(a), TiO_2 samples with different crystal sizes (76.1, 11.0, and 6.3 nm)

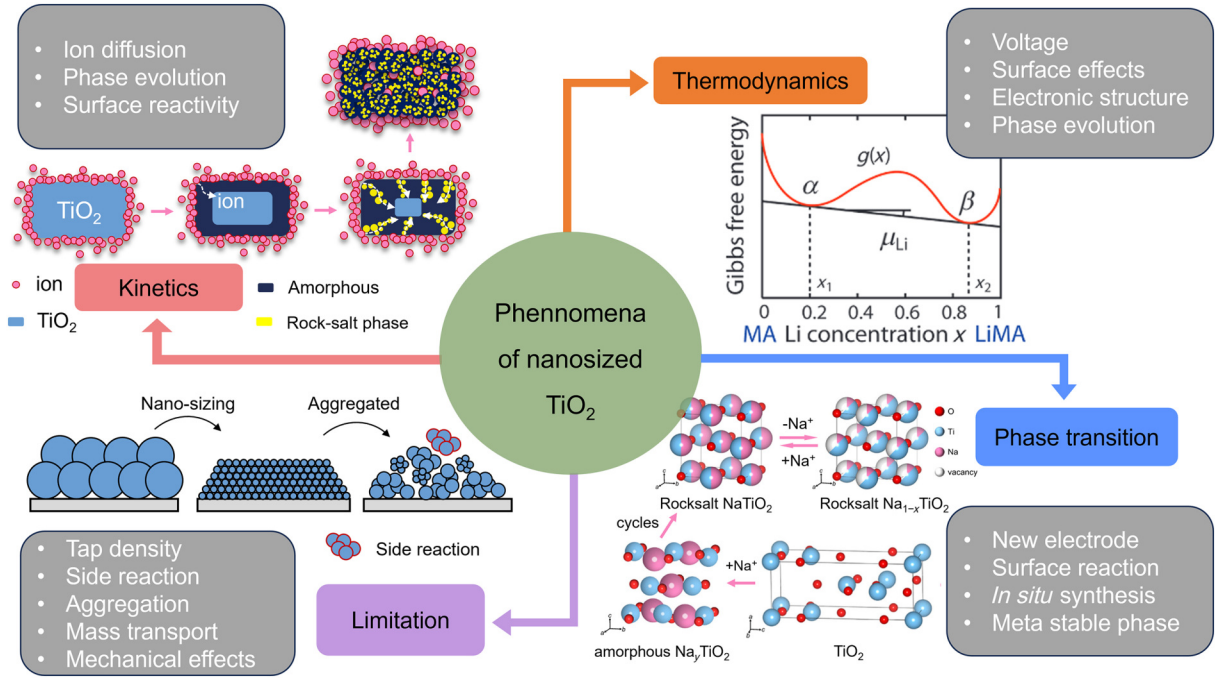

Figure 10 Nanosizing phenomena of TiO_2 electrode materials. Reproduced with permission from Ref. [63], © 2025 Tang, D. F. et al.; from Ref. [84], © 2012 American Chemical Society, and from Ref. [156], © 2019 American Chemical Society.

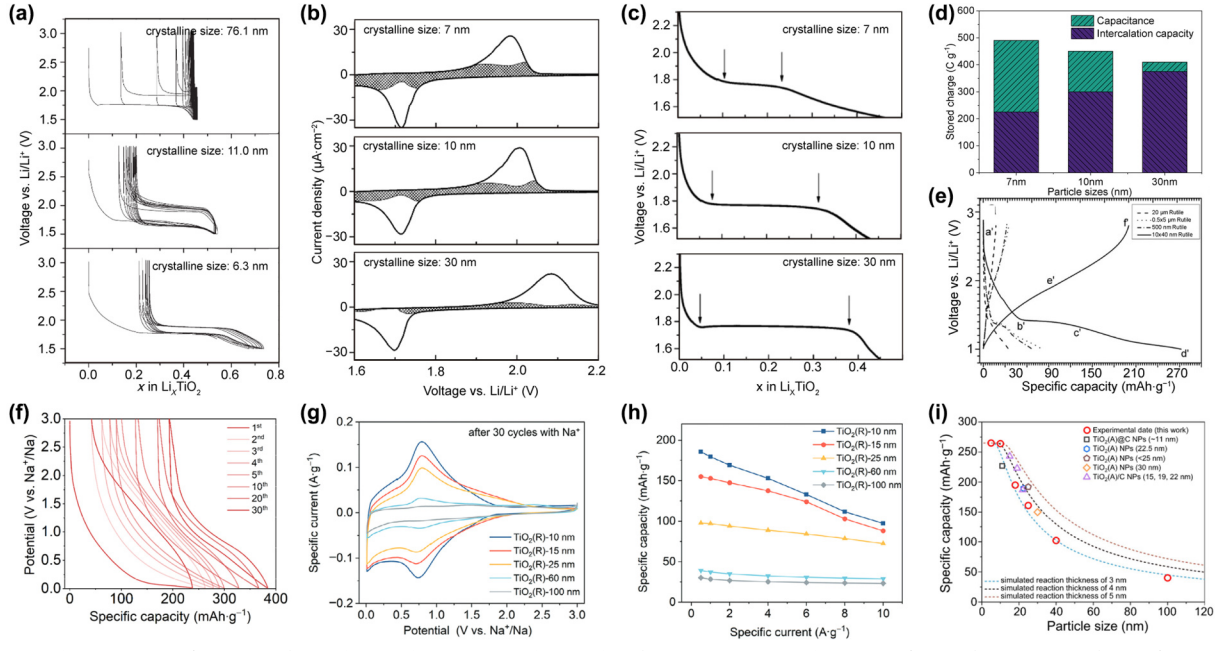

Figure 11 (a) GCD curves of commercial TiO_2 (76.1 nm), TiO_2 400 °C (11.0 nm) and TiO_2 250 °C (6.3 nm) at a rate of 0.05 C between 1.5 and 2.5 V for Li^+ storage. Reproduced with permission from Ref. [68], © 2005 The Royal Society of Chemistry. (b) CV (0.5 $mV \cdot s^{-1}$) curves of the three TiO_2 for Li^+ storage. The total current (solid line) is obtained experimentally. The capacitive current curves (shaded regions) are obtained by calculating. (c) GCD curves of TiO_2 at 1 C. (d) The total charge is separated into lithium insertion and capacitive contributions. (b–d) Reproduced with permission from Ref. [143], © 2007 American Chemical Society. (e) GCD curves of TiO_2 with different particle sizes and shapes cycled at a rate of 0.05 C between 1.0 and 2.8 V. Reproduced with permission from Ref. [69], © 2006 WILEY-VCH Verlag GmbH & Co. KGaA, Weinheim. (f) GCD profiles of the TiO_2(R)-10 nm electrode for Na^+ storage during initial 30 cycles. (g) CV (0.2 $mV \cdot s^{-1}$) curves for Na^+ storage at the 30th cycle. (h) Rate capability of TiO_2 with different particle sizes for Na^+ storage. (f-h) Reproduced with permission from Ref. [62], © 2025 Wiley-VCH GmbH. (i) The relationship between particle size and specific capacity can be attributed to the thickness of the surface reaction layer. Reproduced with permission from Ref. [22], © 2023 Wei, Q. L. et al.

exhibit a well-defined plateau at 1.75 V vs. Li^+/Li^0 during the first discharge, with the solid-solution domain broadening as particle sizes decreases. These results highlight the crucial role of particle size in influencing electrochemical behavior. Moreover, smaller TiO_2 particles also demonstrate superior capacity retention (Table 3), which may be attributed to faster ion transport, improved surface kinetics, and greater structural flexibility. Such characteristics facilitate accommodation of lattice strain during ion insertion in nanoscale crystallites, whereas in bulk materials, ion insertion is largely confined to the surface, often resulting in internal stress and structural degradation.

Building on these findings, B. Dunn et al. further investigated

the size effect by analyzing galvanostatic discharge behavior and conducting detailed cyclic voltammetry (CV) of TiO_2 with different nanocrystal sizes (Figs. 11(b)–11(d)). Their CV curves reveal narrower peak separations for smaller TiO_2 particles, indicating more favorable kinetics. However, surprisingly Li^+ insertion and extraction in these smaller TiO_2 particles exhibited lower diffusion coefficients: 1.3×10^{-16} $cm^2 \cdot s^{-1}$ for 10 nm TiO_2 and 6.2×10^{-17} $cm^2 \cdot s^{-1}$ for 7 nm TiO_2. In contrast, the diffusion coefficients of Li^+ in single-crystalline and bulk thin-film TiO_2 are approximately 3.0×10^{-13} and 3.8×10^{-15} $cm^2 \cdot s^{-1}$, respectively [99, 165]. This discrepancy arises from the different dominant charge storage processes. While charge transfer at the electrode–electrolyte interface becomes more efficient with decreasing particle size, bulk diffusion becomes increasingly constrained due to size-induced structural limitations. In this context, surface or grain boundary diffusion dominates over bulk diffusion.

In short, although insertion-based ion diffusion becomes less favorable as crystal size decreases, the enhanced surface-controlled capacitive contributions of smaller TiO_2 particles more than compensate for this limitation, ultimately resulting in improved electrochemical performance. Additionally, a reduction in particle size leads to a narrower voltage plateau region (Fig. 11(c)), which is typically associated with a two-phase reaction involving coexistence of lithiated and unlithiated phases [84]. However, when particle size falls below a critical threshold, this phase separation is suppressed, and the system transitions to a single-phase solid-solution behavior dominated by surface adsorption [74]. Consequently, ion storage becomes increasingly pseudocapacitive in nature. More interestingly, although TiO_2(R) is the most thermodynamically stable and abundant polymorph under standard conditions, it has traditionally been considered inactive for lithium storage [166, 167]. Yet, when reduced to the nanometer scale, TiO_2(R) unexpectedly exhibits both high capacity and excellent rate performance (Fig. 11(e)) [69]. Thermodynamic analysis further indicates that surface free energy and surface stress, both highly size-dependent, play critical roles in governing phase stability [164]. These findings collectively reinforce the notion that TiO_2 electrochemical behavior is highly sensitive to crystal size.

More recently, Wei et al. [22, 62, 63] conducted a comprehensive investigation of the size-dependent ion storage behavior of TiO_2(A). As shown in Fig. 11(f), TiO_2 particles with ~10 nm size exhibit large irreversible GCD curves in the initial 30 cycles, along with a broadened solid-solution domain. Furthermore, smaller particles display stronger current responses at the same scan rate (Fig. 11(g)). Their CV profiles show broad, nearly mirror-symmetric peaks centered around 0.75 V vs. Na^+/Na, except for the largest (100 nm) particles. Both sodiation capacity (Q_{Na^+}) and rate capability are inversely proportional to the TiO_2 crystal size (Figs. 11(h)–11(i)), further confirming the critical role of crystal size in determining electrochemical performance. These trends are attributed to an irreversible crystalline-to-amorphous phase transformation that is size-dependent. When particle size exceeds a certain threshold, the transformation becomes incomplete, thereby degrading performance, offering a plausible explanation for the inconsistencies in earlier reports.

Notably, this phase transition process is strongly size-dependent. When the particle (crystal) size is relatively large, the structural transformation remains incomplete, with only a thin surface layer of crystalline TiO_2 undergoing the crystalline-to-amorphous-to-rock-salt phase transition during the initial electrochemical cycles (Fig. 12, left). In contrast, reducing the particle size to the nanoscale enables deeper ion penetration and facilitates a more complete structural transformation throughout the entire particle (Fig. 12, right).

Specifically, during the initial discharge, ion insertion induces lattice distortion in TiO_2, ultimately causing amorphization of a thin surface layer. With continued cycling, partial nucleation occurs within these amorphous regions, leading to the formation of highly ordered cubic rock-salt-phase Li/$NaTiO_2$ nanograins. However, in larger, micrometer-sized TiO_2 particles, sluggish ion diffusion limits the extent of this transition, confining structural evolution to only the surface region. In contrast, nanoscale TiO_2 particles can undergo near-complete amorphization and subsequent rock-salt-phase formation throughout the entire structure due to their short diffusion lengths.

As a result, nanosized TiO_2 typically exhibits superior ion storage performance, which can be attributed to the complete electrochemically induced crystalline-to-amorphous-to-rock-salt phase transition. The thermodynamically stable rock-salt-phase nanograins that form is capable of reversibly storing Li^+ and Na^+ through a solid solution mechanism characterized by minimal lattice volume change. Additionally, the abundant surface area of nanocrystals promotes surface adsorption, giving rise to pseudocapacitive-dominated behavior and significantly enhancing rate capability. This behavior is not exclusive to TiO_2; rather, it is widely observed in other nanostructured transition metal oxides, providing valuable insights for the rational design of advanced electrode materials [61, 67, 119, 137].

3.2 Defects

As previously mentioned, TiO_2 suffers from intrinsically low ionic and electronic conductivity. Therefore, strategies targeting improvements in both bulk and surface properties are essential to enhance its electrochemical performance [168]. Achieving high ionic conductivity requires not only a low activation energy but also a high concentration of mobile ion carriers, such as vacancies or interstitials.

It is well established that ion and electron transport in electrode materials is strongly influenced by the presence and nature of defects, as well as surface modifications. Various defect types exist, including point, line, planar, volumetric, and electronic defects. Among these, point defects play the most critical role in influencing ion transport within crystalline materials. The concept of point defects was first introduced by Frenkel in 1926 [169]. Typical point defects include Frenkel and Schottky defects: the former involves a paired vacancy and interstitial ion, while the latter consists of paired cation and anion vacancies (Fig. 13(a)). Once thermodynamically favorable point defects are formed, ionic diffusion proceeds via a series of thermally activated hops between these defect sites across a static energy landscape. The geometry and topology of the crystal structure dictate this landscape and the ion migration pathways, with the highest energy point along each path representing the activation energy barrier for ion diffusion (Fig. 13(b)). For example, cubic anion-packed frameworks offer relatively flat energy landscapes with low migration barriers, whereas hexagonal close-packed structures present significantly higher barriers [170].

Our current understanding of ionic diffusion in crystalline electrodes is based primarily on classical models, including the vacancy hopping mechanism, the interstitial hopping mechanism, and the interstitial-substitutional exchange (or "knock-off") mechanism (Fig. 13(c)) [171]. The vacancy hopping mechanism is

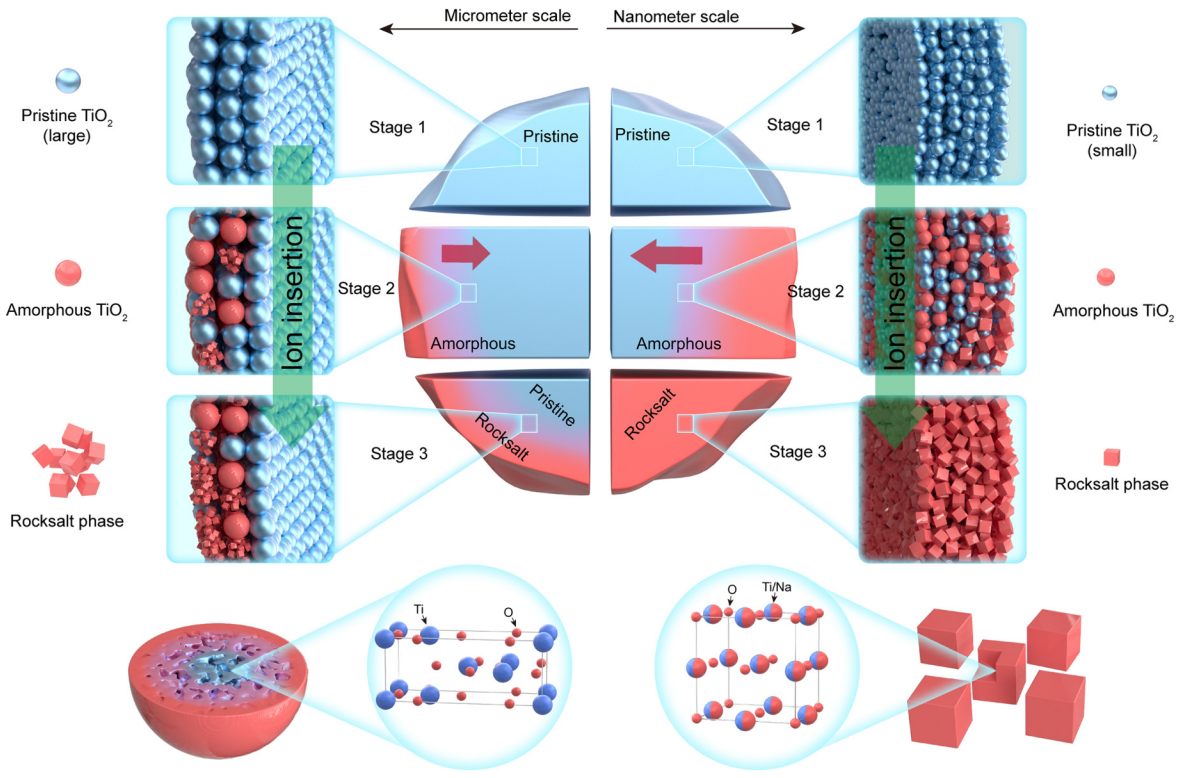

Figure 12 Size-dependent phase transition process.

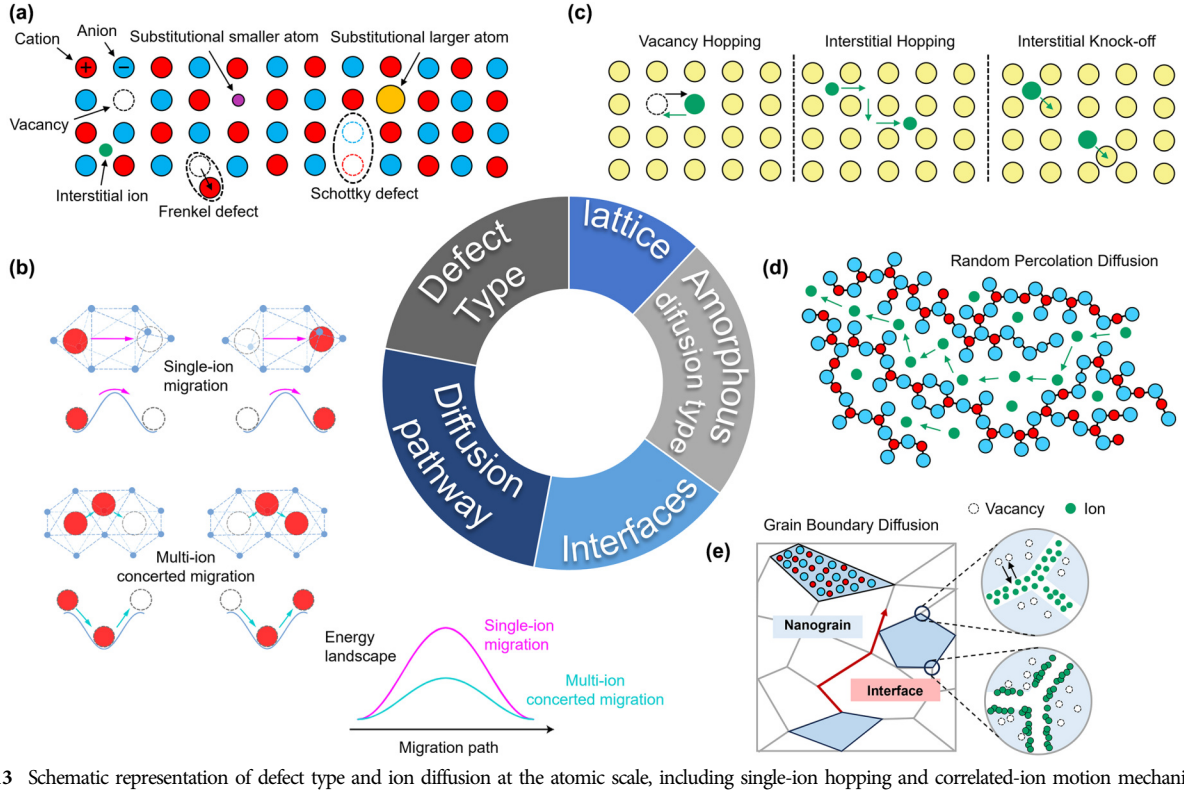

Figure 13 Schematic representation of defect type and ion diffusion at the atomic scale, including single-ion hopping and correlated-ion motion mechanisms. (a) Defect type, (b) diffusion pathway. Reproduced with permission from Ref. [172], © He, X. F. et al. 2017. (c) Migration mechanism in crystalline TiO_2. (d) Amorphous TiO_2 and (e) the nanograin boundaries transport at the microstructural scale.

driven by Schottky defects, where ions move through the lattice by successively occupying adjacent vacancies. In contrast, the interstitial hopping mechanism involves ion migration through available interstitial sites. In the knock-off mechanism, associated with Frenkel defects, interstitial ions displace lattice ions into neighboring sites, enabling ion mobility through a series of exchanges.

However, in structurally disordered systems, such as

amorphous or nanocrystalline materials, ion transport deviates significantly from these classical descriptions. In amorphous TiO_2 materials, which lack long-range order, ions migrate through random, non-periodic pathways influenced by the local structural and dynamic heterogeneity of the medium (Fig. 13(d)). These migration pathways involve complex interactions with surrounding atoms and structural features—including pores, voids, and chemical bonding environments, resulting in a distinct transport mechanism from that in crystalline phases.

Ion transport in nanocrystalline materials is also unique. These materials are composed of nanosized crystalline domains (1–100 nm) separated by grain boundaries, which are typically disordered and rich in defects such as vacancies and interstitials. These grain boundaries serve as fast ion-conducting pathways and are often accompanied by significant interfacial capacitance effects (Fig. 13(e)) [101]. Grain boundary diffusion plays a central role in governing ion transport in nanograined electrodes and contributes to heterogeneous ion distribution within the electrode material. Moreover, repeated electrochemical cycling often triggers a series of phase transitions, such as order–disorder transformations, two-phase boundary migration, and crystallographic reconfigurations, which align well with the proposed multistep phase transition mechanism in TiO_2. These findings also provide a broader conceptual framework for understanding phase evolution phenomena in nanocrystalline transition metal oxides.

In transition metal oxide systems such as TiO_2, structural defects, particularly oxygen vacancies (OVs) within nanocrystalline regions, play a critical role in enhancing ionic conductivity by facilitating ion hopping [173, 174]. In addition to their impact on ion transport, such defects also profoundly influence the electronic properties of TiO_2. Among various types of defects, OVs and cationic vacancies are especially prevalent, and their presence can significantly alter the intrinsic physical and chemical properties of the material (Figs. 14(a) and 14(b)) [175]. Consequently, defect engineering has emerged as a powerful strategy to tune the ionic conductivity and electronic structure of TiO_2, which has attracted increasing attention in recent decades.

Numerous studies have demonstrated that treatment under reducing atmospheres, such as hydrogen [173], ammonia (NH_3) , or with reductive metals like Mg and Al at elevated temperatures [176, 177], promotes the formation of oxygen vacancies in TiO_2. Alternative methods such as high-energy laser irradiation [178] and room-temperature lithium-induced reduction via mechanical grinding have also proven effective for defect engineering. The presence and concentration of oxygen vacancies can be characterized using techniques such as electron paramagnetic

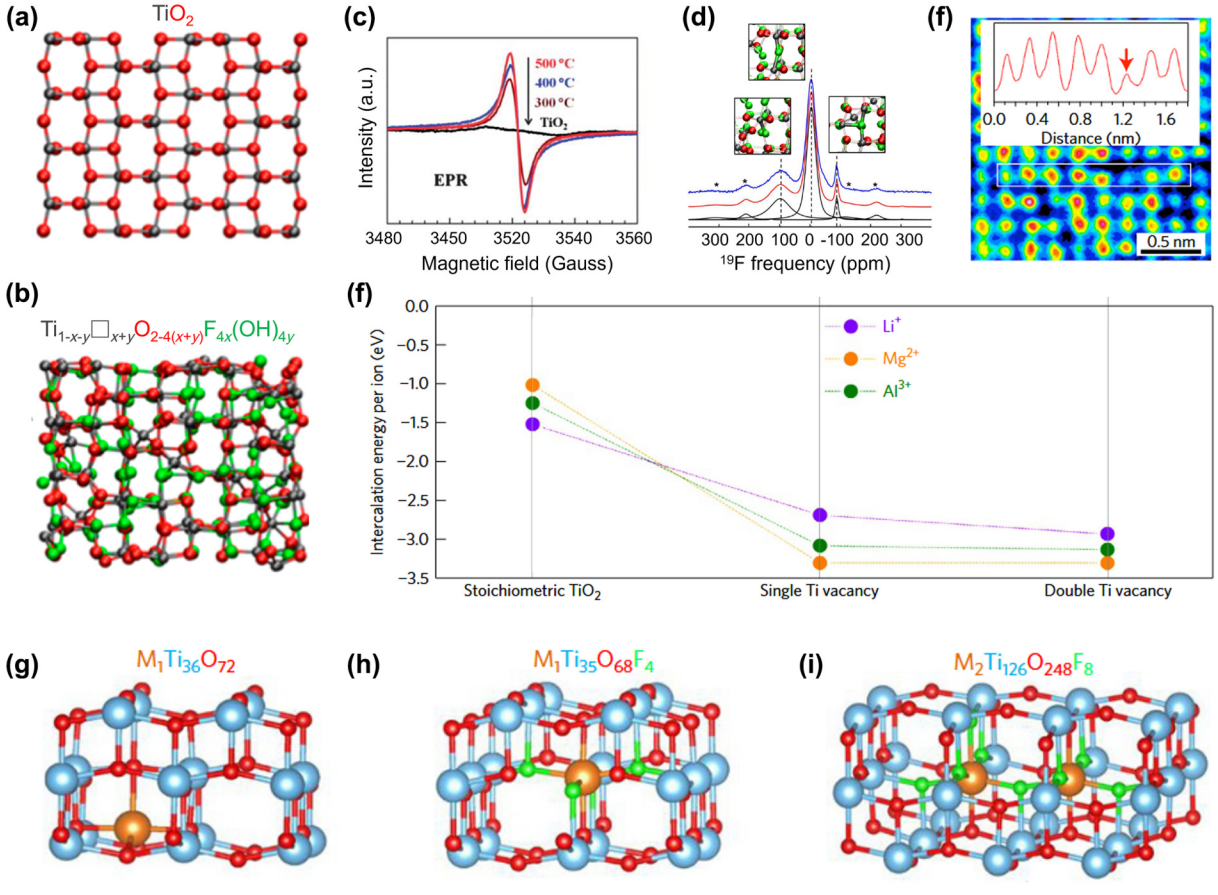

Figure 14 Structure representation of (a) TiO_2(A), (b) $Ti_{1-x-y}\square_{x+y}O_{2-4(x+y)}F_{4x}(OH)_{4y}$ (ball-stick model, gray = Ti, red = O, green=F or OH). (c) EPR spectra of Ovs in TiO_{2-x} and pristine TiO_2 as a reference sample at different temperature. (d) Experimental (in blue) ^{19}F solid-state MAS (60 kHz) NMR spectrum of one of $Ti_{1-x-y}\square_{x+y}O_{2-4(x+y)}F_{4x}(OH)_{4y}$. Fitted (in red) with three NMR lines (in black, indicated by vertical dashed lines), which are assigned to $Ti_1\square_2$-F, $Ti_2\square_1$-F, and Ti_3–F (from left to right) environments. Asterisks denote the spinning sidebands. (e) A coloured HR-TEM image with a profile plot along a selected atomic row (white rectangle) shows clear intensity variations in both atomic columns and dark regions, indicating the presence of structural defects. (f) DFT-calculated insertion energies for Li, Mg, and Al in TiO_2(A) and in F-doped TiO_2(A) with different Titanium vacancies defects [179]. (g–i) From left to right, corresponding structural representations of the insertion sites in stoichiometric (defect-free) TiO_2(A), single-vacancy $Ti_{35}\square_1O_{68}F_4$ and double-vacancy $Ti_{126}\square_2O_{248}F_8$. (a, b, d) Reproduced with permission from Ref. [179]. © 2015 American Chemical Society. (c) Reproduced with permission from Ref. [177], © 2013 The Royal Society of Chemistry. (e–i) Reproduced with permission from Ref. [180], © 2017 Macmillan Publishers Limited, part of Springer Nature.

resonance (EPR) and thermogravimetric analysis (TGA). A strong EPR signal at g = 2.002 is generally indicative of oxygen vacancies in TiO_2 samples (Fig. 14(c)). Additionally, oxygen-deficient materials display reduced mass loss in oxidative atmospheres in the TGA testing compared to measurements performed under inert conditions, due to oxygen uptake. Additionally, XPS can be used to estimate the stoichiometry and oxidation state of titanium by analysing the Ti 2p peak area ratios [139].

Furthermore, substitutional doping of O^{2-} anions with monovalent anions such as F^- or OH^- can induce the formation of cationic Ti^{4+} vacancies (□), with the defect concentration controllable via reaction temperature. Dambournet et al. [179, 180], successfully introduced such cationic Ti^{4+} vacancies in TiO_2 through F^- or OH^- doping, as evidenced by solid-state NMR and high-resolution TEM analyses (Figs. 14(d) and 14(e)). These Ti^{4+} vacancies act as shallow acceptor states that enhance charge carrier density, thereby improving both electronic and ionic conductivities. Moreover, the introduction of cationic vacancies provides additional insertion sites, leading to significantly improved capacity and rate performance compared to pristine TiO_2.

Notably, Ti^{4+} vacancies also enable the reversible insertion of of multivalent ions such as Mg^{2+} and Al^{3+}. Density functional theory (DFT) calculations comparing the insertion energies of Li^+, Mg^{2+}, and Al^{3+} in both pristine TiO_2(A) and F-doped TiO_2(A) with titanium vacancies confirm more favorable energetics (i.e., lower insertion energies) in the defect-engineered systems (Fig. 14(f)). The corresponding atomic configurations of insertion sites in stoichiometric, single-vacancy, and double-vacancy TiO_2(A) structures are illustrated in Figs. 14(g)–14(i), further highlighting the defect-enabled enhancement of ion insertion.

Furthermore, defects such as dangling bonds, vacancies, and impurities—more prevalent in amorphous TiO_2, can act as scattering centers or charge traps, thereby impairing electronic conductivity. A recent study investigating the relationship between atomic order and electrochemical performance revealed that Na^+ diffusion in disordered TiO_2 was nearly 300 times faster than in long-range ordered TiO_2 (6.56×10^{-10} $cm^2 \cdot s^{-1}$ vs. 2.11×10^{-12} $cm^2 \cdot s^{-1}$) [181]. This enhancement in ion mobility is largely attributed to the structural disorder, which facilitates ion transport by eliminating energy barriers associated with ordered lattice sites. Moreover, the amorphous structure accommodates insertion with minimal volume expansion, consistent with a pseudocapacitive mechanism, thereby enabling excellent rate capability and high reversible capacity. Although structural disorder enhances ionic conductivity, it often compromises electronic conductivity due to intrinsic limitations. Unlike crystalline TiO_2, which possesses long-range periodicity conducive to band conduction, amorphous TiO_2 lacks such structural coherence. This disorder leads to the localization of electron wavefunctions, thereby reducing carrier mobility and shifting the dominant electronic transport mechanism from band conduction to thermally activated hopping [182].

In brief, defects in TiO_2 significantly influence its ion storage behavior by introducing additional ion storage sites, modulating electron transport pathways, and facilitating redox processes. More intriguingly, defects can also dictate whether phase transitions occur during electrochemical cycling. For instance, in MoO_3, transition metal oxide with electrochemical properties analogous to TiO_2, lithium insertion leads to the disappearance of distinct XRD reflections and the emergence of broad peaks upon delithiation, indicative of a new nanoparticulate phase formation [139, 183]. This behavior resembles the electrochemically driven phase transition reported in TiO_2. However, when oxygen vacancies are introduced into MoO_3 (i.e., MoO_{3-x}), the phase transition is effectively suppressed during the (de)lithiation process [139], suggesting that oxygen deficiency stabilizes the lattice and inhibits structural reorganization. These observations highlight the critical role of both cationic and anionic vacancies in modulating electrochemical phase behavior. Accordingly, rational design strategies for TiO_2-based materials should incorporate precise control over defect type and concentration, enabling the optimization of ion transport, phase stability, and overall electrochemical performance.

3.3 Morphologies

The morphology of TiO_2 plays an indirect yet crucial role in governing ion diffusion pathways, the formation of conductive networks, the density of electrochemically active sites, and the overall structural stability of the electrode. Tailoring TiO_2 electrode architectures, by employing structures of varying dimensionalities such as nanorods, nanosheets, and nanoparticles with distinct surface areas, offers a highly effective strategy to improve electrochemical performance. Accordingly, the following section will systematically examine how different electrode morphologies influence ion storage mechanisms from both macroscopic and microscopic perspectives.

Over the past few decades, a diverse array of nanostructured TiO_2 materials, including one-dimensional (1D) nanorods/nanotubes (Figs. 15(a)–15(c)) [175, 184–189], two-dimensional (2D) nanosheets (Figs. 15(d)–15(f)) [190–194], and three-dimensional (3D) nanoparticles (Figs. 15(g)–15(i)) [157, 195–199], have been synthesized and extensively explored for applications in LIBs and SIBs. Morphologies characterized by high surface areas provide a larger number of electrochemically active sites for ion adsorption and insertion, thereby significantly boosting charge storage capacity [82, 101]. Furthermore, specific morphologies offer improved structural resilience; for instance, hollow or porous architectures effectively buffer the volumetric changes associated with ion insertion/extraction, mitigating mechanical degradation such as particle pulverization and thereby improving capacity retention and prolonging cycle life.

Moreover, different TiO_2 morphologies can expose distinct crystalline facets, such as the high-energy {001} or the thermodynamically stable {101} facets of anatase, which exhibit varying surface energies and ion adsorption capacities. These crystallographic differences can directly influence the ion storage behavior of TiO_2 electrodes [57]. Recent studies on single-crystal electrodes have demonstrated that the anatase (101) facet is particularly favorable for ion insertion due to its high permeability to Li^+/Na^+ ions [200–202].

Recently, the rational design of hierarchical and porous TiO_2 structures has attracted considerable attention as a means to simultaneously improve energy/power densities and cycling stability. Despite these advances, the underlying microscopic mechanisms through which morphology influences electrochemical performance remain incompletely understood. Therefore, this section aims to elucidate the relationship between electrode morphology and charge transport behavior, and to clarify the ion storage mechanism in TiO_2 from a morphological perspective.

3.3.1 *One-dimensional (1D)*

One-dimensional (1D) nanomaterials are characterized by having

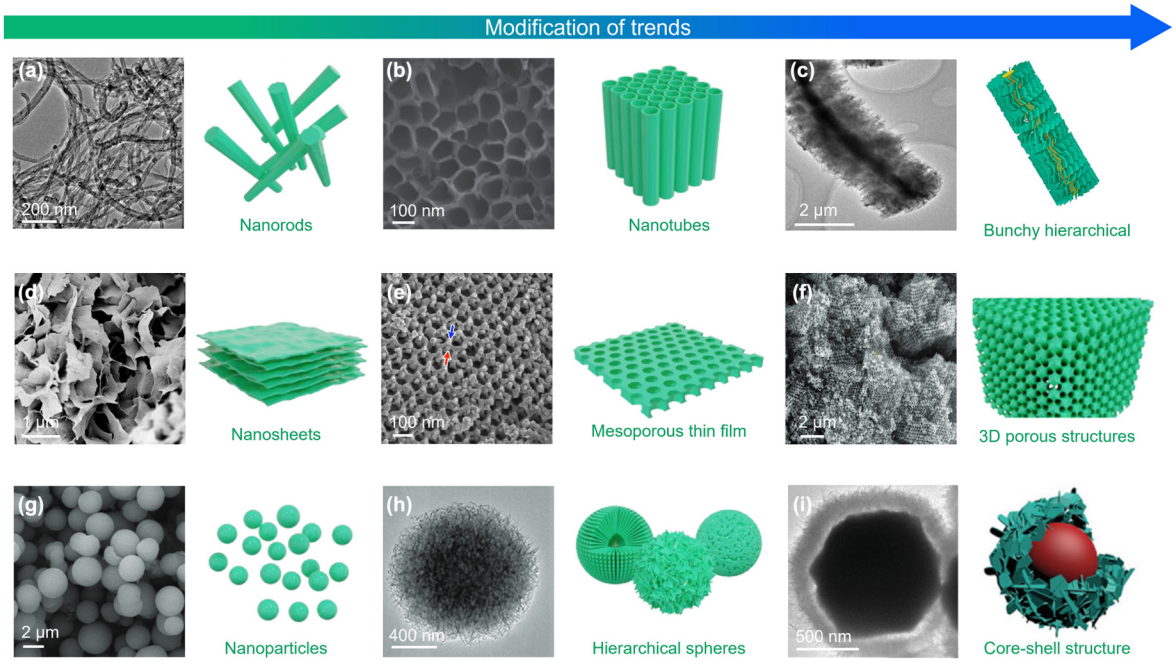

Figure 15 Selected schematic illustrations of typical TiO_2-based electrode materials—including nanorods/nanowires/nanofibers, nanotubes, bunchy hierarchical, nanoparticles, various spherical structures, nanosheets, mesoporous thin film and 3D porous architectures—are presented from a modification perspective. (a) Multiwalled carbon nanotubes incorporated TiO_2 nanorods. Reproduced with permission from Ref. [188], © 2017 WILEY-VCH Verlag GmbH & Co. KGaA, Weinheim. (b) Self-supported nanotube arrays of TiO_2. Reproduced with permission from Ref. [186], © 2016 WILEY-VCH Verlag GmbH & Co. KGaA, Weinheim. (c) Bunchy hierarchical structure TiO_2. Reproduced with permission from Ref. [189], © 2022 Liu, S. et al. (d) TiO_2 nanosheets. Reproduced with permission from Ref. [192], © 2018, American Chemical Society. (e) Mesoporous TiO_2 thin film. Reproduced with permission from Ref. [194], © 2020 Tsinghua University Press and Springer-Verlag GmbH Germany, part of Springer Nature. (f) Three-dimensionally ordered macroporous TiO_2. Reproduced with permission from Ref. [190], © 2012 WILEY-VCH Verlag GmbH & Co. KGaA, Weinheim. (g) TiO_2 solid spheres obtained by asymmetric Ostwald ripening. Reproduced with permission from Ref. [198], © 2016 WILEY-VCH Verlag GmbH & Co. KGaA, Weinheim. (h) Spontaneous assembly of TiO_2 three-dimensional hierarchical spheres. Reproduced with permission from Ref. [157], © 2010 American Chemical Society. (i) Yolk–shell TiO_2 microspheres. Reproduced with permission from Ref. [196], © 2015 WILEY-VCH Verlag GmbH & Co. KGaA, Weinheim.

one extended spatial dimension (typically along the *x*-axis) significantly larger than the other two dimensions (*y* and *z*), which are confined to the nanoscale. These structures generally possess high aspect ratios (often >10, and in some cases exceeding 1000), with lengths extending into the micrometer range or beyond. Ion transport in such 1D architectures is primarily dominated by axial diffusion, while tip-induced electric field enhancements at the ends can further promote localized ion adsorption.

Examples like TiO_2 nanorods, nanotubes and nanowires [185, 203, 204], all of which provide optimized pathways for ion diffusion. The anisotropic structure and large surface-to-volume ratio of these materials contribute to enhanced charge/discharge rates. Typically, TiO_2 nanotubes are synthesized via electrochemical anodization of Ti foil [41, 175, 186, 205], whereas TiO_2 nanorods and nanowires commonly obtained by modulating reaction time and temperature during the final dehydration step of a hydrothermal synthesis process [203, 204]. Low-temperature synthesis strategies have also been reported as viable alternatives [206, 207]. Among these structures, nanorods offer a relatively large surface area and reduced surface strain, while nanotubes, owing to their hollow geometry, provide even greater surface area and porosity. Electrochemically, these 1D TiO_2 electrodes often display sloped galvanostatic charge/discharge (GCD) profiles during ion (de)intercalation [78, 186, 208], in contrast to conventional insertion compounds, which typically exhibit flat voltage plateaus associated with two-phase reactions. As particle size decreases, voltage profiles shift toward more sloping curves [209], indicating a transition to solid-solution or pseudocapacitive behavior.

Furthermore, the tubular or rod-like morphologies offer open-channel structures that facilitate rapid mass transport [205]. In some cases, TiO_2 nanotubes and nanorods are coated with conductive networks such as few-layer graphene to enhance electronic conductivity [184], or are engineered into hierarchical and bunchy architectures that support rapid pseudocapacitive responses [189]. In these systems, the electrode surface acts as a host for solid-solution–like ion insertion, where surface free energy varies continuously with ion concentration. Such behavior may be attributed to curvature-induced strain effects within the nanotube walls, which modulate the local surface energy landscape during ion adsorption and insertion [102].

3.3.2 *Two-dimensional (2D)*

Two-dimensional (2D) materials are characterized by their extensive lateral dimensions along the *x*- and *y*-axes, while being atomically thin along the *z*-axis. Such structural anisotropy, exemplified by single-layer graphene or few-layer MoS_2, imparts remarkable electrical and mechanical properties due to quantum confinement in the thickness direction. In the context of TiO_2-based electrodes, 2D morphologies, particularly nanosheets, offer high specific surface areas and ultrathin profiles, which greatly enhance electrode–electrolyte interfacial contact and facilitate efficient charge transport and ion storage. These attributes are critical for improving electrochemical performance.

The flat, thin morphology of TiO_2 nanosheets enables superior ion transport kinetics. The enlarged surface area increases the number of electrochemically active sites and enhances electrode–electrolyte contact, while the short diffusion lengths

inherent to the nanosheet architecture accelerate ion migration, collectively contributing to improved rate capability in TiO_2 and capacity. Common synthesis techniques for TiO_2 nanosheets include hydrothermal processes [210–212], atomic layer deposition (ALD) [213, 214], and templating strategies [193, 194]. These methods yield nanosheets with high electrolyte permeability, reduced overpotential, and fast reaction kinetics [192, 193, 214]. For instance, ALD-fabricated amorphous TiO_2 coatings with thicknesses of 3–10 nm on carbon templates have achieved surface areas up to 467 $m^2 \cdot g^{-1}$ after calcination [213].

From an electrochemical standpoint, several features contribute to the superior performance of nanosheet-based TiO_2 electrodes: (a) High surface area. It enhances ion accessibility and electrode–electrolyte interface, promoting faster electron and ion transport. (b) Short ion diffusion paths. The thin nature of nanosheets minimizes diffusion lengths, accelerating reaction kinetics. For example, mesoporous TiO_2 nanosheets have achieved capacities up to 280 $mAh \cdot g^{-1}$, approaching the theoretical limit of 335 $mAh \cdot g^{-1}$, compared to ~168 $mAh \cdot g^{-1}$ for bulk TiO_2 [214]. (c) Improved conductive network. When combined with conductive scaffolds such as graphene foam or nitrogen-doped graphene layers, electron transport is significantly enhanced [193, 212, 215].

While ion storage in bulk TiO_2 predominantly involves insertion, 2D morphologies also enable pseudocapacitive behavior, characterized by surface-controlled redox reactions. This mechanism provides faster kinetics and higher capacities than bulk diffusion-limited insertion. The ultrathin nature of TiO_2 nanosheets maximizes surface exposure and facilitates electrolyte penetration, enabling rapid ion uptake and release. For instance, hybrid TiO_2 nanosheets demonstrated significantly enhanced pseudocapacitive characteristics, delivering a specific capacity of 120 $mAh \cdot g^{-1}$ at 1 $A \cdot g^{-1}$ and retaining 90% capacity over 2500 cycles, highlighting their excellent rate capability and cycling stability [216]. These traits are particularly valuable for fast-charging energy storage applications.

However, despite their initial electrochemical advantages, TiO_2 nanosheets are prone to morphological instability during prolonged cycling. 2D Structural degradation such as aggregation, restacking, or collapse of nanosheets can reduce active surface area and disrupt ionic transport pathways. For instance, TiO_2 nanobelts were reported to form ~100 nm aggregates after just 10 cycles, resulting in severe surface area loss and a drop in capacity retention to only 23% [217]. These findings underscore that while 2D TiO_2 architectures enable rapid ion transport and high initial capacity, their mechanical fragility presents challenges for long-term durability.

3.3.3 *Three-dimensional (3D)*

Three-dimensional (3D) materials exhibit comparable dimensions along all three spatial axes (*x*, *y*, and *z*), typically ranging from nanometers to micrometers, and are not confined in any particular direction. This structural isotropy imparts stability and facilitates morphology tailoring and structural modification without pronounced geometric constraints. In this context, TiO_2 nanoparticles have garnered significant attention owing to their unique nanoscale effects and tunable physicochemical properties. It is well established that the electrochemical performance of TiO_2 nanoparticles is highly dependent on particle size, morphology, and structural uniformity.

Over the past decade, various synthetic methodologies, including liquid-phase synthesis (e.g., sol–gel) [19, 195, 198, 218], solid-state synthesis [219, 220], and alternative routes such as laser ablation [221], have been developed to fabricate TiO_2 nanoparticles with tailored characteristics. Among them, the liquid-phase route is widely employed due to its simplicity and scalability. However, uncontrolled synthesis often leads to heterogeneous particle size distributions and aggregation. To address this issue, Hu and Mahshid et al. [195, 222] firstly systematically investigated the effects of pH and temperature during hydrothermal synthesis, achieving uniform, nearly spherical TiO_2 nanoparticles (5–30 nm) under acidic conditions that suppressed agglomeration. To further optimize the electrochemical performance, hierarchical nanostructures, such as hollow spheres and yolk–shell architectures, have been developed [157, 198]. These open frameworks enhance ion transport by improving the electrode-electrolyte interfacial area and accommodating volumetric changes during cycling. The performance of such nanostructured TiO_2 materials is strongly governed by the interplay among crystal chemistry, surface ion concentration, and particle morphology. For example, Bruce et al. [78] demonstrated that TiO_2 nanoparticles exhibit superior lithium storage capacity and rate capability compared to bulk, nanorod, and nanosheet counterparts, particularly at voltages below 1.4 V. This enhanced performance was attributed to high surface area and nanoscale-induced structural distortions, which significantly alter the ion insertion behavior. Their findings also highlight the necessity of advanced characterization techniques to elucidate such distortions and support the multistep phase transition mechanism in nanoparticulate TiO_2.

In addition to structural design, surface modification, especially carbon coating, has emerged as an effective strategy to improve the electrical conductivity of TiO_2 electrodes. Various carbon materials, including amorphous carbon, graphene, and carbon nanotubes, have been integrated with TiO_2 [218, 223, 224]. Among these, amorphous carbon is most widely employed due to its ability to uniformly coat particles and significantly boost electronic conductivity [225]. Incorporation of conductive carbon networks facilitates efficient electron transport, thereby enhancing overall electrode performance.

More importantly, most investigations into ion transport, size effects, and pseudocapacitive contributions have been primarily centered on TiO_2 nanoparticles. In addition to these well-known benefits, it exhibits a unique advantage to observe the multistep phase transformation [61–63]. This structural evolution effectively mitigates the crystallographic anisotropy that typically restricts ion insertion to specific surfaces in bulk crystalline TiO_2. This indicates that different electrode morphologies and structural configurations may influence the formation of percolation pathways and ion transport, thereby affecting the overall electrochemical performance. In addition to morphologies engineering, surface modification through carbon coatings has proven to be an effective approach to improve the conductivity of nanoparticles TiO_2 electrodes. Various carbon nanomaterials—including amorphous carbon, graphene, and carbon nanotubes—have been employed for this purpose [218, 223, 224]. Among these, amorphous carbon is particularly widely used due to its ability to form uniform coatings and significantly enhance the electrical conductivity of TiO_2 [225]. The incorporation of carbon additives has consistently been shown to improve electron transport within the electrode, thereby boosting the overall electrochemical performance.

The relationship between electrode architecture and charge transport in TiO_2 is reflected in multiple aspects, including ion

diffusion paths, conductive network formation, and electrochemically active site density. In brief, 1D TiO_2 structures (e.g., nanowires, nanotubes) and 2D architectures (e.g., nanosheets) offer high surface areas and well-defined ion transport channels, facilitating fast (de)intercalation and improved rate capabilities. 3D TiO_2 nanoparticles, owing to their shortened ion diffusion lengths, provide more direct and efficient ion diffusion pathways, significantly reducing tortuosity compared to their bulk counterparts (Fig. 16). In contrast, bulk TiO_2 materials exhibit long diffusion paths, which hinder ion mobility and reduce performance.

Amorphous TiO_2, in particular, provides continuous ion diffusion pathways, minimizing resistance compared to its crystalline counterparts. Although studies on the intrinsic properties of amorphous TiO_2 nanotubes and their influence on electrochemical behavior remain limited, it is generally accepted that nanostructures with high surface areas enhance ion adsorption and insertion, leading to increased ion storage capacity. Furthermore, in high surface area morphologies, ion transport is not solely governed by bulk-phase diffusion but is also significantly influenced by surface-confined charge transfer processes. Such surface-limited mechanisms are less pronounced in bulk or low-surface-area electrodes, underscoring the importance of morphology in modulating ion adsorption and desorption dynamics.

In summary, TiO_2 materials with different morphologies exhibit distinct specific surface areas, which play a pivotal role in determining their electrochemical performance. Morphologies characterized by high surface areas provide a greater number of electrochemically active sites and improve the interfacial contact between the electrode and electrolyte. In particular, the increased surface area in nanostructured TiO_2 facilitates a more uniform current density distribution, thereby enhancing electrode kinetics and overall reaction efficiency. Without these structural optimizations, ion transport becomes sluggish, especially in bulk phases, leading to compromised electrochemical performance. Beyond providing additional active sites, electrode morphology also indirectly affects ion storage mechanisms by modulating charge transport pathways and the kinetics of electrochemical reactions. Specifically, nanostructured morphologies shorten ion diffusion lengths, enhance structural integrity during cycling, and promote the exposure of specific high-energy crystalline facets, each of which contributes to improved electrochemical reversibility and rate performance. Collectively, these morphological attributes play a critical role in governing the ion storage behavior and overall electrochemical performance of TiO_2-based electrode materials.

3.4 Electrochemical factors

Electrochemical factors, such as charge–discharge rate, voltage window, and electrolyte composition, play pivotal roles in regulating ion (de)intercalation and (de)adsorption processes in TiO_2, thereby significantly impacting its ion storage mechanisms and overall electrochemical performance. The charge–discharge rate directly influences ion transport kinetics; at high rates, kinetic limitations often restrict ion diffusion, reduce specific capacity, and suppress phase transition processes. The voltage window governs the depth of (de)intercalation, as operating outside of optimal voltage ranges can induce irreversible structural transformations or trigger complex multiphase transitions in the TiO_2 lattice. Meanwhile, the composition of the electrolyte affects ionic conductivity, ion solvation dynamics, and the formation of the solid electrolyte interphase, all of which determine ion accessibility and structural stability during cycling. Collectively, these electrochemical parameters critically modulate the phase transition behavior and govern the energy storage characteristics of TiO_2-based electrodes.

3.4.1 Charge-discharge rate

The charge–discharge rate, or C-rate, which defines the rate at which a battery is charged or discharged relative to its capacity,

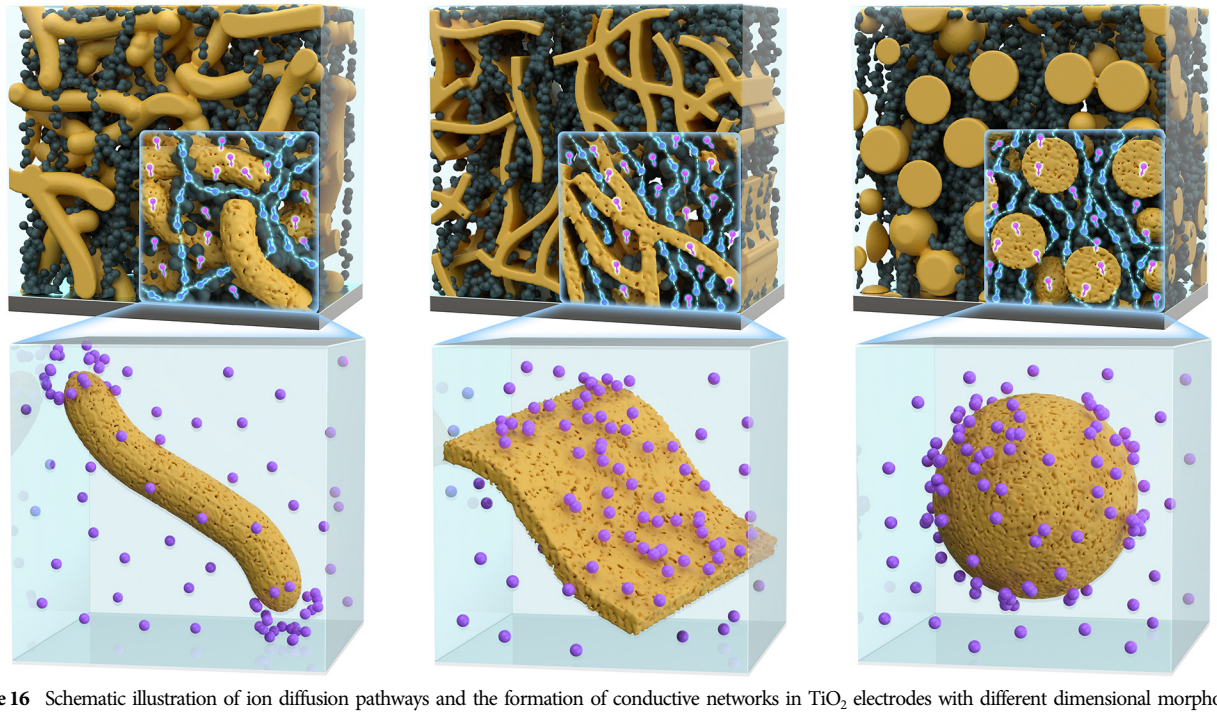

Figure 16 Schematic illustration of ion diffusion pathways and the formation of conductive networks in TiO_2 electrodes with different dimensional morphologies (1D, 2D, and 3D). Distinct morphological features lead to varying ion transport efficiencies and electronic conductivities, which in turn influence the electrochemical performance and ion storage mechanisms.

significantly affects the electrochemical performance of TiO_2. At high C-rates, polarization effects are exacerbated, leading to reduced capacity utilization due to the inherently limited ionic and electronic conductivity of TiO_2. In contrast, at low C-rates, ions have sufficient time to diffuse into the bulk of TiO_2, enabling more thorough utilization of the active material. Therefore, several studies have reported that high charge–discharge rates can prolong the activation process, resulting in a gradual increase in capacity over the initial cycles, a phenomenon that is less pronounced under low C-rate conditions. For instance, when comparing the cycling performance of nitrogen-doped carbon-modified TiO_2 at 1C and 25C, the specific capacity at 25C exhibited a gradual increase over the first 100 cycles, whereas such behavior was minimal at 1C [198]. Similar trends have been observed in other studies as well [57, 218, 226, 227].

This progressive capacity increase is commonly attributed to the gradual activation of previously underutilized regions within the electrode. Under high C-rate cycling, phase transformations may initially occur only near the surface or proceed non-uniformly due to kinetic limitations. Over repeated cycles, ions gradually diffuse into deeper bulk regions, completing phase transitions and enabling broader material participation in the electrochemical reactions. In particular, the formation of a rock-salt phase during cycling enhances ion accessibility and contributes to capacity recovery. This behavior is especially prominent in nanostructured TiO_2, where reduced diffusion lengths facilitate faster ion transport even at elevated C-rates. Consequently, the influence of charge–discharge rate on the ion storage mechanism of TiO_2 has been increasingly recognized, particularly with regard to its role in driving electrochemically induced phase transitions.[62,63,77]

3.4.2 *Voltage window*

The voltage window is a critical parameter that directly influences the electrochemical stability, capacity, and phase transition behavior of TiO_2. In LIBs, TiO_2 typically operates within a voltage window of 1.0–3.0 V vs. Li^+/Li (equivalent to −2.04 to −0.04 V vs. the standard hydrogen electrode, SHE), with the Ti^{4+}/Ti^{3+} redox activity occurring primarily at plateaus between 1.6–1.9 V. This voltage range ensures safe operation by suppressing lithium dendrite formation and minimizing electrolyte decomposition, but it also limits the electrochemical driving force required to induce structural reorganization, such as multiphase transitions. In contrast, SIBs typically employ a wider cut-off voltage range of 0.01–3.0 V vs. Na^+/Na (−2.70 to 0.29 V vs. SHE) to accommodate the larger ionic radius and distinct insertion characteristics of Na^+. The lower cut-off voltage is often necessary to overcome the higher activation energy barrier for initial Na^+ insertion into the TiO_2 lattice, which is frequently accompanied by a crystalline-to-amorphous phase transition [63]. However, operating at such low voltages can also trigger irreversible electrolyte decomposition, complicating the identification of the underlying cause of capacity loss.

For example, Kim et al. [54] reported an unusually high first-discharge capacity of over 700 $mAh{\cdot}g^{-1}$ in TiO_2, with three distinct voltage plateaus and a substantial irreversible capacity loss of more than 500 $mAh{\cdot}g^{-1}$, resulting in an ICE of less than 30%. When the lower cut-off voltage was raised to 0.3 V and 0.8 V, the irreversible capacities were still significant, approximately 452 and 318 $mAh{\cdot}g^{-1}$, respectively. Since electrolyte decomposition is unlikely at these higher voltages, the observed irreversible capacity loss is more plausibly attributed to intrinsic structural changes within TiO_2, such as irreversible phase transitions. Although TiO_2 also exhibits irreversible capacity loss in LIBs, the extent is generally lower than that observed in SIBs, owing to the narrower voltages window and differences in electrolyte composition [90].

Therefore, precise control and optimization of the voltage window are essential for disentangling the contributions of electrolyte decomposition (e.g., SEI formation) and intrinsic structural evolution (e.g., phase transitions) to the observed irreversible capacity loss. However, systematic studies aimed at differentiating these mechanisms remain scarce in the current literature.

Interestingly, voltage window manipulation has yielded surprising results in other electrode systems as well. For instance, Yi Cui et al. [228] reported that tailored voltage pulse protocols could facilitate capacity recovery in silicon-based negative electrodes. More recently, Qiu et al. [137] demonstrated that adjusting the cut-off voltages in Li-rich layered and rocksalt-structured materials could induce a dynamic disorder–order transition, with evolving discharge voltage profiles indicative of electrochemically driven structural reconstruction.

3.4.3 *Electrolyte*

In LIBs, the most commonly used electrolytes are composed of lithium hexafluorophosphate ($LiPF_6$) dissolved in organic carbonate solvents, such as propylene carbonate (PC), ethylene carbonate (EC), diethyl carbonate (DEC), and dimethyl carbonate (DMC). In contrast, ether-based solvents, such as dimethoxyethane (DME), tetrahydrofuran (THF), and diethylene glycol dimethyl ether (diglyme), are rarely utilized in LIBs due to their distinct chemical properties, limited electrochemical stability, and poor compatibility with conventional LIB electrode materials. For instance, ether-based electrolytes typically exhibit an electrochemical stability window of 0–4.0 V vs. Li^+/Li, whereas LIBs often operate at higher cut-off voltages (≥4.3 V), exceeding the oxidative stability limit of ether solvents. This can lead to electrolyte degradation, gas evolution, and diminished battery performance, rendering ether-based systems unsuitable for high-energy-density LIB applications. Moreover, low-molecular-weight ethers such as DME are prone to co-insertion with Li^+ into the graphite negative electrode, causing exfoliation and irreversible structural damage, which further limits their practical application in LIBs.

Conversely, in SIBs, the lower operating voltage of Na^+-insertion positive electrode materials, such as polyanionic or Prussian blue analogs, which typically function within 2.5–3.8 V vs. Na^+/Na, falls well within the electrochemical stability window of ether-based electrolytes. This compatibility effectively mitigates the oxidative decomposition issues encountered in high-voltage LIBs. Consequently, ether-based electrolytes offer several advantages in SIB applications. Their strong solvation capabilities enable the effective dissolution of sodium salts, resulting in high ionic conductivity (~10^{-3} $S{\cdot}cm^{-1}$). Additionally, their low viscosity (e.g., DME: ~0.46 cP vs. EC/DMC: 1–2 cP) promotes rapid Na^+ diffusion and improved rate performance. In contrast, carbonate-based electrolytes often result in the formation of a thicker SEI layer and increased interfacial resistance, both of which hinder electrochemical kinetics.

Therefore, the choice of electrolyte plays a critical role in determining the electrochemical performance of TiO_2 electrodes in both LIBs and SIBs by influencing key parameters such as ionic conductivity, SEI formation, and interfacial compatibility [59, 229–232]. A systematic summary of the effects of different

electrolytes different electrolytes on the ion storage mechanism of TiO_2 is presented in Table 3.

For example, detailed studies by T. Y. Zhang et al. [59] revealed a marked contrast in the electrochemical behavior of TiO_2 when using different electrolytes. In EC/DEC-based electrolytes, TiO_2 did not undergo complete amorphization, even when discharged to 0.01 V during the first cycle. This was confirmed by *ex-situ* XRD and *in-situ* Raman spectroscopy, where characteristic Raman peaks of crystalline TiO_2 remained observable. Complete amorphization was only achieved after approximately four cycles, indicating limited sodium accessibility and lower capacity relative to diglyme-based electrolytes, in which TiO_2 fully transformed to an amorphous phase in the first cycle. A similar trend of incomplete amorphization has also been observed with other ester-

Table 3 Comparison of the electrochemical properties of TiO_2 with varying crystal sizes, morphologies, voltage windows, and electrolyte systems

Morphology (crystal size/nm) [a]	SSA [b] ($m^2 \cdot g^{-1}$)	Discharge capacity		Voltage windows	Electrolyte [c]	Activation [d]	Ref.
		At low rate	At high ate				
Amorphous (particle size: 50 nm)	—[e]	280 mAh·g^{-1} at 1st cycle 185 mAh·g^{-1} at 10th cycle (at 0.3C)	150 mAh·g^{-1} at 1st cycle 140 mAh·g^{-1} at 10th cycle (at 3C)	1.2–3.6 V	1 M $LiPF_6$ in EC: DEC (1:1)	Yes	[233]
Nanoparticles (76.1 nm) (particle size: 200 nm)	10	152 mAh·g^{-1} at 1st cycle 5 mAh·g^{-1} at 22nd cycle (at 0.05C)	—	1.0–3.0 V	1 M $LiClO_4$ in PC	—	[68]
Nanoparticles (17.0 nm) (particle size: 200 nm)	49	—	—				
Nanoparticles (11.0 nm) (particle size: 200 nm)	94	—	—				
Nanoparticles (6.3 nm) (particle size: 200 nm)	223	245 mAh·g^{-1} at 1st cycle 128 mAh·g^{-1} at 50th cycle (at 0.05C)	—				
Nanotube (9–37 nm)	—	280 mAh·g^{-1} at 1st cycle 169 mAh·g^{-1} at 50th cycle (at 0.05C)	70 mAh·g^{-1} at 90th cycle (at 30C)	1.0–2.8 V	1 M $LiPF_6$ in EC: DMC (1:1)	—	[69]
Nanoparticles (7.0 nm)	220	137 mAh·g^{-1} (Data converted from specific capacitance)	—	1.5–2.5 V	1 M $LiClO_4$ in PC	—	
Nanoparticles (10.0 nm)	150	129 mAh·g^{-1} (Data converted from specific capacitance)					
Nanoparticles (30.0 nm)	50	118 mAh·g^{-1} (Data converted from specific capacitance)					
Amorphous (particle size: 2–3 nm)	598	800 mAh·g^{-1} at 1st cycle 200 mAh·g^{-1} at 50th cycle (at 0.1C)	270 mAh·g^{-1} at 1st cycle 125 mAh·g^{-1} at 50th cycle (at 10C)	1.0–3.0 V	1 M $LiPF_6$ in EC: DMC (2:1)	Yes	[234]
Nanorods (5–10 nm)	—	700 mAh·g^{-1} at 1st cycle (at 0.03C) 208 mAh·g^{-1} at 2nd cycle (at 0.03C)	168 mAh·g^{-1} at 2nd cycle (at 0.5C) 92 mAh·g^{-1} at 22th cycle (at 10C) 53 mAh·g^{-1} at 42nd cycle (at 100C)	0.01–3.0 V	1 M $NaClO_4$ in PC with 2% FEC	Yes	[54]
Nanoparticles (30 nm)	—	355 mAh·g^{-1} at 1st cycle (at 0.01C) 155 mAh·g^{-1} at 200th cycle (at 0.1C)	90 mAh·g^{-1} at 50th cycle (at 10C)	0.1–2.0 V	1 M $NaClO_4$ in EC: PC (1:1).	Yes	[49]
Nanoparticles (11 nm)	120	267 mAh·g^{-1} at 1st cycle 226 mAh·g^{-1} at 6th cycle (at 0.1C)	700 mAh·g^{-1} at 1st cycle (at 0.02C) 200 mAh·g^{-1} at 2nd cycle 204 mAh·g^{-1} at 300th cycle (at 1C) 128 mAh·g^{-1} at 2nd cycle 180 mAh·g^{-1} at 500th cycle (at 5C)	0.05–2.0 V	1 M $NaClO_4$ in EC: PC (1:1)	Yes	[218]
Nanoparticles (40 nm)	42	209 mAh·g^{-1} at 1st cycle 182 mAh·g^{-1} at 6th cycle (at 0.1C)	—			—	
Nanoparticles (12 nm)	—	338 mAh·g^{-1} at 1st cycle 251 mAh·g^{-1} at 300th cycle (at 0.25C)	144 mAh·g^{-1} at 1100th cycle (at 2.5C) 75 mAh·g^{-1} at 4000th cycle (at 10C)	0.01–3 V	1 M $NaClO_4$ in PC with 5% FEC	Yes	[224]

(Continued)

Morphology (crystal size/nm)[a]	SSA[b] ($m^2 \cdot g^{-1}$)	Discharge capacity		Voltage windows	Electrolyte[c]	Activation[d]	Ref.
		At low rate	At high ate				
Nanoparticles (15 nm)	124	501 mAh·g^{-1} at 1st cycle 182 mAh·g^{-1} at 300th cycle (at 0.25C)	132 mAh·g^{-1} at 2nd cycle 125 mAh·g^{-1} at 1000th cycle (at 10C)	0.01–2.5 V	1 M $NaClO_4$ in PC with 5% FEC	Yes	[235]
Nanoparticles (19 nm)	76	445 mAh·g^{-1} at 1st cycle 182 mAh·g^{-1} at 300th cycle (at 0.25C)	98 mAh·g^{-1} at 2nd cycle 96 mAh·g^{-1} at 1000th cycle (at 10C)				
Nanoparticles (22 nm)	61	363 mAh·g^{-1} at 1st cycle 182 mAh·g^{-1} at 6th cycle (at 0.1C)	—				
Nanoparticles (18.7 nm)	106.1	445 mAh·g^{-1} at 1st cycle 205 mAh·g^{-1} at 200th cycle (at 0.1C)	383 mAh·g^{-1} at 1st cycle 183 mAh·g^{-1} at 500th cycle (at 0.5C)	0.01–3.0 V	1 M $NaClO_4$ in PC with 5% FEC	Yes	[236]
Nanoparticles (22.5 nm)	80.7	263 mAh·g^{-1} at 1st cycle 183 mAh·g^{-1} at 200th cycle (at 0.1C)	222 mAh·g^{-1} at 1st cycle 135 mAh·g^{-1} at 500th cycle (at 0.5C)				
Nanoparticles (5-10nm) (particle size: 400 nm)	145	360 mAh·g^{-1} at 1st cycle 245 mAh·g^{-1} at 200th cycle (at 0.5C)	95 mAh·g^{-1} at 2nd cycle 90 mAh·g^{-1} at 3000th cycle (at 25C)	0.01–3 V	1 M $NaClO_4$ in PC with 5% FEC	Yes	[198]
Nanorod (10.8–21.3 nm)	122.3	82 mAh·g^{-1} at 84th cycle 123 mAh·g^{-1} at 140th cycle (at 0.15C)	23 mAh·g^{-1} at 2nd cycle 26 mAh·g^{-1} at 31st cycle (at 1.5C)	0.1–2.0 V	1M $NaClO_4$ in PC with 2% FEC	Yes	[57]
Nanorod (10.4–18.4 nm)	103.6	79 mAh·g^{-1} at 84th cycle 88 mAh·g^{-1} at 140th cycle (at 0.15C)	11 mAh·g^{-1} at 2nd cycle 16 mAh·g^{-1} at 31st cycle (at 1.5C)				
Nanorod (13.6–41.2 nm)	89.4	161 mAh·g^{-1} at 84th cycle 180 mAh·g^{-1} at 140th cycle (at 0.15C)	48 mAh·g^{-1} at 2nd cycle 45 mAh·g^{-1} at 31th cycle (at 1.5C)				
Amorphous (Thickness: 3.0 nm)	490	233 mAh·g^{-1} at 2nd cycle 230 mAh·g^{-1} at 5th cycle (at 0.13C)	176 mAh·g^{-1} at 5th cycle (at 50C)	1.0–3.0 V	1 M $LiPF_6$ in EC: DMC (1:1)	No	[237]
Amorphous (Thickness: 7.4 nm)	152	220 mAh·g^{-1} at 2nd cycle 223 mAh·g^{-1} at 5th cycle (at 0.13C)	158 mAh·g^{-1} at 5th cycle (at 50C)				
Amorphous (Thickness: 14 nm)	86	211 mAh·g^{-1} at 2nd cycle 203 mAh·g^{-1} at 5th cycle (at 0.13C)	46 mAh·g^{-1} at 5th cycle (at 50C)				
Nanoparticles (<25 nm)	—	394 mAh·g^{-1} at 1st cycle 216 mAh·g^{-1} at 10th cycle (at 0.15C)	200 mAh·g^{-1} at 2nd cycle 192 mAh·g^{-1} at 500th cycle (at 0.3C) 212 mAh·g^{-1} at 1st cycle 153 mAh·g^{-1} at 2nd cycle 136 mAh·g^{-1} at 600th cycle (at 6C)	0.01–3.0 V	1 M $NaPF_6$ in Diglyme	Yes	[36]
	—	471 mAh·g^{-1} at 1st cycle 180 mAh·g^{-1} at 10th cycle (at 0.15C)	200 mAh·g^{-1} at 2nd cycle 43 mAh·g^{-1} at 500th cycle (at 0.3C)		1 M $NaPF_6$ in EC:DEC (1:1)	Yes (Not obvious)	
Nanoparticles (100 nm)	11	34 mAh·g^{-1} at 1st cycle 41 mAh·g^{-1} at 10th cycle (at 0.3C)	24 mAh·g^{-1} at 50th cycle (at 12C)	0.01–3.0 V	1 M $NaPF_6$ in Diglyme	No	[22]
Nanoparticles (40 nm)	40	76 mAh·g^{-1} at 1st cycle 102 mAh·g^{-1} at 10th cycle (at 0.3C)	58 mAh·g^{-1} at 50th cycle (at 12C)			No	
Nanoparticles (25 nm)	57	131 mAh·g^{-1} at 1st cycle 159 mAh·g^{-1} at 10th cycle (at 0.3C)	92 mAh·g^{-1} at 50th cycle (at 12C)			No	
Nanoparticles (18 nm)	80	142 mAh·g^{-1} at 1st cycle 191 mAh·g^{-1} at 10th cycle (at 0.3C)	118 mAh·g^{-1} at 50th cycle (at 12C)			Yes	
Nanoparticles (10 nm)	133	295 mAh·g^{-1} at 1st cycle 230 mAh·g^{-1} at 10th cycle (at 0.3C)	159 mAh·g^{-1} at 50th cycle (at 12C)			Yes	
Nanoparticles (5 nm)	303	298 mAh·g^{-1} at 1st cycle 236 mAh·g^{-1} at 10th cycle (at 0.3C)	151 mAh·g^{-1} at 50th cycle (at 12C)			Yes	

(Continued)

Morphology (crystal size/nm) [a]	SSA [b] ($m^2 \cdot g^{-1}$)	Discharge capacity		Voltage windows	Electrolyte [c]	Activation [d]	Ref.
		At low rate	At high ate				
Nanoparticles (13.6 nm)	211	337 mAh·g^{-1} at 1st cycle 206 mAh·g^{-1} at 1000th cycle (at 3C)	145 mAh·g^{-1} at 1st cycle 121 mAh·g^{-1} at 20,000th cycle (at 30C)	0.01–3.0 V	1 M $NaPF_6$ in DME	Yes (at high current density)	[238]
Nanoparticles (10 nm)	108	293 mAh·g^{-1} at 1st cycle 255 mAh·g^{-1} at 20th cycle (at 0.3C)	214 mAh·g^{-1} at 3rd cycle 156 mAh·g^{-1} at 5000th cycle (at 6C)	0.01–3.0 V	1 M $NaPF_6$ in Diglyme	Yes	[63]
Amorphous	357	303 mAh·g^{-1} at 1st cycle 155 mAh·g^{-1} at 20th cycle (at 0.3C)	133 mAh·g^{-1} at 3rd cycle 65 mAh·g^{-1} at 5000th cycle (at 6C)				
Nanoparticles (110 nm)	3	20 mAh·g^{-1} after 30 cycles(at 0.3C)	3 mAh·g^{-1} after 30 cycles(at 6C) 2 mAh·g^{-1} after 30 cycles(at 30C)	1.0–3.0 V	1 M $LiPF_6$ in EC:DME:EMC (1:1:1)	No	[62]
		39 mAh·g^{-1} after 30 cycles(at 0.3C)	26 mAh·g^{-1} after 30 cycles (at 6C) 24 mAh·g^{-1} after 30 cycles(at 30C)	0.01–3.0 V	1 M $NaPF_6$ in Diglyme	No	
Nanoparticles (58 nm)	11	91 mAh·g^{-1} after 30 cycles(at 0.3C)	21 mAh·g^{-1} after 30 cycles(at 6C) 12 mAh·g^{-1} after 30 cycles(at 30C)	1.0–3.0 V	1 M $LiPF_6$ in EC:DME:EMC (1:1:1)	Not clear	
		46 mAh·g^{-1} after 30 cycles(at 0.3C)	35 mAh·g^{-1} after 30 cycles(at 6C) 30 mAh·g^{-1} after 30 cycles(at 30C)	0.01–3.0 V	1 M $NaPF_6$ in Diglyme	No	
Nanoparticles (22 nm)	31	133 mAh·g^{-1} after 30 cycles(at 0.3C)	58 mAh·g^{-1} after 30 cycles(at 6C) 27 mAh·g^{-1} after 30 cycles(at 30C)	1.0–3.0 V	1 M $LiPF_6$ in EC:DME:EMC (1:1:1)	Yes	
		95 mAh·g^{-1} after 30 cycles(at 0.3C)	94 mAh·g^{-1} after 30 cycles(at 6C) 72 mAh·g^{-1} after 30 cycles(at 30C)	0.01–3.0 V	1 M $NaPF_6$ in Diglyme	No	
Nanoparticles (15 nm)	62	200 mAh·g^{-1} after 30 cycles(at 0.3C)	112 mAh·g^{-1} after 30 cycles(at 6C) 63 mAh·g^{-1} after 30 cycles(at 30C)	1.0–3.0 V	1 M $LiPF_6$ in EC:DME:EMC (1:1:1)	Yes	
		151 mAh·g^{-1} after 30 cycles(at 0.3C)	147 mAh·g^{-1} after 30 cycles(at 6C) 88 mAh·g^{-1} after 30 cycles(at 30C)	0.01–3.0 V	1 M $NaPF_6$ in Diglyme	Yes	
Nanoparticles (10 nm)	150	228 mAh·g^{-1} after 30 cycles(at 0.3C)	143 mAh·g^{-1} after 30 cycles(at 6C) 72 mAh·g^{-1} after 30 cycles(at 30C)	1.0–3.0 V	1 M $LiPF_6$ in EC:DME:EMC (1:1:1)	Yes	
		227 mAh·g^{-1} after 30 cycles(at 0.3C)	170 mAh·g^{-1} after 30 cycles(at 6C) 98 mAh·g^{-1} after 30 cycles(at 30C)	0.01–3.0 V	1 M $NaPF_6$ in Diglyme	Yes	

Note: [a] Calculated based on Scherrer formula or observed from TEM. [b] Specific surface area, [c] The rates of different literatures have been converted to 1 C=335 mAh·g^{-1}, [d] **A:** large irreversible capacity loss (low ICE), **B**: a distinct capacity increase or **C:** phase transition during the initial cycle. [e] The symbol '— ' indicates that the value/data was not mentioned.

based electrolytes, such as EC/PC [36, 49], suggesting that Na^+ diffusion and storage kinetics are significantly slower compared to those in diglyme-based systems. The superior performance in diglyme-based electrolytes is attributed to the formation of a thinner, more inorganic-rich solid electrolyte interphase, which reduces interfacial resistance and enhances ion transport. This is further supported by a significantly lower charge transfer energy barrier, 172 meV for diglyme versus approximately 410 meV for EC/DEC, derived from temperature-dependent electrochemical impedance spectroscopy using the Arrhenius relationship. More interestingly, pseudocapacitive contributions are markedly enhanced in ether-based electrolytes [94]. This enhancement is ascribed to the high surface potential of amorphous TiO_2 nanoparticles, which facilitates ion adsorption. A recent study investigating the influence of atomic ordering on the electrochemical performance of TiO_2 further supports this view, suggesting that atomic disorder significantly impacts ion storage mechanism by modulating ion adsorption behavior, diffusion kinetics, and electron transport [36, 181].

Notably, Table 3 highlights that both electrolyte composition and the applied cut-off voltage play critical roles in governing the amorphization process. When a diglyme-based electrolyte is conjunction with a low cut-off voltage, full amorphization is consistently observed across multiple studies. Additionally, the inclusion of fluoroethylene carbonate as an electrolyte additive can induce an abnormally high initial discharge capacity, potentially complicating the interpretation of whether amorphization has occurred.

In brief, this section underscores the critical role of electrochemical parameters, including C-rate, voltage window, and electrolyte composition, in dictating the ion storage mechanism of TiO_2. Specifically, under conditions of low C-rate, low cut-off voltage, and the use of diglyme-based electrolytes, multiphase transition phenomena (i.e., crystalline-to-amorphous-to-rock-salt transformations) are frequently observed. These parameters collectively regulate phase transition dynamics and ultimately determine the electrochemical performance of TiO_2-based electrode materials.

4 Summary and outlook

Nanocrystalline TiO_2 exhibits distinctive multiphase transition behavior that has often been overlooked in previous studies.

Whether partial recrystallization or rock-salt phase formation is observed largely depends on the particle size of TiO_2. When the crystallite size is sufficiently small, complete amorphization followed by recrystallization can occur throughout the entire particle, resulting in the disappearance of all XRD diffraction peaks. In contrast, larger particles generally undergo only surface-limited amorphization and phase transition, while the bulk crystalline framework remains intact; hence, XRD peaks are still observable. This size-dependent structural evolution often leads to discrepancies among reported results and contributes to the divergent interpretations of the ion storage mechanism in TiO_2-based electrodes.

In this work, we critically summarize the ion storage mechanisms of TiO_2 across lithium- and sodium-based systems, with particular emphasis on the recently recognized electrochemically induced crystalline-to-amorphous-to-rock-salt phase multistep phase transformation mechanism. Although other mechanisms such as reversible (de)intercalation and amorphization have been proposed derived from distinct experimental observations, they are not necessarily mutually exclusive. On the contrary, these mechanisms may occur concurrently or sequentially within the same system at different stages of cycling.

Through systematically review, we summarize the complete ion storage process in TiO_2 as follows: during the initial discharge, ion insertion induces TiO_2 lattice distortion, ultimately causing a thin surface layer of crystalline TiO_2 to undergo amorphization. Upon continued cycling, partial nucleation occurs within these amorphous regions, resulting in the formation of cubic rock-salt $Li/NaTiO_2$ nanograins. In this highly symmetric rock-salt structure, Ti and Li/Na are randomly distributed over octahedral sites within a nearly ideal cubic close-packed oxygen lattice. The disordered atomic distribution within the newly formed rock-salt structure is maintained even in the fully charged state, which prevents structural collapse and contributes to the thermodynamic stability of the host framework. Meanwhile, some interfacial regions remain amorphous, potentially forming percolation pathways that enhance ion diffusion, primarily governed grain boundary transport rather than bulk diffusion. Importantly, the formation of these amorphous interfacial regions effectively mitigates the crystallographic anisotropy typically associated with ion insertion in bulk TiO_2, thereby enabling more isotropic and efficient ion storage. Furthermore, this structure contributes additional ion storage via surface or insertion-type pseudocapacitive mechanisms [61–63].

Furthermore, we summarize the effects of extrinsic physicochemical factors on the ion storage mechanisms of TiO_2 and propose that the critical role of overcoming nucleation barriers to initiate or accelerate phase transitions, which can be effectively modulated by tuning parameters such as temperature, crystal size, cycling rates, cut-off potentials (voltage window), and electrolyte composition. To further verify this size-dependent phase transition behavior, *operando* characterization techniques such as XRD, XAS, and cryo-TEM are crucial. Particularly, long-term operando measurements can help distinguish whether the observed structural evolution originates from surface-localized or bulk phase transitions in TiO_2 during cycling.

In summary, this review not only suggests that the electrochemical driving force can effectively induce phase transitions in TiO_2 materials but also highlight a rich and underexplored research area with significant potential to advance the understanding of electrochemical phase transitions in other transition-metal oxides. Although the irreversibility of amorphization and subsequent phase transitions may hinder the practical implementation of TiO_2 in full-cell systems, it also reveals an intriguing phenomenon: the self-organization of materials during electrochemical cycling. Such self-driven structural evolution, which has been rarely reported, may offer a simple and generalizable strategy for the *in-situ* synthesis of novel electrode materials [61–63, 77, 239]. This innovative mechanism could enable the discovery of high-energy, high-power, and stable electrode systems that are otherwise inaccessible through conventional synthesis routes. Drawing on findings from Nb_2O_5 and TiO_2 systems, as well as recent studies on other metal oxides [119, 137, 140, 240, 241], we propose that electrochemically driven amorphous and recrystallization in metal oxide electrodes could provide a broadly applicable concept for materials synthesis.

Acknowledgements

This work was financially supported by Shenzhen Science and Technology Plan Project (No. SGDX20230116091644003), Guangdong Major Project of Basic and Applied Basic Research (No. 2023B0303000002), Shenzhen Key Laboratory of Advanced Energy Storage (No. ZDSYS20220401141000001) and High level of special funds (G03034K001).

Declaration of conflicting interests

The authors declare no conflicting interests regarding the content of this article.

Data availability

All data needed to support the conclusions in the paper are presented in the manuscript and/or the Supplementary Materials. Additional data related to this paper may be requested from the corresponding author upon request.

References

[1] Harring, N.; Jönsson, E.; Matti, S.; Mundaca, G.; Jagers, S. C. Cross-national analysis of attitudes towards fossil fuel subsidy removal. *Nat. Clim. Chang.* **2023**, *13*, 244–249.

[2] Chu, S.; Majumdar, A. Opportunities and challenges for a sustainable energy future. *Nature* **2012**, *488*, 294–303.

[3] Armand, M.; Tarascon, J. M. Building better batteries. *Nature* **2008**, *451*, 652–657.

[4] Li, L.; Zheng, Y.; Zhang, S. L.; Yang, J. P.; Shao, Z. P.; Guo, Z. P. Recent progress on sodium ion batteries: Potential high-performance anodes. *Energy Environ. Sci.* **2018**, *11*, 2310–2340.

[5] Tarascon, J. M. Na-ion versus Li-ion batteries: Complementarity rather than competitiveness. *Joule* **2020**, *4*, 1616–1620.

[6] Tan, S. S.; Jiang, Y. L.; Wei, Q. L.; Huang, Q. M.; Dai, Y. H.; Xiong, F. Y.; Li, Q. D.; An, Q. Y.; Xu, X.; Zhu, Z. Z. et al. Multidimensional synergistic nanoarchitecture exhibiting highly stable and ultrafast sodium-ion storage. *Adv. Mater.* **2018**, *30*, 1707122.

[7] Moriwake, H.; Kuwabara, A.; Fisher, C. A. J.; Ikuhara, Y. Why is sodium-intercalated graphite unstable. *RSC Adv.* **2017**, *7*, 36550–36554.

[8] Dou, X. W.; Hasa, I.; Saurel, D.; Vaalma, C.; Wu, L. M.; Buchholz, D.; Bresser, D.; Komaba, S.; Passerini, S. Hard carbons for sodium-ion batteries: Structure, analysis, sustainability, and electrochemistry. *Mater. Today* **2019**, *23*, 87–104.

[9] Cao, Y. L.; Xiao, L. F.; Wang, W.; Choi, D.; Nie, Z. M.; Yu, J. G.; Saraf, L. V.; Yang, Z. G.; Liu, J. Reversible sodium ion insertion in single crystalline manganese oxide nanowires with long cycle life.

Adv. Mater. **2011**, *23*, 3155–3160.
[10] Liu, Q. N.; Hu, Z.; Chen, M. Z.; Zou, C.; Jin, H. L.; Wang, S.; Chou, S. L.; Dou, S. X. Recent progress of layered transition metal oxide cathodes for sodium-ion batteries. *Small* **2019**, *15*, 1805381.
[11] Zhao, C. L.; Wang, Q. D.; Yao, Z. P.; Wang, J. L.; Sánchez-Lengeling, B.; Ding, F. X.; Qi, X. G.; Lu, Y. X.; Bai, X. D.; Li, B. H. et al. Rational design of layered oxide materials for sodium-ion batteries. *Science* **2020**, *370*, 708–711.
[12] Liu, K.; Tan, S. S.; Moon, J.; Jafta, C. J.; Li, C.; Kobayashi, T.; Lyu, H.; Bridges, C. A.; Men, S.; Guo, W. et al. Insights into the enhanced cycle and rate performances of the F-substituted P2-type oxide cathodes for sodium-ion batteries. *Adv. Energy Mater.* **2020**, *10*, 2000135.
[13] Zhang, W.; Wu, Y. L.; Xu, Z. M.; Li, H. X.; Xu, M.; Li, J. W.; Dai, Y. H.; Zong, W.; Chen, R. W.; He, L. et al. Rationally designed sodium chromium vanadium phosphate cathodes with multi-electron reaction for fast-charging sodium-ion batteries. *Adv. Energy Mater.* **2022**, *12*, 2201065.
[14] Saravanan, K.; Mason, C. W.; Rudola, A.; Wong, K. H.; Balaya, P. The first report on excellent cycling stability and superior rate capability of $Na_3V_2(PO_4)_3$ for sodium ion batteries. *Adv. Energy Mater.* **2013**, *3*, 444–450.
[15] Lu, Y. H.; Wang, L.; Cheng, J. G.; Goodenough, J. B. Prussian blue: A new framework of electrode materials for sodium batteries. *Chem. Commun.* **2012**, *48*, 6544–6546.
[16] Fujishima, A.; Honda, K. Electrochemical photolysis of water at a semiconductor electrode. *Nature* **1972**, *238*, 37–38.
[17] Ni, M.; Leung, M. K. H.; Leung, D. Y. C.; Sumathy, K. A review and recent developments in photocatalytic water-splitting using TiO_2 for hydrogen production. *Renew. Sustain. Energy Rev.* **2007**, *11*, 401–425.
[18] Ge, M. Z.; Li, Q. S.; Cao, C. Y.; Huang, J. Y.; Li, S. H.; Zhang, S. N.; Chen, Z.; Zhang, K. Q.; Al-Deyab, S. S.; Lai, Y. K. One-dimensional TiO_2 nanotube photocatalysts for solar water splitting. *Adv. Sci.* **2017**, *4*, 1600152.
[19] Meng, W. J.; Dang, Z. Z.; Li, D. S.; Jiang, L.; Fang, D. N. Interface and defect engineered titanium-base oxide heterostructures synchronizing high-rate and ultrastable sodium storage. *Adv. Energy Mater.* **2022**, *12*, 2201531.
[20] Zhang, W.; Tian, Y.; He, H. L.; Xu, L.; Li, W.; Zhao, D. Y. Recent advances in the synthesis of hierarchically mesoporous TiO_2 materials for energy and environmental applications. *Natl. Sci. Rev.* **2020**, *7*, 1702–1725.
[21] Wang, C.; Zhang, J. S.; Wang, X. F.; Lin, C. F.; Zhao, X. S. Hollow rutile cuboid arrays grown on carbon fiber cloth as a flexible electrode for sodium-ion batteries. *Adv. Funct. Mater.* **2020**, *30*, 2002629.
[22] Wei, Q. L.; Chang, X. Q.; Butts, D.; DeBlock, R.; Lan, K.; Li, J. B.; Chao, D. L.; Peng, D. L.; Dunn, B. Surface-redox sodium-ion storage in anatase titanium oxide. *Nat. Commun.* **2023**, *14*, 7.
[23] Rajagopalan, R.; Tang, Y. G.; Jia, C. K.; Ji, X. B.; Wang, H. Y. Understanding the sodium storage mechanisms of organic electrodes in sodium ion batteries: Issues and solutions. *Energy Environ. Sci.* **2020**, *13*, 1568–1592.
[24] Li, Y. W.; Zhao, Y.; Chen, Q.; Yang, Y.; Liu, Y. S.; Hong, Z. R.; Liu, Z. H.; Hsieh, Y. T.; Meng, L.; Li, Y. F. et al. Multifunctional fullerene derivative for interface engineering in perovskite solar cells. *J. Am. Chem. Soc.* **2015**, *137*, 15540–15547.
[25] Kim, H. S.; Park, N. G. Parameters affecting *I–V* hysteresis of $CH_3NH_3PbI_3$ perovskite solar cells: Effects of perovskite crystal size and mesoporous TiO_2 layer. *J. Phys. Chem. Lett.* **2014**, *5*, 2927–2934.
[26] Nguyen, T. T.; Patel, M.; Kim, S.; Mir, R. A.; Yi, J.; Dao, V. A.; Kim, J. Transparent photovoltaic cells and self-powered photodetectors by TiO_2/NiO heterojunction. *J. Power Sources* **2021**, *481*, 228865.
[27] Zhao, J. H.; Wang, H. Q.; Cai, Y. H.; Zhao, J. J.; Gao, Z. D.; Song, Y. Y. The challenges and opportunities for TiO_2 nanostructures in gas sensing. *ACS Sens.* **2024**, *9*, 1644–1655.
[28] Li, Z.; Yao, Z. J.; Haidry, A. A.; Plecenik, T.; Xie, L. J.; Sun, L. C.; Fatima, Q. Resistive-type hydrogen gas sensor based on TiO_2: A review. *Int. J. Hydrogen Energy* **2018**, *43*, 21114–21132.
[29] Zhang, W. L.; Rhim, J. W. Titanium dioxide (TiO_2) for the manufacture of multifunctional active food packaging films. *Food Packag. Shelf Life* **2022**, *31*, 100806.
[30] Zhang, X. D.; Xiao, G.; Wang, Y. Q.; Zhao, Y.; Su, H. J.; Tan, T. W. Preparation of chitosan-TiO_2 composite film with efficient antimicrobial activities under visible light for food packaging applications. *Carbohydr. Polym.* **2017**, *169*, 101–107.
[31] Lu, P. J.; Huang, S. C.; Chen, Y. P.; Chiueh, L. C.; Shih, D. Y. C. Analysis of titanium dioxide and zinc oxide nanoparticles in cosmetics. *J. Food Drug Anal.* **2015**, *23*, 587–594.
[32] Vegard, L. LV. Results of crystal analysis.-III. *London, Edinburgh, Dublin Philos. Mag. J. Sci.* **1916**, *32*, 505–518.
[33] Greenwood, G. LXVI. The crystal structure of cuprite and rutile. *London, Edinburgh, Dublin Philos. Mag. J. Sci.* **1924**, *48*, 654–663.
[34] Cromer, D. T.; Herrington, K. The structures of anatase and rutile. *J. Am. Chem. Soc.* **1955**, *77*, 4708–4709.
[35] Liang, S. Z.; Wang, X. Y.; Cheng, Y. J.; Xia, Y. G.; Müller-Buschbaum, P. Anatase titanium dioxide as rechargeable ion battery electrode-a chronological review. *Energy Storage Mater.* **2022**, *45*, 201–264.
[36] Xu, Z. L.; Lim, K.; Park, K. Y.; Yoon, G.; Seong, W. M.; Kang, K. Engineering solid electrolyte interphase for pseudocapacitive anatase TiO_2 anodes in sodium-ion batteries. *Adv. Funct. Mater.* **2018**, *28*, 1802099.
[37] Huang, J. P.; Yuan, D. D.; Zhang, H. Z.; Cao, Y. L.; Li, G. R.; Yang, H. X.; Gao, X. P. Electrochemical sodium storage of TiO_2(B) nanotubes for sodium ion batteries. *RSC Adv.* **2013**, *3*, 12593–12597.
[38] Marchand, R.; Brohan, L.; Tournoux, M. TiO_2(B) a new form of titanium dioxide and the potassium octatitanate $K_2Ti_8O_{17}$. *Mater. Res. Bull.* **1980**, *15*, 1129–1133.
[39] Latroche, M.; Brohan, L.; Marchand, R.; Tournoux, M. New hollandite oxides: TiO_2(H) and $K_{0.06}TiO_2$. *J. Solid State Chem.* **1989**, *81*, 78–82.
[40] Akimoto, J.; Gotoh, Y.; Oosawa, Y.; Nonose, N.; Kumagai, T.; Aoki, K.; Takei, H. Topotactic oxidation of ramsdellite-type $Li_{0.5}TiO_2$, a new polymorph of titanium dioxide: TiO_2(R). *J. Solid State Chem.* **1994**, *113*, 27–36.
[41] Xiong, H.; Slater, M. D.; Balasubramanian, M.; Johnson, C. S.; Rajh, T. Amorphous TiO_2 nanotube anode for rechargeable sodium ion batteries. *J. Phys. Chem. Lett.* **2011**, *2*, 2560–2565.
[42] Wang, H. W.; Jia, G. C.; Guo, Y. Y.; Zhang, Y. Q.; Geng, H. B.; Xu, J.; Mai, W.; Yan, Q. Y.; Fan, H. J. Atomic layer deposition of amorphous TiO_2 on carbon nanotube networks and their superior Li and Na ion storage properties. *Adv. Mater. Interfaces* **2016**, *3*, 1600375.
[43] Momma, K.; Izumi, F. *VESTA 3* for three-dimensional visualization of crystal, volumetric and morphology data. *J. Appl. Cryst.* **2011**, *44*, 1272–1276.
[44] Zhang, H. Z.; Banfield, J. F. Structural characteristics and mechanical and thermodynamic properties of nanocrystalline TiO_2. *Chem. Rev.* **2014**, *114*, 9613–9644.
[45] Usui, H.; Yoshioka, S.; Wasada, K.; Shimizu, M.; Sakaguchi, H. Nb-doped rutile TiO_2: A potential anode material for Na-ion battery. *ACS Appl. Mater. Interfaces* **2015**, *7*, 6567–6573.
[46] Armstrong, A. R.; Armstrong, G.; Canales, J.; García, R.; Bruce, P. G. Lithium-ion intercalation into TiO_2–B nanowires. *Adv. Mater.* **2005**, *17*, 862–865.
[47] Brutti, S.; Gentili, V.; Menard, H.; Scrosati, B.; Bruce, P. G. TiO_2-(B) nanotubes as anodes for lithium batteries: Origin and mitigation of irreversible capacity. *Adv. Energy Mater.* **2012**, *2*, 322–327.
[48] Ni, J. F.; Li, X. Y.; Sun, M. L.; Yuan, Y. F.; Liu, T. C.; Li, L.; Lu, J. Durian-inspired design of bismuth-antimony alloy arrays for robust sodium storage. *ACS Nano* **2020**, *14*, 9117–9124.

[49] Wu, L. M.; Bresser, D.; Buchholz, D.; Giffin, G. A.; Castro, C. R.; Ochel, A.; Passerini, S. Unfolding the mechanism of sodium insertion in anatase TiO_2 nanoparticles. *Adv. Energy Mater.* **2015**, *5*, 1401142.

[50] Li, W. J.; Yu, C. Y.; Huang, S. Z.; Zhang, C.; Chen, B. B.; Wang, X. F.; Yang, H. Y.; Yan, D.; Bai, Y. Synergetic Sn incorporation-Zn substitution in copper-based sulfides enabling superior Na-ion storage. *Adv. Mater.* **2024**, *36*, 2305957.

[51] Le, Z. Y.; Liu, F.; Nie, P.; Li, X. R.; Liu, X. Y.; Bian, Z. F.; Chen, G.; Wu, H. B.; Lu, Y. F. Pseudocapacitive sodium storage in mesoporous single-crystal-like TiO_2-graphene nanocomposite enables high-performance sodium-ion capacitors. *ACS Nano* **2017**, *11*, 2952–2960.

[52] Hijazi, H.; Ye, Z. W.; Zhang, L. B.; Deshmukh, J.; Johnson, M. B.; Dahn, J. R.; Metzger, M. Impact of sodium metal plating on cycling performance of layered oxide/hard carbon sodium-ion pouch cells with different voltage cut-offs. *J. Electrochem. Soc.* **2023**, *170*, 070512.

[53] Whittingham, M. S. Electrical energy storage and intercalation chemistry. *Science* **1976**, *192*, 1126–1127.

[54] Kim, K. T.; Ali, G.; Chung, K. Y.; Yoon, C. S.; Yashiro, H.; Sun, Y. K.; Lu, J.; Amine, K.; Myung, S. T. Anatase titania nanorods as an intercalation anode material for rechargeable sodium batteries. *Nano Lett.* **2014**, *14*, 416–422.

[55] Lindström, H.; Södergren, S.; Solbrand, A.; Rensmo, H.; Hjelm, J.; Hagfeldt, A.; Lindquist, S. E. Li^+ ion insertion in TiO_2 (Anatase). 2. Voltammetry on nanoporous films. *J. Phys. Chem. B* **1997**, *101*, 7717–7722.

[56] Hwang, J. Y.; Myung, S. T.; Lee, J. H.; Abouimrane, A.; Belharouak, I.; Sun, Y. K. Ultrafast sodium storage in anatase TiO_2 nanoparticles embedded on carbon nanotubes. *Nano Energy* **2015**, *16*, 218–226.

[57] Longoni, G.; Pena Cabrera, R. L.; Polizzi, S.; D'Arienzo, M.; Mari, C. M.; Cui, Y.; Ruffo, R. Shape-controlled TiO_2 nanocrystals for Na-ion battery electrodes: The role of different exposed crystal facets on the electrochemical properties. *Nano Lett.* **2017**, *17*, 992–1000.

[58] Han, M. S.; Zou, Z. Y.; Liu, J.; Deng, C. F.; Chu, Y. Q.; Mu, Y. B.; Zheng, K. X.; Yu, F. H.; Wei, L.; Zeng, L. et al. Pressure-induced defects and reduced size endow TiO_2 with high capacity over 20 000 cycles and excellent fast-charging performance in sodium ion batteries. *Small* **2024**, *20*, 2312119.

[59] Li, K. K.; Zhang, J.; Lin, D. M.; Wang, D. W.; Li, B. H.; Lv, W.; Sun, S.; He, Y. B.; Kang, F. Y.; Yang, Q. H. et al. Evolution of the electrochemical interface in sodium ion batteries with ether electrolytes. *Nat. Commun.* **2019**, *10*, 725.

[60] Cha, H. A.; Jeong, H. M.; Kang, J. K. Nitrogen-doped open pore channeled graphene facilitating electrochemical performance of TiO_2 nanoparticles as an anode material for sodium ion batteries. *J. Mater. Chem. A* **2014**, *2*, 5182–5186.

[61] Barnes, P.; Zuo, Y. X.; Dixon, K.; Hou, D. W.; Lee, S.; Ma, Z. Y.; Connell, J. G.; Zhou, H.; Deng, C. J.; Smith, K. et al. Electrochemically induced amorphous-to-rock-salt phase transformation in niobium oxide electrode for Li-ion batteries. *Nat. Mater.* **2022**, *21*, 795–803.

[62] Yan, Z. R.; Tang, D. F.; Fan, S. C.; Zou, X.; Huang, X. J.; Jiang, Q. Y.; Li, J. X.; Yu, R. H.; Lin, Y. B.; Huang, Z. G. et al. Unifying electrochemically-driven multistep phase transformations of rutile TiO_2 to rocksalt nanograins for reversible Li^+ and Na^+ storage. *Adv. Mater.* **2025**, *37*, 2419999.

[63] Tang, D. F.; Yu, R. H.; Jiang, Y. L.; Li, J. T.; Yan, Z. R.; Fan, S. C.; Huang, X. J.; Lee, S.; Li, T. Y.; Xie, Q. S. et al. Electrochemically *in situ* formed rocksalt phase in titanium dioxide determines pseudocapacitive sodium-ion storage. *Nat. Commun.* **2025**, *16*, 2015.

[64] Ohzuku, T.; Takehara, Z.; Yoshizawa, S. Nonaqueous lithium/titanium dioxide cell. *Electrochim. Acta* **1979**, *24*, 219–222.

[65] Bonino, F.; Busani, L.; Lazzari, M.; Manstretta, M.; Rivolta, B.; Scrosati, B. Anatase as a cathode material in lithium-organic electrolyte rechargeable batteries. *J. Power Sources* **1981**, *6*, 261–270.

[66] Zachauchristiansen, B. Lithium insertion in different TiO_2 modifications. *Solid State Ion.* **1988**, *28–30*, 1176–1182.

[67] Poizot, P.; Laruelle, S.; Grugeon, S.; Dupont, L.; Tarascon, J. M. Nano-sized transition-metal oxides as negative-electrode materials for lithium-ion batteries. *Nature* **2000**, *407*, 496–499.

[68] Sudant, G.; Baudrin, E.; Larcher, D.; Tarascon, J. M. Electrochemical lithium reactivity with nanotextured anatase-type TiO_2. *J. Mater. Chem.* **2005**, *15*, 1263–1269.

[69] Hu, Y. S.; Kienle, L.; Guo, Y. G.; Maier, J. High lithium electroactivity of nanometer-sized rutile TiO_2. *Adv. Mater.* **2006**, *18*, 1421–1426.

[70] Murphy, D. W.; Di Salvo, F. J.; Carides, J. N.; Waszczak, J. V. Topochemical reactions of rutile related structures with lithium. *Mater. Res. Bull.* **1978**, *13*, 1395–1402.

[71] Furukawa, H.; Hibino, M.; Honma, I. Electrochemical properties of nanostructured amorphous, sol-gel-synthesized TiO_2/acetylene black composite electrodes. *J. Electrochem. Soc.* **2004**, *151*, A527–A531.

[72] Idota, Y.; Kubota, T.; Matsufuji, A.; Maekawa, Y.; Miyasaka, T. Tin-based amorphous oxide: A high-capacity lithium-ion-storage material. *Science* **1997**, *276*, 1395–1397.

[73] Aricò, A. S.; Bruce, P.; Scrosati, B.; Tarascon, J. M. ; van Schalkwijk, W. Nanostructured materials for advanced energy conversion and storage devices. *Nat. Mater.* **2005**, *4*, 366–377.

[74] Wagemaker, M.; Borghols, W. J. H.; Mulder, F. M. Large impact of particle size on insertion reactions. A case for anatase Li_xTiO_2. *J. Am. Chem. Soc.* **2007**, *129*, 4323–4327.

[75] Wagemaker, M.; Borghols, W. J. H. ; van Eck, E. R. H.; Kentgens, A. P. M.; Kearley, G. J.; Mulder, F. M. The influence of size on phase morphology and Li-ion mobility in nanosized lithiated anatase TiO_2. *Chem. -Eur. J.* **2007**, *13*, 2023–2028.

[76] Cabana, J.; Monconduit, L.; Larcher, D.; Palacín, M. R. Beyond intercalation-based Li-ion batteries: The state of the art and challenges of electrode materials reacting through conversion reactions. *Adv. Mater.* **2010**, *22*, E170–E192.

[77] Xiong, H.; Yildirim, H.; Shevchenko, E. V.; Prakapenka, V. B.; Koo, B.; Slater, M. D.; Balasubramanian, M.; Sankaranarayanan, S. K. R. S.; Greeley, J. P.; Tepavcevic, S. et al. Self-improving anode for lithium-ion batteries based on amorphous to cubic phase transition in TiO_2 nanotubes. *J. Phys. Chem. C* **2012**, *116*, 3181–3187.

[78] Ren, Y.; Liu, Z.; Pourpoint, F.; Armstrong, A. R.; Grey, C. P.; Bruce, P. G. Nanoparticulate TiO_2(B): An anode for lithium-ion batteries. *Angew. Chem., Int. Ed.* **2012**, *51*, 2164–2167.

[79] Gentili, V.; Brutti, S.; Hardwick, L. J.; Armstrong, A. R.; Panero, S.; Bruce, P. G. Lithium insertion into anatase nanotubes. *Chem. Mater.* **2012**, *24*, 4468–4476.

[80] Armstrong, A. R.; Armstrong, G.; Canales, J.; Bruce, P. G. TiO_2–B nanowires. *Angew. Chem., Int. Ed.* **2004**, *43*, 2286–2288.

[81] Shin, J. Y.; Samuelis, D.; Maier, J. Sustained lithium-storage performance of hierarchical, nanoporous anatase TiO_2 at high rates: Emphasis on interfacial storage phenomena. *Adv. Funct. Mater.* **2011**, *21*, 3464–3472.

[82] Zhukovskii, Y. F.; Balaya, P.; Kotomin, E. A.; Maier, J. Evidence for interfacial-storage anomaly in nanocomposites for lithium batteries from first-principles simulations. *Phys. Rev. Lett.* **2006**, *96*, 058302.

[83] Jamnik, J.; Maier, J. Nanocrystallinity effects in lithium battery materials Aspects of nano-ionics. Part IV. *Phys. Chem. Chem. Phys.* **2003**, *5*, 5215–5220.

[84] Van der Ven, A.; Bhattacharya, J.; Belak, A. A. Understanding Li diffusion in Li-intercalation compounds. *Acc. Chem. Res.* **2013**, *46*, 1216–1225.

[85] Verma, P.; Maire, P.; Novák, P. A review of the features and analyses of the solid electrolyte interphase in Li-ion batteries.

Electrochim. Acta **2010**, *55*, 6332–6341.
[86] Ren, Y.; Hardwick, L. J.; Bruce, P. G. Lithium intercalation into mesoporous anatase with an ordered 3D pore structure. *Angew. Chem., Int. Ed.* **2010**, *49*, 2570–2574.
[87] Belak, A. A.; Wang, Y. Z.; Van der Ven, A. Kinetics of anatase electrodes: The role of ordering, anisotropy, and shape memory effects. *Chem. Mater.* **2012**, *24*, 2894–2898.
[88] Lee, D. H.; Lee, B. H.; Sinha, A. K.; Park, J. H.; Kim, M. S.; Park, J.; Shin, H.; Lee, K. S.; Sung, Y. E.; Hyeon, T. Engineering titanium dioxide nanostructures for enhanced lithium-ion storage. *J. Am. Chem. Soc.* **2018**, *140*, 16676–16684.
[89] Deng, D.; Kim, M. G.; Lee, J. Y.; Cho, J. Green energy storage materials: Nanostructured TiO_2 and Sn-based anodes for lithium-ion batteries. *Energy Environ. Sci.* **2009**, *2*, 818–837.
[90] Dambournet, D.; Belharouak, I.; Amine, K. Tailored preparation methods of TiO_2 anatase, rutile, brookite: Mechanism of formation and electrochemical properties. *Chem. Mater.* **2010**, *22*, 1173–1179.
[91] Liu, Y. Y.; Merinov, B. V.; Goddard, W. A. Origin of low sodium capacity in graphite and generally weak substrate binding of Na and Mg among alkali and alkaline earth metals. *Proc. Natl. Acad. Sci. USA* **2016**, *113*, 3735–3739.
[92] Farges, F.; Brown, G. E.; Rehr, J. J. Ti *K*-edge XANES studies of Ti coordination and disorder in oxide compounds: Comparison between theory and experiment. *Phys. Rev. B* **1997**, *56*, 1809–1819.
[93] Xu, Y.; Lotfabad, E. M.; Wang, H. L.; Farbod, B.; Xu, Z. W.; Kohandehghan, A.; Mitlin, D. Nanocrystalline anatase TiO_2: A new anode material for rechargeable sodium ion batteries. *Chem. Commun.* **2013**, *49*, 8973–8975.
[94] Chen, C. J.; Wen, Y. W.; Hu, X. L.; Ji, X. L.; Yan, M. Y.; Mai, L.; Hu, P.; Shan, B.; Huang, Y. H. Na^+ intercalation pseudocapacitance in graphene-coupled titanium oxide enabling ultra-fast sodium storage and long-term cycling. *Nat. Commun.* **2015**, *6*, 6929.
[95] Gan, Q. M.; He, H. N.; Zhu, Y. H.; Wang, Z. Y.; Qin, N.; Gu, S.; Li, Z. Q.; Luo, W.; Lu, Z. G. Defect-assisted selective surface phosphorus doping to enhance rate capability of titanium dioxide for sodium ion batteries. *ACS Nano* **2019**, *13*, 9247–9258.
[96] Hofmann, A.; Wang, Z. Q.; Bautista, S. P.; Weil, M.; Müller, F.; Löwe, R.; Schneider, L.; Mohsin, I. U.; Hanemann, T. Comprehensive characterization of propylene carbonate based liquid electrolyte mixtures for sodium-ion cells. *Electrochim. Acta* **2022**, *403*, 139670.
[97] Pan, K. H.; Lu, H. Y.; Zhong, F. P.; Ai, X. P.; Yang, H. X.; Cao, Y. L. Understanding the electrochemical compatibility and reaction mechanism on Na metal and hard carbon anodes of PC-based electrolytes for sodium-ion batteries. *ACS Appl. Mater. Interfaces* **2018**, *10*, 39651–39660.
[98] Li, F. J.; Wang, C.; Zhao, X. S. Sodium-ion storage properties of thermally stable anatase. *Energy Mater. Adv.* **2022**, *2022*, 9876319.
[99] Kavan, L.; Rathouský, J.; Grätzel, M.; Shklover, V.; Zukal, A. Surfactant-templated TiO_2 (anatase): Characteristic features of lithium insertion electrochemistry in organized nanostructures. *J. Phys. Chem. B* **2000**, *104*, 12012–12020.
[100] Bella, F.; Muñoz-García, A. B.; Meligrana, G.; Lamberti, A.; Destro, M.; Pavone, M.; Gerbaldi, C. Unveiling the controversial mechanism of reversible Na storage in TiO_2 nanotube arrays: Amorphous versus anatase TiO_2. *Nano Res.* **2017**, *10*, 2891–2903.
[101] Li, Q.; Li, H. S.; Xia, Q. T.; Hu, Z. Q.; Zhu, Y.; Yan, S. S.; Ge, C.; Zhang, Q. H.; Wang, X. X.; Shang, X. T. et al. Extra storage capacity in transition metal oxide lithium-ion batteries revealed by *in situ* magnetometry. *Nat. Mater.* **2021**, *20*, 76–83.
[102] Dylla, A. G.; Henkelman, G.; Stevenson, K. J. Lithium insertion in nanostructured TiO_2(B) architectures. *Acc. Chem. Res.* **2013**, *46*, 1104–1112.
[103] Xiao, B. W.; Liu, H. S.; Liu, J.; Sun, Q.; Wang, B. Q.; Kaliyappan, K.; Zhao, Y.; Banis, M. N.; Liu, Y. L.; Li, R. Y. et al. Nanoscale manipulation of spinel lithium nickel manganese oxide surface by multisite Ti occupation as high-performance cathode. *Adv. Mater.* **2017**, *29*, 1703764.
[104] Xia, T.; Zhang, W.; Li, W. J.; Oyler, N. A.; Liu, G.; Chen, X. B. Hydrogenated surface disorder enhances lithium ion battery performance. *Nano Energy* **2013**, *2*, 826–835.
[105] Augustyn, V.; Simon, P.; Dunn, B. Pseudocapacitive oxide materials for high-rate electrochemical energy storage. *Energy Environ. Sci.* **2014**, *7*, 1597–1614.
[106] Wagemaker, M.; Kentgens, A. P. M.; Mulder, F. M. Equilibrium lithium transport between nanocrystalline phases in intercalated TiO_2 anatase. *Nature* **2002**, *418*, 397–399.
[107] Miller, J. R.; Simon, P. Electrochemical capacitors for energy management. *Science* **2008**, *321*, 651–652.
[108] Augustyn, V.; Come, J.; Lowe, M. A.; Kim, J. W.; Taberna, P. L.; Tolbert, S. H.; Abruña, H. D.; Simon, P.; Dunn, B. High-rate electrochemical energy storage through Li^+ intercalation pseudocapacitance. *Nat. Mater.* **2013**, *12*, 518–522.
[109] Simon, P.; Gogotsi, Y. Materials for electrochemical capacitors. *Nat. Mater.* **2008**, *7*, 845–854.
[110] Zotti, G.; Schiavon, G.; Zecchin, S. Anodic dissolution of titanium in acetonitrile to Ti(IV) perchlorate and subsequent reductive electrodeposition of amorphous TiO_2 films. *J. Electrochem. Soc.* **1999**, *146*, 637–641.
[111] Simon, P.; Gogotsi, Y.; Dunn, B. Where do batteries end and supercapacitors begin. *Science* **2014**, *343*, 1210–1211.
[112] Yu, P. F.; Li, C. L.; Guo, X. X. Sodium storage and pseudocapacitive charge in textured $Li_4Ti_5O_{12}$ thin films. *J. Phys. Chem. C* **2014**, *118*, 10616–10624.
[113] Brezesinski, K.; Wang, J.; Haetge, J.; Reitz, C.; Steinmueller, S. O.; Tolbert, S. H.; Smarsly, B. M.; Dunn, B.; Brezesinski, T. Pseudocapacitive contributions to charge storage in highly ordered mesoporous group V transition metal oxides with iso-oriented layered nanocrystalline domains. *J. Am. Chem. Soc.* **2010**, *132*, 6982–6990.
[114] Denis, S.; Baudrin, E.; Touboul, M.; Tarascon, J. M. Synthesis and electrochemical properties of amorphous vanadates of general formula RVO_4 (R = In, Cr, Fe, Al, Y) vs. Li. *J. Electrochem. Soc.* **1997**, *144*, 4099–4199.
[115] Poizot, P.; Laruelle, S.; Grugeon, S.; Dupont, L.; Tarascon, J. M. From the vanadates to 3D-metal oxides negative electrodes. *Ionics* **2000**, *6*, 321–330.
[116] Denis, S.; Baudrin, E.; Orsini, F.; Ouvrard, G.; Touboul, M.; Tarascon, J. M. Synthesis and electrochemical properties of numerous classes of vanadates. *J. Power Sources* **1999**, *81–82*, 79–84.
[117] Laruelle, S.; Grugeon, S.; Poizot, P.; Dollé, M.; Dupont, L.; Tarascon, J. M. On the origin of the extra electrochemical capacity displayed by MO/Li cells at low potential. *J. Electrochem. Soc.* **2002**, *149*, A627–A634.
[118] Jung, H.; Taillefert, M.; Sun, J. Y.; Wang, Q.; Borkiewicz, O. J.; Liu, P.; Yang, L. F.; Chen, S.; Chen, H. L.; Tang, Y. Z. Redox cycling driven transformation of layered manganese oxides to tunnel structures. *J. Am. Chem. Soc.* **2020**, *142*, 2506–2513.
[119] Liu, H. D.; Zhu, Z. Y.; Yan, Q. Z.; Yu, S. C.; He, X.; Chen, Y.; Zhang, R.; Ma, L.; Liu, T. C.; Li, M. et al. A disordered rock salt anode for fast-charging lithium-ion batteries. *Nature* **2020**, *585*, 63–67.
[120] Yoshio ldota; Masayuki Mishima; Yukio Miyaki; Tadahiko Kubota; Tsutomu Miyasaka. U.S. Patent-5618640-A. 5618640.
[121] Courtney, I. A.; Dahn, J. R. Electrochemical and *in situ* X-ray diffraction studies of the reaction of lithium with tin oxide composites. *J. Electrochem. Soc.* **1997**, *144*, 2045–2052.
[122] Goward, G. R.; Leroux, F.; Power, W. P.; Ouvrard, G.; Dmowski, W.; Egami, T.; Nazaraa, L. F. On the nature of Li insertion in tin composite oxide glasses. *Electrochem. Solid-State Lett.* **1999**, *2*, 367–370.
[123] Sandu, I.; Brousse, T.; Santos-Peña, J.; Danot, M.; Schleich, D. M. comparison of the electrochemical behaviour of SnO_2 and PbO_2 negative electrodes for lithium ion batteries. *Ionics* **2002**, *8*, 27–35.

[124] Grugeon, S.; Laruelle, S.; Dupont, L.; Tarascon, J. M. An update on the reactivity of nanoparticles Co-based compounds towards Li. *Solid State Sci.* **2003**, *5*, 895–904.
[125] Poizot, P.; Laruelle, S.; Grugeon, S.; Tarascon, J. M. Rationalization of the low-potential reactivity of 3D-metal-based inorganic compounds toward Li. *J. Electrochem. Soc.* **2002**, *149*, A1212–A1217.
[126] Ling, L. M.; Bai, Y.; Li, Y.; Ni, Q.; Wang, Z. H.; Wu, F.; Wu, C. Quick activation of nanoporous anatase TiO_2 as high-rate and durable anode materials for sodium-ion batteries. *ACS Appl. Mater. Interfaces* **2017**, *9*, 39432–39440.
[127] Yan, D.; Pan, L. K. A new sodium storage mechanism of TiO_2 for sodium ion batteries. *Inorg. Chem. Front.* **2016**, *3*, 464–468.
[128] Buffat, P.; Borel, J. P. Size effect on the melting temperature of gold particles. *Phys. Rev. A* **1976**, *13*, 2287–2298.
[129] Wang, Y.; Sakamoto, J.; Kostov, S.; Mansour, A. N. ; denBoer, M. L.; Greenbaum, S. G.; Huang, C. K.; Surampudi, S. Structural aspects of electrochemically lithiated SnO: Nuclear magnetic resonance and X-ray absorption studies. *J. Power Sources* **2000**, *89*, 232–236.
[130] Anani, A.; Crouch-Baker, S.; Huggins, R. A. Kinetic and thermodynamic parameters of several binary lithium alloy negative electrode materials at ambient temperature. *J. Electrochem. Soc.* **1987**, *134*, 3098–3102.
[131] Ulus, A.; Rosenberg, Y.; Burstein, L.; Peled, E. Tin alloy-graphite composite anode for lithium-ion batteries. *J. Electrochem. Soc.* **2002**, *149*, A635–A643.
[132] Martos, M.; Morales, J.; Sánchez, L. Lead-based systems as suitable anode materials for Li-ion batteries. *Electrochim. Acta* **2003**, *48*, 615–621.
[133] Klein, F.; Jache, B.; Bhide, A.; Adelhelm, P. Conversion reactions for sodium-ion batteries. *Phys. Chem. Chem. Phys.* **2013**, *15*, 15876–15887.
[134] Li, W.; Fukunishi, M.; Morgan, B. J.; Borkiewicz, O. J.; Chapman, K. W.; Pralong, V.; Maignan, A.; Lebedev, O. I.; Ma, J. W.; Groult, H. et al. A reversible phase transition for sodium insertion in anatase TiO_2. *Chem. Mater.* **2017**, *29*, 1836–1844.
[135] Wu, L. M.; Buchholz, D.; Bresser, D.; Gomes Chagas, L.; Passerini, S. Anatase TiO_2 nanoparticles for high power sodium-ion anodes. *J. Power Sources* **2014**, *251*, 379–385.
[136] Zhou, M.; Xu, Y.; Wang, C. L.; Li, Q. W.; Xiang, J. X.; Liang, L. Y.; Wu, M. H.; Zhao, H. P.; Lei, Y. Amorphous TiO_2 inverse opal anode for high-rate sodium ion batteries. *Nano Energy* **2017**, *31*, 514–524.
[137] Qiu, B.; Zhou, Y. H.; Liang, H. Y.; Zhang, M. H.; Gu, K. X.; Zeng, T.; Zhou, Z.; Wen, W.; Miao, P.; He, L. H. et al. Negative thermal expansion and oxygen-redox electrochemistry. *Nature* **2025**, *640*, 941–946.
[138] Larcher, D.; Masquelier, C.; Bonnin, D.; Chabre, Y.; Masson, V.; Leriche, J. B.; Tarascon, J. M. Effect of particle size on lithium intercalation into α-Fe_2O_3. *J. Electrochem. Soc.* **2003**, *150*, A133–A139.
[139] Kim, H. S.; Cook, J. B.; Lin, H.; Ko, J. S.; Tolbert, S. H.; Ozolins, V.; Dunn, B. Oxygen vacancies enhance pseudocapacitive charge storage properties of MoO_{3-x}. *Nat. Mater.* **2017**, *16*, 454–460.
[140] Lee, J.; Urban, A.; Li, X.; Su, D.; Hautier, G.; Ceder, G. Unlocking the potential of cation-disordered oxides for rechargeable lithium batteries. *Science* **2014**, *343*, 519–522.
[141] Quine, T. E.; Duncan, M. J.; Armstrong, A. R.; Robertson, A. D.; Bruce, P. G. Layered $LixMn_{1-y}Ni_yO_2$ intercalation electrodes. *J. Mater. Chem.* **2000**, *10*, 2838–2841.
[142] Reed, J.; Ceder, G.; Van Der Ven, A. Layered-to-spinel phase transition in Li_xMnO_2. *Electrochem. Solid-State Lett.* **2001**, *4*, A78–A81.
[143] Wang, J.; Polleux, J.; Lim, J.; Dunn, B. Pseudocapacitive contributions to electrochemical energy storage in TiO_2 (anatase) nanoparticles. *J. Phys. Chem. C* **2007**, *111*, 14925–14931.
[144] Chen, S. H.; Xiao, Y.; Wang, Y. H.; Hu, Z. F.; Zhao, H.; Xie, W. A facile approach to prepare black TiO_2 with oxygen vacancy for enhancing photocatalytic activity. *Nanomaterials* **2018**, *8*, 245.
[145] Liu, G. H.; Li, J. D.; Fu, J.; Jiang, G. P.; Lui, G.; Luo, D.; Deng, Y. P.; Zhang, J.; Cano, Z. P.; Yu, A. P. et al. An oxygen-vacancy-rich semiconductor-supported bifunctional catalyst for efficient and stable zinc-air batteries. *Adv. Mater.* **2019**, *31*, 1806761.
[146] Liu, H. Y.; Zeng, F.; Lin, Y. S.; Wang, G. Y.; Pan, F. Correlation of oxygen vacancy variations to band gap changes in epitaxial ZnO thin films. *Appl. Phys. Lett.* **2013**, *102*, 181908.
[147] Idriss, H. On the wrong assignment of the XPS O1s signal at 531-532 eV attributed to oxygen vacancies in photo-and electro-catalysts for water splitting and other materials applications. *Surf. Sci.* **2021**, *712*, 121894.
[148] Xu, L. S.; Wu, Z. F.; Zhang, W. H.; Jin, Y. K.; Yuan, Q.; Ma, Y. S.; Huang, W. X. Oxygen vacancy-induced novel low-temperature water splitting reactions on FeO(111) monolayer-thick film. *J. Phys. Chem. C* **2012**, *116*, 22921–22929.
[149] Zhu, K. Y.; Shi, F.; Zhu, X. F.; Yang, W. S. The roles of oxygen vacancies in electrocatalytic oxygen evolution reaction. *Nano Energy* **2020**, *73*, 104761.
[150] Ou, G.; Xu, Y. S.; Wen, B.; Lin, R.; Ge, B. H.; Tang, Y.; Liang, Y. W.; Yang, C.; Huang, K.; Zu, D. et al. Tuning defects in oxides at room temperature by lithium reduction. *Nat. Commun.* **2018**, *9*, 1302.
[151] Sun, Z. Q.; Kim, J. H.; Zhao, Y.; Bijarbooneh, F.; Malgras, V.; Lee, Y.; Kang, Y. M.; Dou, S. X. Rational design of 3D dendritic TiO_2 nanostructures with favorable architectures. *J. Am. Chem. Soc.* **2011**, *133*, 19314–19317.
[152] Gao, X.; Li, Y. Q.; Zeng, W.; Zhang, C. F.; Wei, Y. M. Hydrothermal synthesis of agglomerating TiO_2 nanoflowers and its gas sensing. *J. Mater. Sci.: Mater. Electron.* **2017**, *28*, 18781–18786.
[153] Delacourt, C.; Poizot, P.; Levasseur, S.; Masquelier, C. Size effects on carbon-free $LiFePO_4$ powders: The key to superior energy density. *Electrochem. Solid-State Lett.* **2006**, *9*, A352–A355.
[154] Bruce, P. G.; Scrosati, B.; Tarascon, J. M. Nanomaterials for rechargeable lithium batteries. *Angew. Chem., Int. Ed.* **2008**, *47*, 2930–2946.
[155] Guo, Y. G.; Hu, J. S.; Wan, L. J. Nanostructured materials for electrochemical energy conversion and storage devices. *Adv. Mater.* **2008**, *20*, 2878–2887.
[156] Jung, S. K.; Hwang, I.; Chang, D.; Park, K. Y.; Kim, S. J.; Seong, W. M.; Eum, D.; Park, J.; Kim, B.; Kim, J. et al. Nanoscale phenomena in lithium-ion batteries. *Chem. Rev.* **2020**, *120*, 6684–6737.
[157] Chen, J. S.; Tan, Y. L.; Li, C. M.; Cheah, Y. L.; Luan, D. Y.; Madhavi, S.; Boey, F. Y. C.; Archer, L. A.; Lou, X. W. Constructing hierarchical spheres from large ultrathin anatase TiO_2 nanosheets with nearly 100% exposed (001) facets for fast reversible lithium storage. *J. Am. Chem. Soc.* **2010**, *132*, 6124–6130.
[158] Gan, Z. H.; Yin, J. Y.; Xu, X.; Cheng, Y. H.; Yu, T. Nanostructure and advanced energy storage: Elaborate material designs lead to high-rate pseudocapacitive ion storage. *ACS Nano* **2022**, *16*, 5131–5152.
[159] Cai, Q. L.; Li, X. L.; Hu, E. T.; Wang, Z. Y.; Lv, P.; Zheng, J. J.; Yu, K. H.; Wei, W.; Ostrikov, K. Overcoming ion transport barrier by plasma heterointerface engineering: Epitaxial titanium carbonitride on nitrogen-doped TiO_2 for high-performance sodium-ion batteries. *Small* **2022**, *18*, 2200694.
[160] Grugeon, S.; Laruelle, S.; Herrera-Urbina, R.; Dupont, L.; Poizot, P.; Tarascon, J. M. Particle size effects on the electrochemical performance of copper oxides toward lithium. *J. Electrochem. Soc.* **2001**, *148*, A285–A292.
[161] Wagemaker, M. ; van de Krol, R.; Kentgens, A. P. M.; van Well, A. A.; Mulder, F. M. Two phase morphology limits lithium diffusion in TiO_2 (anatase): A ^{7}Li MAS NMR study. *J. Am. Chem. Soc.* **2001**,

123, 11454–11461.
[162] Leesmith, M. J. A.; Halcovitch, N. R.; Hua, X. Electrochemical lithiation-induced formation of disordered rocksalt. *J. Mater. Chem. A* **2023**, *11*, 17027–17034.
[163] Chen, D. C.; Ahn, J.; Chen, G. Y. An overview of cation-disordered lithium-excess rocksalt cathodes. *ACS Energy Lett.* **2021**, *6*, 1358–1376.
[164] Zhang, H. Z.; Banfield, J. F. Thermodynamic analysis of phase stability of nanocrystalline titania. *J. Mater. Chem.* **1998**, *8*, 2073–2076.
[165] Kavan, L.; Attia, A.; Lenzmann, F.; Elder, S. H.; Grätzel, M. Lithium insertion into zirconia-stabilized mesoscopic TiO_2 (anatase). *J. Electrochem. Soc.* **2000**, *147*, 2897.
[166] Ranade, M. R.; Navrotsky, A.; Zhang, H. Z.; Banfield, J. F.; Elder, S. H.; Zaban, A.; Borse, P. H.; Kulkarni, S. K.; Doran, G. S.; Whitfield, H. J. Energetics of nanocrystalline TiO_2. *Proc. Natl. Acad. Sci. USA* **2002**, *99*, 6476–6481.
[167] Kavan, L.; Grätzel, M.; Gilbert, S. E.; Klemenz, C.; Scheel, H. J. Electrochemical and photoelectrochemical investigation of single-crystal anatase. *J. Am. Chem. Soc.* **1996**, *118*, 6716–6723.
[168] Maier, J. Defect chemistry and ion transport in nanostructured materials: Part II. Aspects of nanoionics. *Solid State Ion.* **2003**, *157*, 327–334.
[169] Frenkel, J. Über die Wärmebewegung in festen und flüssigen Körpern. *Z. Phys.* **1926**, *35*, 652–669.
[170] Wang, Y.; Richards, W. D.; Ong, S. P.; Miara, L. J.; Kim, J. C.; Mo, Y. F.; Ceder, G. Design principles for solid-state lithium superionic conductors. *Nat. Mater.* **2015**, *14*, 1026–1031.
[171] Funke, K. Solid state Ionics: From Michael faraday to green energy-the European dimension. *Sci. Technol. Adv. Mater.* **2013**, *14*, 043502.
[172] He, X. F.; Zhu, Y. Z.; Mo, Y. F. Origin of fast ion diffusion in super-ionic conductors. *Nat. Commun.* **2017**, *8*, 15893.
[173] Shin, J. Y.; Joo, J. H.; Samuelis, D.; Maier, J. Oxygen-deficient $TiO_{2-\delta}$ nanoparticles via hydrogen reduction for high rate capability lithium batteries. *Chem. Mater.* **2012**, *24*, 543–551.
[174] Shin, J. Y.; Samuelis, D.; Maier, J. Defect chemistry of lithium storage in TiO_2 as a function of oxygen stoichiometry. *Solid State Ion.* **2012**, *225*, 590–593.
[175] Lee, K.; Mazare, A.; Schmuki, P. One-dimensional titanium dioxide nanomaterials: Nanotubes. *Chem. Rev.* **2014**, *114*, 9385–9454.
[176] Sinhamahapatra, A.; Jeon, J. P.; Yu, J. S. A new approach to prepare highly active and stable black titania for visible light-assisted hydrogen production. *Energy Environ. Sci.* **2015**, *8*, 3539–3544.
[177] Wang, Z.; Yang, C. Y.; Lin, T. Q.; Yin, H.; Chen, P.; Wan, D. Y.; Xu, F. F.; Huang, F. Q.; Lin, J. H.; Xie, X. M. et al. Visible-light photocatalytic, solar thermal and photoelectrochemical properties of aluminium-reduced black titania. *Energy Environ. Sci.* **2013**, *6*, 3007–3014.
[178] Nakajima, T.; Nakamura, T.; Shinoda, K.; Tsuchiya, T. Rapid formation of black titania photoanodes: Pulsed laser-induced oxygen release and enhanced solar water splitting efficiency. *J. Mater. Chem. A* **2014**, *2*, 6762–6771.
[179] Li, W.; Corradini, D.; Body, M.; Legein, C.; Salanne, M.; Ma, J. W.; Chapman, K. W.; Chupas, P. J.; Rollet, A. L.; Julien, C. et al. High substitution rate in TiO_2 anatase nanoparticles with cationic vacancies for fast lithium storage. *Chem. Mater.* **2015**, *27*, 5014–5019.
[180] Koketsu, T.; Ma, J. W.; Morgan, B. J.; Body, M.; Legein, C.; Dachraoui, W.; Giannini, M.; Demortière, A.; Salanne, M.; Dardoize, F. et al. Reversible magnesium and aluminium ions insertion in cation-deficient anatase TiO_2. *Nat. Mater.* **2017**, *16*, 1142–1148.
[181] Zhou, M.; Xu, Y.; Xiang, J. X.; Wang, C. L.; Liang, L. Y.; Wen, L. Y.; Fang, Y. G.; Mi, Y.; Lei, Y. Understanding the orderliness of atomic arrangement toward enhanced sodium storage. *Adv. Energy Mater.* **2016**, *6*, 1600448.
[182] Shore, K. A. Electronic processes in non-crystalline materials (second edition), by N.F. Mott and E.A. Davis: Scope: Text book. Level: Advanced undergraduate. *Contemp. Phys.* **2014**, *55*, 337–337.
[183] Hashem, A. M.; Askar, M. H.; Winter, M.; Albering, J. H.; Besenhard, J. O. Two-phase reaction mechanism during chemical lithium insertion into α-MoO_3. *Ionics* **2007**, *13*, 3–8.
[184] Qie, L.; Chen, W. M.; Wang, Z. H.; Shao, Q. G.; Li, X.; Yuan, L. X.; Hu, X. L.; Zhang, W. X.; Huang, Y. H. Nitrogen-doped porous carbon nanofiber webs as anodes for lithium ion batteries with a superhigh capacity and rate capability. *Adv. Mater.* **2012**, *24*, 2047–2050.
[185] Bi, Z. H.; Paranthaman, M. P.; Menchhofer, P. A.; Dehoff, R. R.; Bridges, C. A.; Chi, M. F.; Guo, B. K.; Sun, X. G.; Dai, S. Self-organized amorphous TiO_2 nanotube arrays on porous Ti foam for rechargeable lithium and sodium ion batteries. *J. Power Sources* **2013**, *222*, 461–466.
[186] Ni, J. F.; Fu, S. D.; Wu, C.; Maier, J.; Yu, Y.; Li, L. Self-supported nanotube arrays of sulfur-doped TiO_2 enabling ultrastable and robust sodium storage. *Adv. Mater.* **2016**, *28*, 2259–2265.
[187] Mao, M. L.; Yan, F. L.; Cui, C. Y.; Ma, J. M.; Zhang, M.; Wang, T. H.; Wang, C. S. Pipe-wire TiO_2–Sn@carbon nanofibers paper anodes for lithium and sodium ion batteries. *Nano Lett.* **2017**, *17*, 3830–3836.
[188] Zhu, Y. E.; Yang, L. P.; Sheng, J.; Chen, Y. N.; Gu, H. C.; Wei, J. P.; Zhou, Z. Fast sodium storage in TiO_2@CNT@C nanorods for high-performance Na-ion capacitors. *Adv. Energy Mater.* **2017**, *7*, 1701222.
[189] Liu, S.; Niu, K.; Chen, S. L.; Sun, X.; Liu, L. H.; Jiang, B.; Chu, L. H.; Lv, X. J.; Li, M. C. TiO_2 bunchy hierarchical structure with effective enhancement in sodium storage behaviors. *Carbon Energy* **2022**, *4*, 645–653.
[190] Kim, H.; Kim, M. G.; Cho, J. Unique structural changes of three-dimensionally ordered macroporous TiO_2 electrode materials during electrochemical cycling. *Adv. Energy Mater.* **2012**, *2*, 1425–1432.
[191] Balogun, M. S.; Zhu, Y. K.; Qiu, W. T.; Luo, Y.; Huang, Y. C.; Liang, C. L.; Lu, X. H.; Tong, Y. X. Chemically lithiated TiO_2 heterostructured nanosheet anode with excellent rate capability and long cycle life for high-performance lithium-ion batteries. *ACS Appl. Mater. Interfaces* **2015**, *7*, 25991–26003.
[192] Lan, K.; Liu, Y.; Zhang, W.; Liu, Y.; Elzatahry, A.; Wang, R. C.; Xia, Y. Y.; Al-Dhayan, D.; Zheng, N. F.; Zhao, D. Y. Uniform ordered two-dimensional mesoporous TiO_2 nanosheets from hydrothermal-induced solvent-confined monomicelle assembly. *J. Am. Chem. Soc.* **2018**, *140*, 4135–4143.
[193] Li, B. S.; Xi, B. J.; Feng, Z. Y.; Lin, Y.; Liu, J. C.; Feng, J. K.; Qian, Y. T.; Xiong, S. L. Hierarchical porous nanosheets constructed by graphene-coated, interconnected TiO_2 nanoparticles for ultrafast sodium storage. *Adv. Mater.* **2018**, *30*, 1705788.
[194] Sheng, Q. Q.; Li, Q.; Xiang, L. X.; Huang, T.; Mai, Y.; Han, L. Double diamond structured bicontinuous mesoporous titania templated by a block copolymer for anode material of lithium-ion battery. *Nano Res.* **2021**, *14*, 992–997.
[195] Mahshid, S.; Askari, M.; Ghamsari, M. S. Synthesis of TiO_2 nanoparticles by hydrolysis and peptization of titanium isopropoxide solution. *J. Mater. Process. Technol.* **2007**, *189*, 296–300.
[196] Liu, Q. H.; Cao, Q.; Bi, H.; Liang, C. Y.; Yuan, K. P.; She, W.; Yang, Y. J.; Che, R. C. CoNi@SiO_2@TiO_2 and CoNi@Air@TiO_2 microspheres with strong wideband microwave absorption. *Adv. Mater.* **2016**, *28*, 486–490.
[197] Xiong, Y.; Qian, J. F.; Cao, Y. L.; Ai, X. P.; Yang, H. X. Graphene-supported TiO_2 nanospheres as a high-capacity and long-cycle life anode for sodium ion batteries. *J. Mater. Chem. A* **2016**, *4*, 11351–11356.
[198] Zhang, Y.; Wang, C. W.; Hou, H. S.; Zou, G. Q.; Ji, X. B. Nitrogen

doped/carbon tuning yolk-like TiO_2 and its remarkable impact on sodium storage performances. *Adv. Energy Mater.* **2017**, *7*, 1600173.

[199] Xu, D. F.; Chen, C. J.; Xie, J.; Zhang, B.; Miao, L.; Cai, J.; Huang, Y. H.; Zhang, L. N. A hierarchical N/S-codoped carbon anode fabricated facilely from cellulose/polyaniline microspheres for high-performance sodium-ion batteries. *Adv. Energy Mater.* **2016**, *6*, 1501929.

[200] Kavan, L.; Fattakhova, D.; Krtil, P. Lithium insertion into mesoscopic and single-crystal TiO_2 (rutile) electrodes. *J. Electrochem. Soc.* **1999**, *146*, 1375–1379.

[201] Lazzeri, M.; Vittadini, A.; Selloni, A. Structure and energetics of stoichiometric TiO_2 anatase surfaces. *Phys. Rev. B* **2001**, *63*, 155409.

[202] Zukalová, M.; Kalbáč, M.; Kavan, L.; Exnar, I.; Graetzel, M. Pseudocapacitive lithium storage in TiO_2(B). *Chem. Mater.* **2005**, *17*, 1248–1255.

[203] Kavan, L.; Kalbáč, M.; Zukalová, M.; Exnar, I.; Lorenzen, V.; Nesper, R.; Graetzel, M. Lithium storage in nanostructured TiO_2 made by hydrothermal growth. *Chem. Mater.* **2004**, *16*, 477–485.

[204] Zhou, Y. K.; Cao, L.; Zhang, F. B.; He, B. L.; Li, H. L. Lithium insertion into TiO_2 nanotube prepared by the hydrothermal process. *J. Electrochem. Soc.* **2003**, *150*, A1246–A1249.

[205] Fang, H. T.; Liu, M.; Wang, D. W.; Sun, T.; Guan, D. S.; Li, F.; Zhou, J. G.; Sham, T. K.; Cheng, H. M. Comparison of the rate capability of nanostructured amorphous and anatase TiO_2 for lithium insertion using anodic TiO_2 nanotube arrays. *Nanotechnology* **2009**, *20*, 225701.

[206] Wang, D. A.; Liu, L. F.; Zhang, F. X.; Tao, K.; Pippel, E.; Domen, K. Spontaneous phase and morphology transformations of anodized titania nanotubes induced by water at room temperature. *Nano Lett.* **2011**, *11*, 3649–3655.

[207] Liu, N.; Albu, S. P.; Lee, K.; So, S.; Schmuki, P. Water annealing and other low temperature treatments of anodic TiO_2 nanotubes: A comparison of properties and efficiencies in dye sensitized solar cells and for water splitting. *Electrochim. Acta* **2012**, *82*, 98–102.

[208] Xie, M.; Sun, X.; Zhou, C. G.; Cavanagh, A. S.; Sun, H. T.; Hu, T.; Wang, G. K.; Lian, J.; George, S. M. Amorphous ultrathin TiO_2 atomic layer deposition films on carbon nanotubes as anodes for lithium ion batteries. *J. Electrochem. Soc.* **2015**, *162*, A974–A981.

[209] Gibot, P.; Casas-Cabanas, M.; Laffont, L.; Levasseur, S.; Carlach, P.; Hamelet, S.; Tarascon, J. M.; Masquelier, C. Room-temperature single-phase Li insertion/extraction in nanoscale Li_xFePO_4. *Nat. Mater.* **2008**, *7*, 741–747.

[210] Wang, C.; Zhou, Y.; Ge, M. Y.; Xu, X. B.; Zhang, Z. L.; Jiang, J. Z. Large-scale synthesis of SnO_2 nanosheets with high lithium storage capacity. *J. Am. Chem. Soc.* **2010**, *132*, 46–47.

[211] Xiang, G. L.; Li, T. Y.; Zhuang, J.; Wang, X. Large-scale synthesis of metastable TiO_2(B) nanosheets with atomic thickness and their photocatalytic properties. *Chem. Commun.* **2010**, *46*, 6801–6803.

[212] Liu, J. H.; Chen, J. S.; Wei, X. F.; Lou, X. W.; Liu, X. W. Sandwich-like, stacked ultrathin titanate nanosheets for ultrafast lithium storage. *Adv. Mater.* **2011**, *23*, 998–1002.

[213] Ban, C. M.; Xie, M.; Sun, X.; Travis, J. J.; Wang, G. K.; Sun, H. T.; Dillon, A. C.; Lian, J.; George, S. M. Atomic layer deposition of amorphous TiO_2 on graphene as an anode for Li-ion batteries. *Nanotechnology* **2013**, *24*, 424002.

[214] Hong, K. J.; Kim, S. O. Atomic layer deposition assisted sacrificial template synthesis of mesoporous TiO_2 electrode for high performance lithium ion battery anodes. *Energy Storage Mater.* **2016**, *2*, 27–34.

[215] Ren, G. F.; Hoque, M. N. F.; Liu, J. W.; Warzywoda, J.; Fan, Z. Y. Perpendicular edge oriented graphene foam supporting orthogonal TiO_2(B) nanosheets as freestanding electrode for lithium ion battery. *Nano Energy* **2016**, *21*, 162–171.

[216] Maça, R. R.; Cíntora Juárez, D.; Castillo Rodríguez, M.; Etacheri, V. Nanointerface-driven pseudocapacitance tuning of TiO_2 nanosheet anodes for high-rate, ultralong-life and enhanced capacity sodium-ion batteries. *Chem. Eng. J.* **2020**, *391*, 123598.

[217] Luo, W. P.; Blanchard, J.; Xue, Y. P.; Taleb, A. The influence of TiO_2 nanoparticles morphologies on the performance of lithium-ion batteries. *Nanomaterials* **2023**, *13*, 2636.

[218] Tahir, M. N.; Oschmann, B.; Buchholz, D.; Dou, X. W.; Lieberwirth, I.; Panthöfer, M.; Tremel, W.; Zentel, R.; Passerini, S. Extraordinary performance of carbon-coated anatase TiO_2 as sodium-ion anode. *Adv. Energy Mater.* **2016**, *6*, 1501489.

[219] Guimarães, J. L.; Abbate, M.; Betim, S. B.; Alves, M. C. M. Preparation and characterization of TiO_2 and V_2O_5 nanoparticles produced by ball-milling. *J. Alloys Compd.* **2003**, *352*, 16–20.

[220] Kamei, M.; Mitsuhashi, T. Hydrophobic drawings on hydrophilic surfaces of single crystalline titanium dioxide: Surface wettability control by mechanochemical treatment. *Surf. Sci.* **2000**, *463*, L609–L612.

[221] Matsubara, M.; Yamaki, T.; Itoh, H.; Abe, H.; Asai, K. Preparation of TiO_2 nanoparticles by pulsed laser ablation: Ambient pressure dependence of crystallization. *Jpn. J. Appl. Phys.* **2003**, *42*, L479–L481.

[222] Hu, Y.; Tsai, H. L.; Huang, C. L. Effect of brookite phase on the anatase-rutile transition in titania nanoparticles. *J. Eur. Ceram. Soc.* **2003**, *23*, 691–696.

[223] Ulissi, U.; Zimmermann, J.; Brutti, S.; Hassoun, J. Investigation of the electrochemical features of carbon-coated TiO_2 anode for application in lithium-ion battery using high voltage $LiNi_{0.5}Mn_{1.5}O_4$ spinel cathode. *Electrochim. Acta* **2016**, *201*, 158–164.

[224] Zhang, Y.; Foster, C. W.; Banks, C. E.; Shao, L. D.; Hou, H. S.; Zou, G. Q.; Chen, J.; Huang, Z. D.; Ji, X. B. Graphene-rich wrapped petal-like rutile TiO_2 tuned by carbon dots for high-performance sodium storage. *Adv. Mater.* **2016**, *28*, 9391–9399.

[225] Su, D. W.; Dou, S. X.; Wang, G. X. Anatase TiO_2: Better anode material than amorphous and rutile phases of TiO_2 for Na-ion batteries. *Chem. Mater.* **2015**, *27*, 6022–6029.

[226] Guo, J.; Li, Y. Q.; Meng, J. H.; Pedersen, K.; Gurevich, L.; Stroe, D. I. Understanding the mechanism of capacity increase during early cycling of commercial NMC/graphite lithium-ion batteries. *J. Energy Chem.* **2022**, *74*, 34–44.

[227] Tian, R. Y.; Park, S. H.; King, P. J.; Cunningham, G.; Coelho, J.; Nicolosi, V.; Coleman, J. N. Quantifying the factors limiting rate performance in battery electrodes. *Nat. Commun.* **2019**, *10*, 1933.

[228] Yang, Y. F.; Biswas, S.; Xu, R.; Xiao, X.; Xu, X.; Zhang, P.; Gong, H. X.; Zheng, X. L.; Peng, Y. C.; Li, J. Y. et al. Capacity recovery by transient voltage pulse in silicon-anode batteries. *Science* **2024**, *386*, 322–327.

[229] Ponrouch, A.; Marchante, E.; Courty, M.; Tarascon, J. M.; Palacín, M. R. In search of an optimized electrolyte for Na-ion batteries. *Energy Environ. Sci.* **2012**, *5*, 8572–8583.

[230] Ponrouch, A.; Dedryvère, R.; Monti, D.; Demet, A. E.; Mba, J. M. A.; Croguennec, L.; Masquelier, C.; Johansson, P.; Palacín, M. R. Towards high energy density sodium ion batteries through electrolyte optimization. *Energy Environ. Sci.* **2013**, *6*, 2361–2369.

[231] Xu, K. Nonaqueous liquid electrolytes for lithium-based rechargeable batteries. *Chem. Rev.* **2004**, *104*, 4303–4418.

[232] Xu, K. Electrolytes and interphases in Li-ion batteries and beyond. *Chem. Rev.* **2014**, *114*, 11503–11618.

[233] Hibino, M.; Abe, K.; Mochizuki, M.; Miyayama, M. Amorphous titanium oxide electrode for high-rate discharge and charge. *J. Power Sources* **2004**, *126*, 139–143.

[234] Borghols, W. J. H.; Lützenkirchen-Hecht, D.; Haake, U.; Chan, W.; Lafont, U.; Kelder, E. M. ; van Eck, E. R. H.; Kentgens, A. P. M.; Mulder, F. M.; Wagemaker, M. Lithium storage in amorphous TiO_2 nanoparticles. *J. Electrochem. Soc.* **2010**, *157*, A582–A588.

[235] Chen, J.; Zhang, Y.; Zou, G. Q.; Huang, Z. D.; Li, S. M.; Liao, H. X.; Wang, J. F.; Hou, H. S.; Ji, X. S. Size-tunable olive-like anatase TiO_2 coated with carbon as superior anode for sodium-ion batteries.

Small **2016**, *12*, 5554–5563.
[236] Chen, J.; Ding, Z. Y.; Wang, C.; Hou, H. S.; Zhang, Y.; Wang, C. W.; Zou, G. Q.; Ji, X. B. Black anatase titania with ultrafast sodium-storage performances stimulated by oxygen vacancies. *ACS Appl. Mater. Interfaces* **2016**, *8*, 9142–9151.
[237] Han, J. H.; Hirata, A.; Du, J.; Ito, Y.; Fujita, T.; Kohara, S.; Ina, T.; Chen, M. W. Intercalation pseudocapacitance of amorphous titanium dioxide@nanoporous graphene for high-rate and large-capacity energy storage. *Nano Energy* **2018**, *49*, 354–362.
[238] Xu, W. H.; Jiang, L.; Li, Y. W.; Huang, Q. Z.; Yao, J. H.; Lei, C. H. Anatase TiO_2 micro/nano-spheres with rich oxygen vacancies as a high-performance anode material for sodium-ion batteries. *J. Energy Storage* **2024**, *91*, 112014.
[239] Pralong, V. Lithium intercalation into transition metal oxides: A route to generate new ordered rock salt type structure. *Prog. Solid State Chem.* **2009**, *37*, 262–277.
[240] Perez, A. J.; Jacquet, Q.; Batuk, D.; Iadecola, A.; Saubanère, M.; Rousse, G.; Larcher, D.; Vezin, H.; Doublet, M. L.; Tarascon, J. M. Approaching the limits of cationic and anionic electrochemical activity with the Li-rich layered rocksalt Li_3IrO_4. *Nat. Energy* **2017**, *2*, 954–962.
[241] Singer, A.; Zhang, M.; Hy, S.; Cela, D.; Fang, C.; Wynn, T. A.; Qiu, B.; Xia, Y.; Liu, Z.; Ulvestad, A. et al. Nucleation of dislocations and their dynamics in layered oxide cathode materials during battery charging. *Nat. Energy* **2018**, *3*, 641–647.

Zhiyu Zou is currently studying for a master's degree in the Department of mechanical Energy and Engineering, Southern University of Science and Technology, under the supervision of Prof. Tianshao Zhao. His research is mainly focused on designing advanced electrodes and their interfaces for sodium-ion batteries.

Yongbiao Mu recently completed his Ph.D. studies under the supervision of Professor Lin Zeng in the Department of Mechanical and Energy Engineering at the SUSTech. He received his M.S. degree in Materials Science and Engineering from Harbin Institute of Technology in 2019. He has published over 30 research articles as the first or corresponding author in high-impact journals such as *Nature Communications*, *Advanced Materials*, and *Energy & Environmental Science*. His publications have been cited more than 3,000 times, with an H-index of 29 (Google Scholar).

Meisheng Han is a research associate professor in the Department of Mechanical and Energy Engineering, Southern University of Science and Technology. His research interests focus on advanced Li/Na/K-ion-battery anodes, electrode design for redox flow batteries, and ultrafast synthesis of high-entropy materials. He has published over 80 SCI-indexed papers with an H-index of 24. He serves as a young editorial board member of *Nano Research Energy*, *eScience*, and *Nano-Micro Letters*.

Lin Zeng is a tenured Associate Professor in the Department of Mechanical and Energy Engineering at the SUSTech. His research focuses on fuel cells, water electrolysis, and electrochemical energy storage systems. He has published over 200 SCI-indexed papers with an H-index of 54. From 2021 to 2025, he was consecutively listed among the "World's Top 2% Scientists" by Stanford University and, was included in the "Career-Long Scientific Impact Ranking" from 2024-2025. He also serves as a Youth Editorial Board Member for journals such as *Advanced Powder Materials* and *Sustainable Chemistry for Energy Materials*.

Tianshou Zhao is a Chair Professor of Department of Mechanical and Energy Engineering, Director of the Energy Institute for Carbon Neutrality of the Southern University of Science and Technology. He combines his expertise in research and technological innovation with a commitment to creating clean energy production and storage devices for a sustainable future. His research mainly focuses on fuel cells, advanced batteries, multi-scale multiphase heat and mass transport with electrochemical reactions, and computational modeling.